A SIMPLIFIED PHASE DISPLAY SYSTEM FOR 3D SURFACE MEASUREMENT AND ABNORMAL SURFACE PATTERN DETECTION

by

Xin Weng

A dissertation submitted in partial fulfillment
of the requirements for the degree of
Doctor of Philosophy
(Mechanical Engineering)
in the University of Michigan
2017

Doctoral Committee:

Professor Jun Ni, Chair
Dr. Carl Aleksoff, Coherix, Inc.
Professor Jeffrey A. Fessler
Professor Albert J. Shih
Professor Herbert G. Winful

To my beloved wife Tianwei Yang, my parents and parents-in-law.

ACKNOWLEGEMENTS

I would like to express my most sincere gratitude to my advisor, Professor Jun Ni, for his continuous support, guidance and encouragement throughout my graduate study. Without him, I would never have had the chance to begin, continue, and complete my research. I also want to thank Prof. Ni and the Chinese Scholarship Council for providing me the funding to support my Ph.D study in the University of Michigan.

I am also grateful to all my dissertation committee members, for their constructive advice on this dissertation and patient guidance.

I want to give my special thanks to all the amazing people in Coherix, especially Mr. Dwight Carlson and Dr. Zhenhua Huang for supporting my work, Dr. Carl Aleksoff, Mr. Ron Swonger, Mr. Alex Klooster, and Dr. Bin Li for working with me on various projects. All of them have given me tremendous amount of valuable suggestions. It was my great pleasure to have the opportunity to work with them for the past several years on many exciting projects. I have learned so many valuable things that will definitely benefit me in future career.

I would like to thank my friends and co-workers in the Wu Manufacturing Research Center for their kind help and support. In addition, there are all the other friends I have made, the list is too long to mention all, but their friendships are thankful.

Finally, I want to dedicate this work to my family for the endless support that they have never ceased to give me. Without their support, I could not make this dissertation happen.

TABLE OF CONTENTS

LIST OF FIGURES

LIST OF TABLES

ABSTRACT

It is widely observed that today's engineering products demand increasingly strict tolerances. The shape of a machined surface plays a critical role to the desired functionality of a product. Even a small error can be the difference between a successful product launch and a major delay. It is important to develop tools that confirm the quality and accuracy of manufactured products. The key to assessing the quality is robust measurement and inspection tools combined with advanced analysis. This research is motivated by the goals of 1) developing an advanced optical metrology system that provides accurate 3D profiles of target objects with curvature and irregular texture and 2) developing algorithms that can recognize and extract meaningful surface features with the consideration of machining process information.

A new low cost measurement system with a simple coherent interferometric fringe projection system is proposed and developed. Comparing with existing optical measurement systems, the developed system generates fringe patterns on object surface through a pair of fiber optics that have a relatively simple and flexible configuration. Three-dimensional measurements of a variety of engineering surfaces with curvatures demonstrate the applicability and flexibility of the developed system. Also, an improved phase unwrapping algorithm based on a flood fill method is developed to improve the quality of image processing. The developed algorithm performs phase unwrapping under the guidance of a hybrid quality map that is generated by considering the quality of both the intensity images acquired from the measurement

system and the calculated wrapped phase map. This algorithm demonstrates good robustness to noises both in the original images and errors in the calculated wrapped phase map.

Advances in metrology systems enable engineers to obtain a large amount of surface information. Revealed surface details open the torrent of observable events at the plant floor and increase the transparency of manufacturing processes. However, engineers are also facing the challenge of how to avoid data redundancy and extract the most valuable information from big data sets. A systematic framework for surface shape characterization and abnormal pattern detection is proposed to take the advantage of the availability of high definition surface measurements through advanced metrology systems. The proposed framework evaluates a measured surface in two stages. The first step focuses on the extraction of general shape (e.g., surface form) from measurement for surface functionality evaluation and process monitoring. The second step focuses on the extraction of application specific surface details with the consideration of process information (e.g., surface waviness). Applications of automatic abnormal surface pattern detection have been demonstrated.

In summary, this research focuses on two core areas: 1) developing a metrology system that is capable of measuring engineered surfaces accurately; 2) proposing a methodology that can extract meaningful information from high definition measurements with consideration of process information and product functionality.

CHAPTER 1 INTRODUCTION

1.1 Problem statements and motivation

With the help of advanced technologies in computer science and innovative developments of digital imaging devices, electro-optical components, laser and other light sources, imaging systems for the acquisition of 3D shapes have attracted considerable interest for various applications [Chen, 2000, Blais, 2004, Sansoni 2009]. More and more developed instruments have now been commercially available for surface inspection and quality control. In manufacturing industries, increasing demands in functionality and production efficiency require faster inspections, preferably close to the production line. New emerging trends can be described as: 1) Replace traditional measurement systems that require operator intervention with measurement systems that can achieve automatic measurement and provide real-time enhanced information in 3D in user-defined reference frame; 2) Better performance in terms of measurement accuracy (micron-level, nano-level), speed (in seconds) and reliability is desired; and 3) Less skill is required for operators to perform measurements and obtained results are easy to interpret without the need of profound background knowledge.

1.1.1 Measurement of gear tooth flanks

Gear designers are confronted with increasing demands concerning lifetime, power transmission efficiency and noise emission, whereas the size and weight of gear drives are constantly reduced. The tooth flanks are important structural elements of gear. They are critical to reduce noise and improve running properties (e.g., fatigue life, vibration) as well as enhance load-carrying capability. Thus, the measurement of gears is of importance for gear production. The traditional method to measure gear tooth flank is based on contact probe scanning measurement such as a Coordinate Measuring Machine (CMM), shown in Figure 1.1. [Fette, 1985; Pommer, 2002]. Although CMMs can achieve high accuracy in measurement, they can only measure one line profile at a time. One can either use these measured profiles directly for quality inspection or interpolate lines to get estimations of the whole surface. This method is very time consuming.

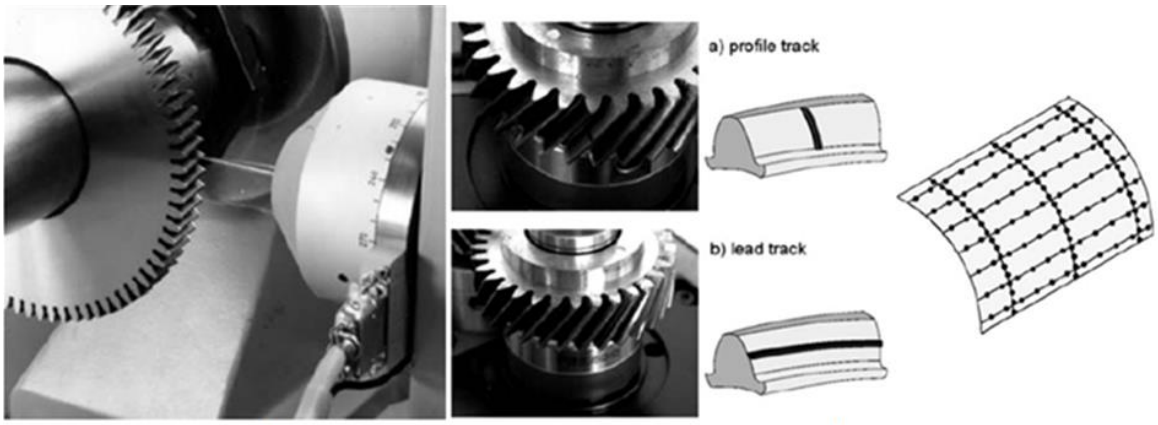

(1) Measurement of shaving gears using CMM

(2) Grid of measured points obtained by rollscan method

Figure 1.1 Gear measurements using contact methodologies [Fette, 1985; Pommer, 2002]

The only available high-speed inspection method is composite inspection, in which the gear to be investigated is run in mesh with a known master gear and the motions of the master

gear axes are measured. Figure 1.2 shows an example of this technique [Goch, 2003]. This technique is much faster than CMMs that use scanning techniques. However, composite inspection is still a mechanical and contacting technique. And the master gears are usually expensive and wear out regularly. Moreover, the measured results are difficult to be used directly for rectifications of manufacturing process even when errors are detected since it is difficult to derive analytical results from the measurement.

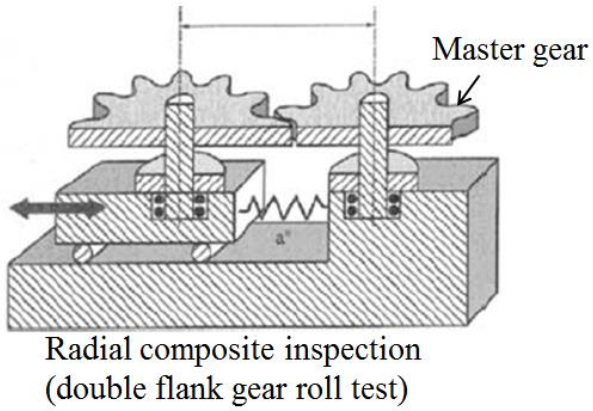

Figure 1.2 Radial composite inspection of a gear [Goch, 2003]

On the other hand, optical techniques have great potential for achieving non-contact, high-speed, high-precision gear measurement. Many measurement systems have been developed by various researchers. [Lu et al., 1998] developed a gear inspection system using a phase-shift triangulation measurement technique. It projected a pre-determined pattern onto the gear surface and collected the projected pattern at a previously verified triangulation angle. The 3D surface of an object was extracted from the distortion of the recorded pattern. [Peters et al., 2000] developed a system using structured light for measuring a helical gear. The projector used was built up using a Digital Micromirror Device (DMD), the principle of this measurement system was also based on triangulation. [Younes et al., 2005] developed a gear gauging system based on optical obscuration and used a laser as a light source for measuring tooth flank and other

parameters. [Fang et al., 2011] developed a laser interferometric system for the measurement of a gear tooth flank.

Interferometry is one of the optical techniques applied for precise surface profile measurement. However, it is highly sensitive to environmental factors such as air flow, temperature and vibration. Moiré techniques have been widely applied in the measurement of surface profiles in manufacturing industries. However, the gear's rough surface could result in poor Moiré fringe contrast and a low signal-to-noise ratio that reduces the accuracy of the measurement. Laser scanning triangulation is another technique that has been used in industry. Since it requires mechanical movement of either the object or the scanner itself, vibration noise is always involved and the results are also affected by laser speckle noise.

Currently available measurement systems normally are designed to measure a specific type of gear. And the optical configurations are complicated, so they require long setup work and require highly skilled operator. Hence the applications are limited. A flexible system that can perform high accuracy and high speed gear inspection is still desired.

1.1.2 Measurement of laser weld bead

Laser welding is a process that results in fusion of materials by directing a highly concentrated laser beam on a relatively small area. It is versatile and applicable for joining miniature electronic components or welding thick steel structures. This welding technique has many merits such as high speed, high productivity and low heat input. As the process of laser welding is better understood, the range of engineering applications has rapidly grown, especially in the automotive, aerospace and microelectronic industries. However, the quality of the weld bead produced by laser welding can be affected by many process parameters such as the laser power, feed rate and etc. Scrap rate would be high to manufacturers if wielded beads cannot meet

the quality standards. Therefore, it is important to have inspections on the weld bead to ensure high welding quality.

Available methods for weld bead inspection include radiographic inspection, magnetic inspection, acoustic emission inspection and optical inspection. Radiographic inspection is a non-destructive technique using radiographic sensors and can be applied to most weldments [Chen et al., 2005]. However, the radioactivity restricted the usage of this technique. Magnetic defect detection has high sensitivity and is easy to operate [Ewald, 2003]. But this technique is limited to ferromagnetic materials and it is difficult to be operated automatically. Acoustic emission inspection involves a sensor that converts process acoustic emissions into measurable signals. Sensors applied in this technique can be installed on the weldment (known as structure-borne emission monitoring) [Passini, 2011] or an independent transducer can receive sound (microphone, known as air borne emission monitoring) [Gu and Duley, 1996]. For the structure-borne inspection, contact installation is needed that restricts its application in in-line mass production. For air-borne emission inspection, it is difficult to acquire the desired sound signal in noisy environments even when a directional transducer is applied. Signals acquired from both techniques usually need skilled operators to interpret them, which also limits its application. Optical inspection is the most widely used technique in the inspection of the weld bead quality. Thanks to the advanced techniques from the field of computer vision, a large variety of vision sensors are available for measuring various parameters of the weld beads [White et al., 1994; Hugel et al., 1999; Park and Rhee 1999; Xu et al., 2004; Sikström et al., 2006; Li et al., 2010]. Among these sensors, vision sensors based on laser techniques have several comparative advantages that include: high efficiency, simple and low cost system configuration, and less human intervention.

For inspection on large beads (width >10mm), almost all the aforementioned techniques can provide reliable results. However, in the measurement of weld beads with narrow width (<2mm, Figure 1.3), most of them could not provide good measurement results as for large bead due to the principles by which they detect the bead.

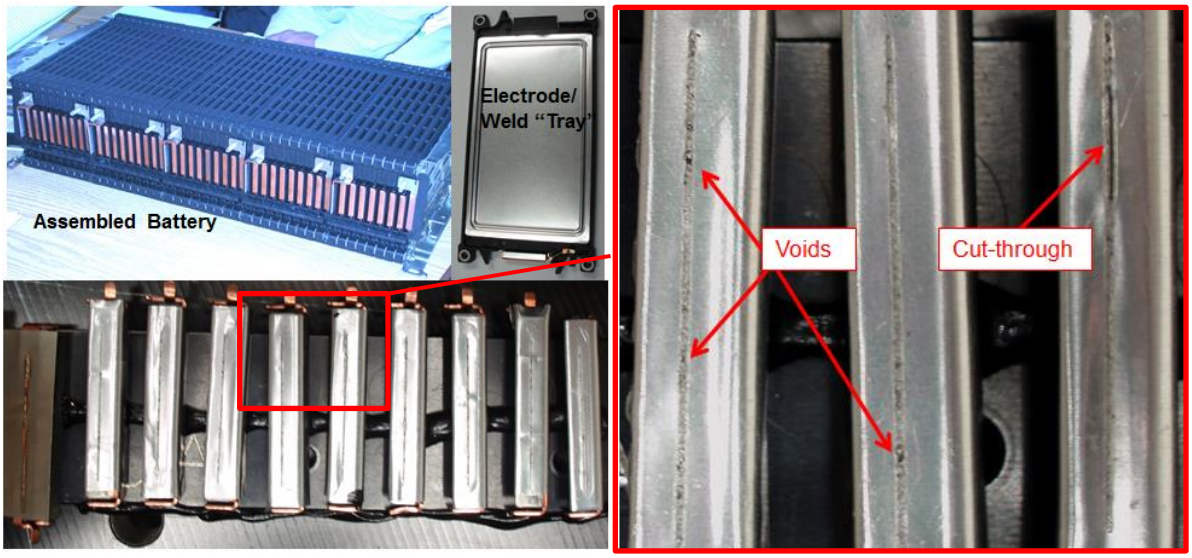

Figure 1.3 Illustration of laser weld defects in an assembled battery (bead width <= 2mm)

In traditional laser-based vision system for the inspection of weld beads, a camera with a pre-selected narrow band filter is applied to pick up the laser stripe (Figure 1.4). The feature points (such as points on boundaries of bead) of the laser stripe will be extracted based on the triangulation principle. Thus, the geometrical defects of a weld bead are measured. When measuring butted-together metal sheets of mono thickness or weld beads with low height jumps, it is difficult to extract feature points of laser stripes. Moreover, this method also suffers from laser speckle noise, which will make the feature point selection more difficult. A system that is capable of doing areal measurement at high accuracy and fast speed is desired for the inspection of laser welds with narrow width.

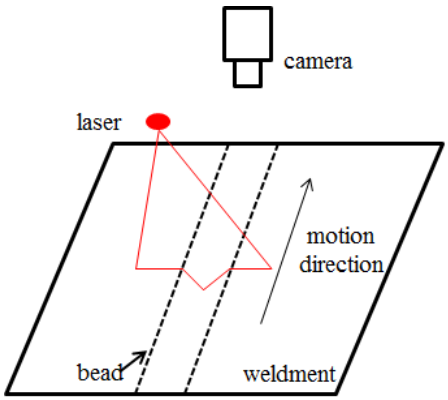

Figure 1.4 Typical frame definition of the vision sensor based on laser-triangulation principle

1.1.3 Multi-scale surface shape characterization

Advances in metrology system enables engineer to measure a machined surface at greater details fast and accurately. The measurement system developed based on digital holographic interferometry [Aleksoff, 2006] can provide sub-micron precision measurement in height direction over a Field Of View (FOV) of 300 x 300 mm^2. Surfaces measured through this technology can be characterized at greater details such that information from multiple scales can be extracted from the same measurement without changing platform or techniques. General shape of the surface, local regular pattern and anomalies can all be mined from one non-contact measurement. The availability of this technique also led to new findings on surface shape, especially in the flatness and waviness scales. Uncovered details indicate there is a lack of appropriate surface shape metrics that can fully capture and describe the variation of a surface shape.

For instance, considering the assembly process of engine head and engine block, the surfaces of engine head and block are usually assembled together under high hydraulic forces. Improper match of the surfaces may induce distortion in cam bore alignment that will affect head gasket sealing or cause cylinder bore distortion illustrated in Figure 1.5a. Thus, tight tolerances

are always imposed in machining the surfaces of engine head and block to reduce the impacts of non-flat surfaces being assembled together. However, it is also impossible for manufacturer to achieve zero flatness under current techniques in mass production. The shape of a surface plays an important role in assembly. Two measured engine heads shown in Figure 1.5b have similar flatness measurements (38 μm for engine head 1 and 35 μm for engine head 2) and all meet the required tolerance. However, these two engine heads cannot be treated as identical in the assembly process. If engine head 1 is assembled with the given engine block, the situation shown in Figure 1.5a occurs and may result in distortion in camshaft area. Alternatively, engine head 2 matches the engine block much better and can avoid the potential distortion in camshaft. This example demonstrates that surface flatness as a metric is not sufficient to describe the shape of a machined surface. New metrics are needed to characterize the surface shape for the evaluation of quality.

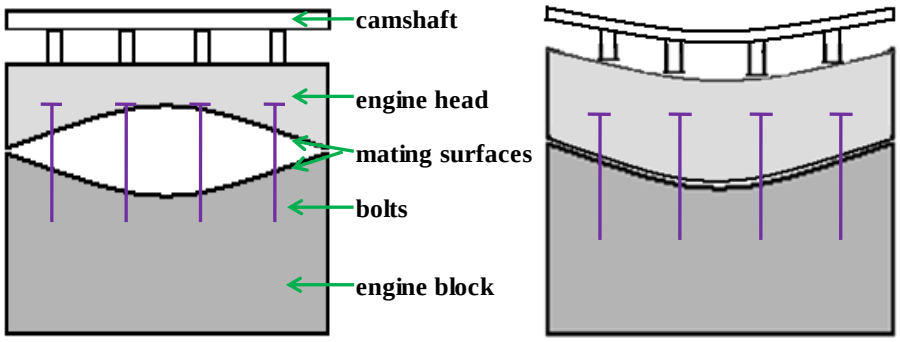

(a)

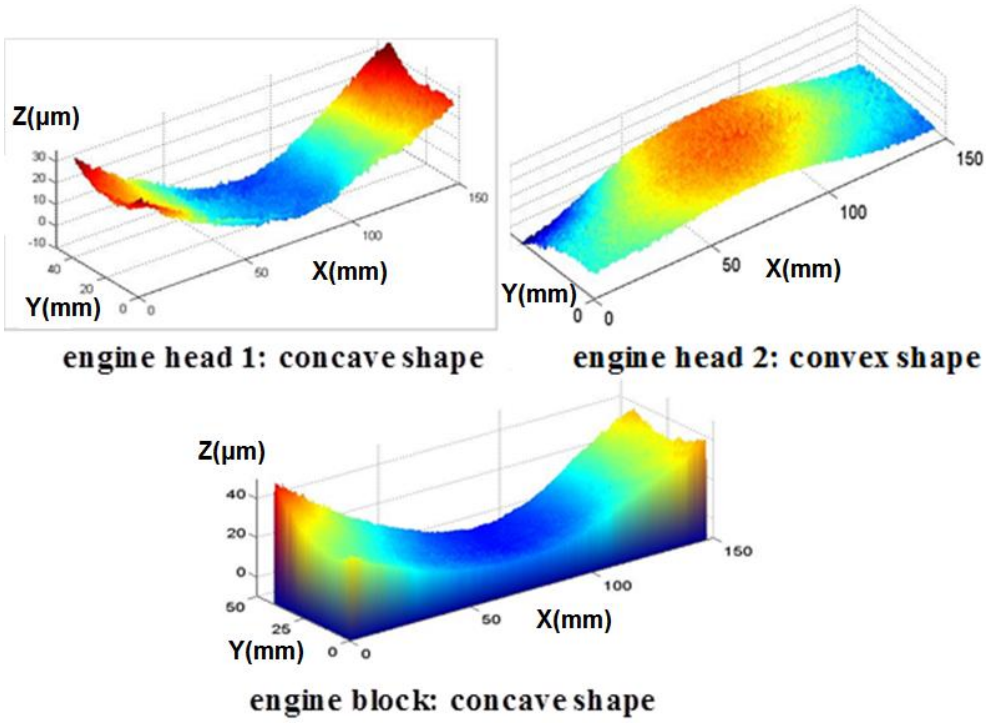

(b)

Figure 1.5 Impact of surface shape on assembly: (a) illustration of engine assembly, (b) surface measurements of engine head and block

Another observation shows that surface shape can clearly reflect the pattern of a changing process parameter over time. Figure 1.6 shows a V10 engine block combustion deck surface measured using a digital holographic interferometry system. Except the wear of inserts on the face mill degraded with time, no other process parameter was changed. Measurements were taken after the deck face milling process at constant time intervals. Figures 1.6b and 1.6c show measurements taken at the time of new cutting tools were installed and after 1800 milling cycles, respectively. The overall flatness values for both surfaces were within the tolerance. However, obvious local distortions can be observed at both ends and areas between cylinder bores in Figure 1.6c. This shows how the degradation of cutting tools could affect the shape of a machined surface. To prevent the local distortions that may cause potential leakage problem in assembled engines, manufacturers can change cutting tools by developing a surface metric that

tracks the local distortion. Compared to conventional techniques in tool change policy that usually just tracks the cycle number a tool has been used, the knowledge gained from this study reveals the direct impacts on the surface from degraded tools and enables manufacturers make tool change in time.

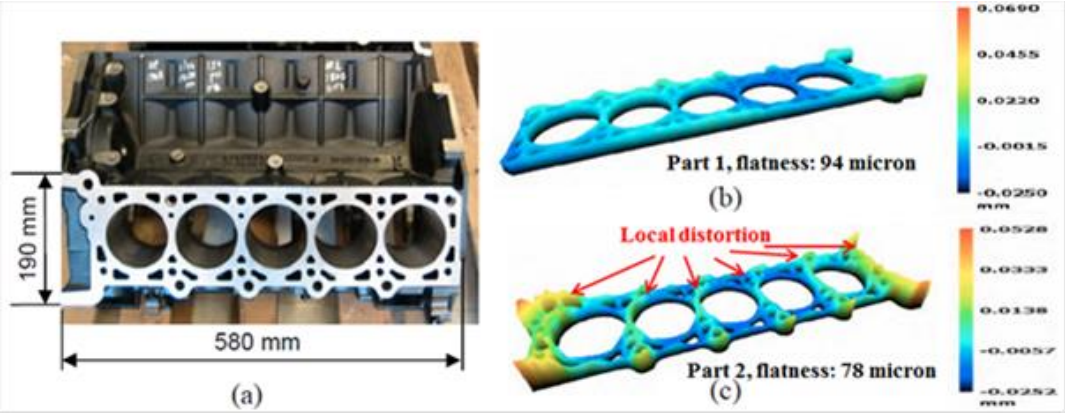

Figure 1.6 V10 engine block surface measurement: (a) overview, (b) new cutting tool and (c) after 1800 milling cycles

In summary, there is a lack of quantifiable surface shape metrics that can be applied to evaluate product quality and the machining process. This limitation is due to the instruments being used as well as the conventional GD&T definitions developed decades ago. Therefore, the characterization and analysis of machined surface patterns integrated with engineering process knowledge present great research opportunities and are of substantial importance to manufacturing.

1.2 Literature reviews of 3D optical measurement techniques

Various optical techniques have been developed for 3D shape measurements. Based on the principles of time-in-flight, stereovision, laser triangulation, photogrammetry, interferometry, and structured light. This section will give a brief review of several widely applied optical metrology techniques.

1.2.1. Time-in-flight

Systems using this technique conduct dimensional measurement based on the direct measurement of the time of flight of a laser or any other light source impulse [Moring and Ailisto, 1989]. Figure 1.7 shows a schematic diagram of a basic measurement system using time-in-flight technique. The major components of such a system include a computer for data processing, a controller for synchronization, a transmitter that generates light pulses (e.g., a laser diode), and a receiver for sensing the signals reflected from the object. The time difference between the object pulse, which is reflected back from target object, and the reference pulse will be calculated once the receiver obtained both signals. Typical resolution of this method is around 1 mm. This technique can provide excellent measurement results in large ranges (>1 m). To measure object small in size, if high speed timing circuitry is implemented, sub-millimeter resolution is achievable.

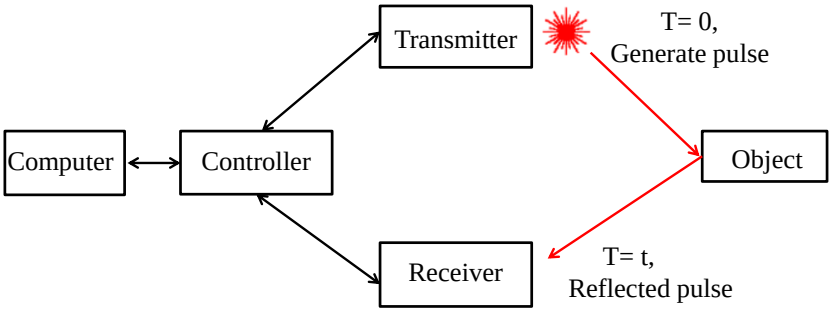

Figure 1.7 Schematic diagram of basic time-in-flight measurement system

1.2.2. Stereovision

Measurement system based on this technique has been studied extensively [Hutber, 1987; Aguilar et al., 1996; Sun et al., 2006]. This technique uses two cameras taking images of the same object simultaneously but from different observation positions (Figure 1.8). Corresponding

algorithm will compare the captured two images and find the homologous reference points. Then the best match parts will be used to calculate the distance.

However, it is challenging to precisely locate the homologous points on both images since errors are inevitable during measurements. Advanced methods have been developed to provide more accurate and efficient stereo matching such as segment-based stereo matching [Medioni and Nevatia, 1985], stereo matching with active window [Kanade and Okutomi, 1994], and stereo matching using belief propagation [Sun et al., 2003].

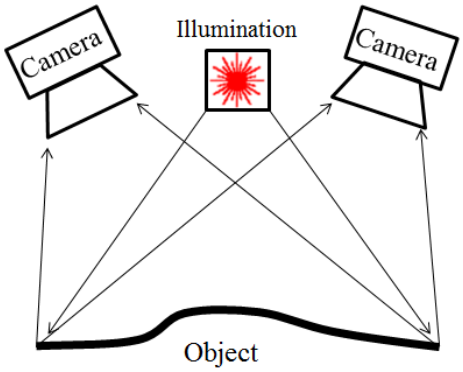

Figure 1.8 Schematic diagram of basic stereovision measurement system

1.2.3. Laser triangulation

Both single point laser triangulators and laser scanners apply the well-known triangulation relationship in optics [Ji and Leu, 1989; Keferstein and Marxer, 1998]. With respect to the time-in-flight technique, systems based on the laser triangulation technique project a laser pulse or laser line on the subject and use a digital camera or PSD (position sensitive detector) to look for the location of the reflected laser signals. Signals reflected from different positions on the target surface will appear at different places in the camera's sensing surface. The name of "triangulation" refers to the fact that the laser source, laser point on the target surface and the camera form a triangle. The distance between the camera and the laser source is assumed to be known. Also the angle of laser source corner is known. The angle of the camera corner can be

determined by looking at the location of the reflected laser signal in the camera's FOV. These three pieces of information can be used to calculate the size of the triangle and gives the position of the laser signal (represents the point on the target surface) of the triangle. Instead of using a single laser dot, a laser scanner uses stripes to scan across object surfaces. The advantages of this technique include high accuracy and high acquisition rate.

1.2.4. Moiré fringes

Two precisely matched pairs of gratings are used to create an interference pattern for the surface measurement in the basic Moiré technique. This technique can be classified into two categories: projection moiré [Cardenas-Garcia et al., 1991] and shadow moiré [Livnat and Kafri, 1983]. Figure 1.9 shows a schematic diagram of the two techniques. For measurement systems based on projection moiré, projected light is spatially amplitude modulated by the grating. Once the light is reflected by the surface, the grating before camera demodulates it and creates interference fringes whose phases are proportional to range [Matsumoto et al., 1991]. The resulting interference pattern shows contour lines for surface with equal height, but it does not give information about the corresponding depth values. Instead of using two gratings, shadow moiré uses only one grating. However, it is usually difficult to apply it to the measurement of large objects as the size of grating usually needs to be increased to guarantee the coverage of fringe patterns on object surface. As Moiré technique has phase discrimination problems when the surface doesn't show smooth shape variations, this technique is mostly used in measuring objects with relatively large flat surfaces and barely any height variations [Moore et al., 1979].

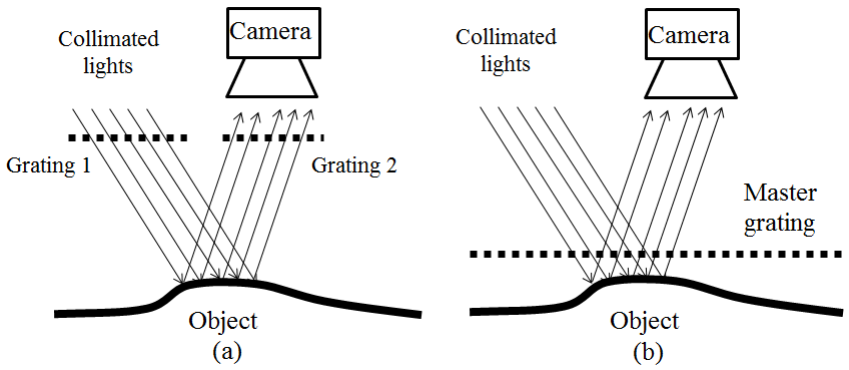

Figure 1.9 Schematic diagram of moiré technique

1.2.5. Structured light

This technique is considered as an active triangulation based method for the measurement of 3D shape of an object using projected patterns and a camera system. Parallel stripes are the most widely used patterns in structured light projection. A coded fringe pattern is usually projected on an object surface. The depth information is then encoded in the deformed fringe patterns. A camera is usually used for recording the deformed patterns. The height information can be retrieved after decoding the image with deformed fringe patterns [Chen et al., 2000; Huang et al., 2003].

Another well-known technique that can be used to extract depth information is called binary coding [Vuylsteke and Oosterlinck, 1990]. There are two levels in this technique: 0 and 1. Multiple encoded stripe patterns are projected in sequence. Each pixel will obtain a specific code composed of 0s and 1s after all the patterns are projected. Then, the shape information can be retrieved by decoding the code. Although this technique can obtain good results while noise occurs, the resolution of the provided result cannot be very high. Increasing the number of patterns to be projected can increase the resolution. However, this will result in longer measurement time. An alternative technique to the binary coding is the multi-level grey coding. This technique uses multiple intensity levels to reduce the number of required fringe patterns

[Salvi et al, 2004]. Color-encoded fringe pattern has also been applied in this technique [Tajima, 1987; Geng, 1996; Liu et al., 2000; Pan et al., 2006].

The advantages of using this technique include full field measurement and good accuracy. Disadvantages include high implementation cost and longer measurement time (due to the necessity of projecting various structured light patterns). User should evaluate the advantages and disadvantages of various types of structured light measurement system and select the best tool for specific application requirements.

1.2.6. Interferometry

Optical interferometry technique has been widely used in surface measurement for a long time. Various methods have been developed to achieve shape measurement such as phase-shifting interferometry [Cheng, 1985; Creath, 1988], white light interferometry [Caber, 1993], and speckle interferometry [Joenathan et al., 1990]. These techniques are based on the analysis of generated interference fringe patterns from two beams (object beam and reference beam). A digital camera is always used to record the intensity changes in multiple images while the projected fringe patterns are phase-shifted. Physical quantity such as height is encoded into the periodic signal. It can be recovered by decoding the periodic signal and thus achieving the goal of measurement. Fringe patterns usually represent the dark and bright stripes of two-dimensional interferometric signals. They can be described by using spatial coordinates (x, y, z) and the temporal coordinate t:

$$I(x,y,z,t) = I_0(x,y,z,t) \cdot \left(1 + m(x,y,z,t) \cdot f\left(\Delta\varphi(x,y,z,t)\right)\right) \quad \text{.....(1.1)}$$

$I_0(x,y,z,t)$, is the average background value of the signal;

$m(x,y,z,t)$, is the contrast of fringe patterns (modulation);

$\Delta\varphi(x,y,z,t)$, is the optical phase encoding;

f, is the defining function of the fringe pattern profile, it could be a function of sinusoidal shape, a rectangular shape, or a trapezoidal shape.

Various applications have been developed based on this technique [Maack, 1995; Wang, 1996; Ding, 2000; Schmit, 2002; Barbosa, 2007; Jiang, 2010]

Several advantages of this technique include:

(1) Good capability of obtaining instantaneous spatial information, contrary to many other time consuming techniques that give information at single spatial point or array of points after scanning.

(2) High measurement resolution in nm scope. Combined with phase shifting technique, interferometric methods can achieve accuracies of 1/100 to 1/1000 of a fringe. Even accuracy of 1/10000 of a fringe has been achieved with dedicated optical configuration developed by [Trolinger, 1996].

(3) No shading problem of triangulation techniques.

After an optical measurement system is developed, several tests will usually be taken to evaluate the system performance. The tests generally include:

(1) Calibrate the developed system;

(2) Evaluate the accuracy of the developed system by measuring standard sample parts with known dimensions, material and surface finishes;

(3) Evaluate the speed and volume capacity of the developed system;

(4) Evaluate the repeatability and reproducibility;

(5) Recognize the sources of errors and uncertainties, and make compensations [Taylor, 1994].

Each 3D optical measurement technique has its own set of advantages and disadvantages. Interferometry technique can measure reflective and smooth surfaces fast and achieve good accuracy. However, it usually cannot deliver similar performance in measuring rough and low reflective surfaces. In addition, the cost of the 3D measurement system is another major concern for a system to be available for widespread use [Blais, 2004].

1.3 Research objectives

In this research, an advanced optical metrology system that can measure a variety of machined surfaces in three dimensions is developed. And a systematic framework to analyze obtained high definition surface measurements is proposed. Methodology can be used to connect surface quality with desired functionalities and process parameters to achieve improved product quality and reduced manufacturing costs are introduced. Specific objectives of this research are identified as follows:

(1) Develop an advanced experimental measurement system that can provide three dimensional measurements with good axial accuracy for surfaces of target objects with curvature and irregular texture. The complexity of the configuration in the proposed system is simplified by utilizing optical fibers directly to generate interference patterns on object surfaces. Since no optical lenses are used between the light sources and object surface, errors due to optical distortions are avoided. The system can be applied in precision manufacturing for various types of surface inspection due to its simplicity, flexibility, low cost and good accuracy. A phase map of measured surface is calculated based on optimized least squares estimation using the acquired series of images. This phase calculation algorithm does not require fixed value for phase shift and can calculate the wrapped phase map robustly.

(2) An improved phase unwrapping algorithm based on flood fill technique to improve the accuracy of image processing is proposed. The developed algorithm can conduct phase unwrapping under the guidance of a hybrid quality map that is generated by considering the quality of both the raw intensity images and the calculated wrapped phase map. This algorithm demonstrates good robustness to noises both in the original captured images and errors in calculated wrapped phase map.

(3) A systematic multi-scale surface characterization strategy of engineered surfaces by taking the advantage of high definition measurements is proposed. A two stage data analysis methodology is introduced. The first step focuses on characterization of generalized surface shape while the second step focuses on developing applications to extract specific surface details. Both the general surface shape information and surface details can be extracted from the high definition measurement, data analysis can be taken by focusing on different surface wavelengths with the consideration of process information. For example, assembly quality can be evaluated by considering the extracted general shape of a machined surface from the foam scale, and the tool wear of a cutting insert can be estimated by analyzing the extracted surface details in waviness scale. This strategy can help engineers to effectively evaluate the quality of machined surfaces and obtain meaningful information for process condition monitoring and control.

In summary, continuous improvement of metrology system and analytical methodologies are critical to the successful of manufacturing industry. These two areas have been addressed in this research. The connection between chapters can be described using Figure 1.10. Conventional GD&T specifications still provide the majority metrics used in manufacturing industry. With advances in the metrology systems, high definition measurements of engineered surfaces can be obtained (e.g., using digital holographic system), and surfaces that were either difficult or time-

consuming to be measured, can now be measured in a simple and fast way (e.g., using developed fringe projection system). Therefore, new surface features can be extracted and new metrics can be developed as supplemental tools or indicators to predict product's functionality and monitor the conditions of manufacturing processes. As manufacturing industry has embraced the digitalization for years, an increasing number of process knowledge and information is being stored in servers. This enables researchers and engineers to integrate new information in analysis of product quality and process condition conveniently.

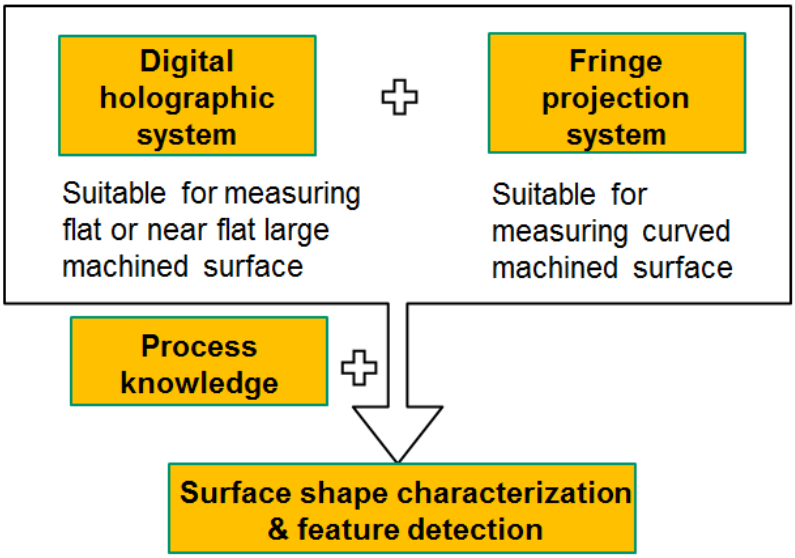

Figure 1.10 Connections among research topics

1.4 Organization of dissertation

This dissertation is organized as follows. Chapter 2 introduces the proposed system configuration (hardware) after a literature review of existing measurement systems. Then the algorithms used to calculate the phase information are explained. Demonstrations on the measurement of a gear tooth flank and beads processed by laser welding are presented to show the feasibility of the system in the measurement of three-dimensional surfaces of objects that are difficult to measure using conventional measurement systems. Chapter 3 focuses on the image

processing after obtaining wrapped phase map from Chapter 2. An improved phase unwrapping algorithm based on flood fill is introduced. Case studies are given to demonstrate the feasibility of the developed algorithm. Validation experiments are conducted in case studies to show that results are comparable with third party certified measurement systems. Chapter 4 gives a comprehensive introduction of the proposed strategy for conducting a multi-scale surface shape characterization. Case studies are given for the first step to illustrate how this strategy can be used to extract a generalized surface shape based on high definition measurements. Then, case studies of evaluating functionality of a product and extracting features for process condition monitoring are presented. Finally, Chapter 5 summarizes the contributions of the work. In addition, possible topics for future research work are also discussed.

CHAPTER 2 SYSTEM CONFIGURATION OF PROPOSED PHASE DISPLAY SYSTEM

2.1 Review of phase measurement systems in interferometry

2.1.1 Review of phase detection techniques

Conventional interferometry techniques always use two coherent light beams, one denoted as object beam that will be projected on object surface, and the other as reference beam that will be projected on a reference surface or mirror. The two reflected beams create the interference patterns that would be recorded for extracting the surface profile information. These techniques can provide high-resolution measurement with repeatability on the order of 1/100 of a wavelength [Besl, 1989; Creath, 1993]. However, the requirement of having a stabilized reference surface cannot always be met in many practical applications.

Alternative methods are projecting interference fringe onto the object surface. Ronchi grating [Srinivasan et al., 1985; Windecker and Tiziani, 1995] and Moire fringe patterns [Matsumoto et al., 1991; Indebetouw and Czarnek, 1992] are two of the most popular methods. Another technique that projects fringes is by the interference of two coherent beams on the object surface [Srinivasan et al., 1984]. Researchers also take advantage of electro-optic technology and using spatial light modulator to project fringes [Saldner and Huntley, 1997;

Servin et al., 1997]. This technique allows convenient adjustment of phase or spacing of the fringes without moving parts.

No matter which technique is applied to generate interference patterns, the goal remains the same that is to relate the location of captured fringes to surface profile. To achieve that, the interferogram must be analyzed to assign the phase of fringes at each location. During the early history of interferometry, phase quantification could hardly be obtained except at extreme values of fringe patterns. Phase values were recovered based on tracing the pixels that had the maximum or minimum intensity. Fringes had to be correctly ordered before the phase could be determined. The fringe patterns were simply photographed and overexposed to highlight these points. These processes were time-consuming and inaccurate because it was difficult to identify the signal from the noise [Reid, 1986]. In the 1960s, with the help of video cameras and computers, fringe patterns could be recorded and stored in a format which was more convenient for post-processing. The quality of measurement was improved with the implementation of new tools [Tsuruta and Itoh, 1969]. These methods were further replaced in the middle 1970s by a technique based on image processing which gave direct access to phase. One could extract phase difference from captured images. However the analysis of conventional interferograms can still be tedious. It requires the detection of coordinates of fringe centers and the data is analyzed from this point onwards [Creath, 1988; Malacara, 2005].

Phase-shifting interferometry (PSI) overcomes many disadvantages of conventional interferometry. It was introduced in 1966 by Carré [1966]. This technique eliminates the need of locating the fringe centers by recovering phase through a pixel-by-pixel calculation of a series (at least three) measured images. Early applications were reported by [Bruning, 1974; Wyant, 1975].

It has been applied in various application fields because of its advantages that can be described as follows:

(1) Less sensitive to stationary noise in the range on which the phase ϕ varies;

(2) Algorithms can be defined that accommodate with poorly contrasted fringe patterns;

(3) Uncertainty of the results is limited by the signal to noise ratio of the fringe patterns;

(4) Analysis of PSI images is much simpler and does not require the location of fringe centers;

(5) The process of fringe patterns analysis can be fully automated;

(6) High resolution can be obtained to the order of 1/100 of a wavelength.

In PSI, the phase shift can be obtained either in discrete steps (also denotes as phase-stepping interferometry) or by a constant changing rate as the detector is read out [Wyant, 1975]. It can be shown that by taking three or more measurements of the object surface as the projected fringe patterns are shifted, it can provide high resolution 3D reconstruction image rapidly with minimal computational investment [Gorthi and Rastogi, 2010, Wyant, 2013].

Another alternative technique for fringe analysis is based on the Fourier transform [Takeda et al., 1982; Bone et al., 1986; Roddier, 1987] that could calculate the phase information from a single image. As the developed measurement system in this research is based on PSI technique, the next section will review some of the commonly used system designs based on this technique. Other systems built using different techniques are not within the scope of this research.

2.1.2 Review of measurement system configurations using phase-shifting interferometry

Phase-shifting technology has been adapted to a variety of interferometer types such as Twyman-Green, Mach–Zehnder, and Fizeau [Goodwin, 2006]. Figure 2.1 shows the diagram of classical system designs of these three types. Taking the Mach-Zehnder interferometer as an example, a piezoelectric transducer (PZT) can be installed on mirror 2. Then a changing voltage can be used as input to drive the PZT to produce vibration of the mirror. Thus, the phase of the reference beam can be changed. This technique is one of the most widely used methods in commercially available interferometers. Besides using PZT to achieve phase shifting in optical system, two other methods can also be used to achieve the same result: (1) electro-optic modulators; and (2) acousto-optic modulators.

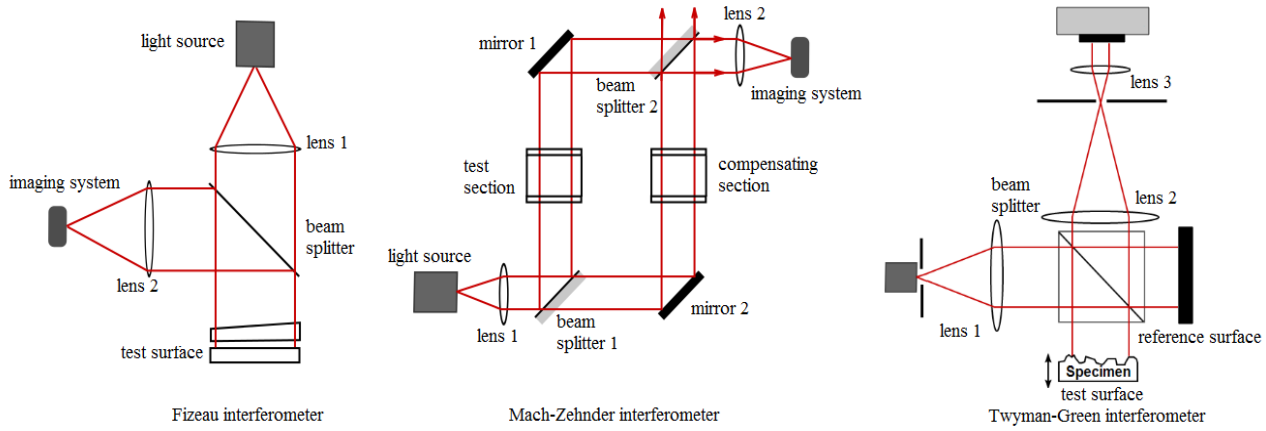

Figure 2.1 Basic configurations of three commonly used interferometers [Goodwin, 2006]

The phase-shifting technique is also applicable for common path configurations such as point diffraction [Bueno, 2010] and lateral shearing interferometers [Nomura, 1998]. Generally, the phase shifting technique can be adapted to almost any system that uses fringes for measurement such as holographic [Yamaguchi, 2001] and speckle interferometry [Takeda, 1994].

Phase-shifting interferometry technique requires at least three images to be measured for the phase calculation. The time elapsed between measurements could be slightly different which may result in non-equal phase changes. To overcome this deficiency, a method called simultaneous phase shift measurement has been developed by [Smythe and Moore, 1984]. By using polarizers and multiple cameras, phase-shifted images can be recorded simultaneously [Koliopoulos, 1991]. Figure 2.2 shows the diagram of a system configuration using this technique [Onuma, 1993]. Three digital cameras have been installed to record phase shifted interferograms. This technique shortens the data acquisition time compared to other techniques, however, the use of many cameras and other optical components make the system complex. It creates a challenge in the alignment of all the optics, especially since the cameras have to be aligned pixel-to-pixel to obtain the best results.

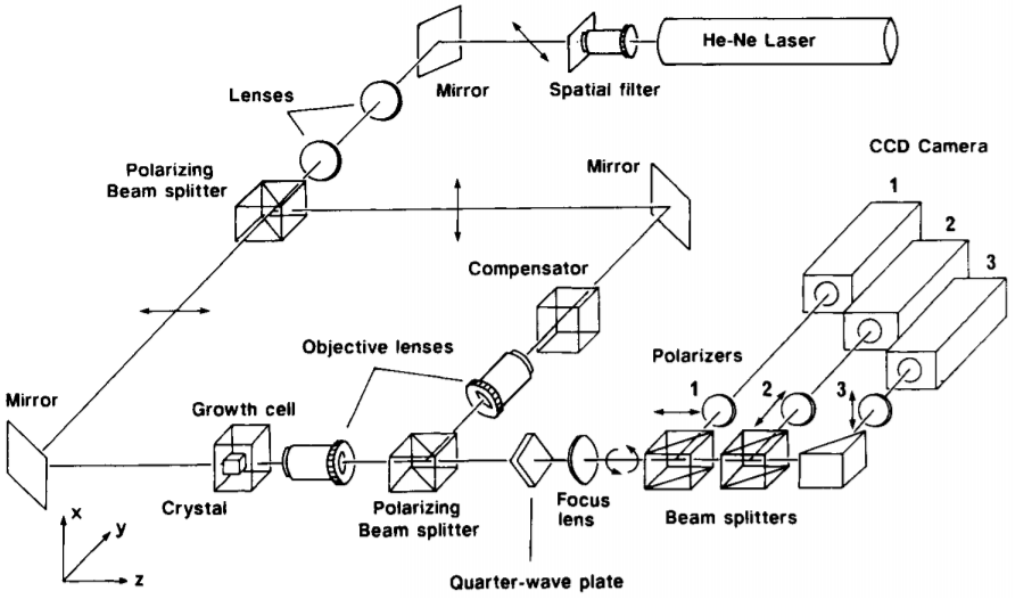

Figure 2.2 Optical system using polarizers and quarter-wave plate to achieve simultaneous phase-shifting measurement [Onuma, 1993]

In summary, most of the current shape measurement systems based on phase-shifting interferometry include several or a series of lenses and mirrors. Moreover, many applications use collimated fringes that require the size of the object must be less than the optics. For instance,

if we want to measure a 300 x 300 mm^2 engineering surface, the optics must be on the order of 300 mm or larger. Obviously, the complexity and cost of such an optical system would become very complicated, heavy and expensive. Moreover, the entire system would be more fragile and difficult to be installed or moved.

If a new measurement system can achieve the same level of accuracy with a simpler system design, it will be desirable and applicable in broad fields. In this research, a measurement system that uses diverging fringe patterns is proposed to satisfy the demand that minimizes the size and complexity of the configurations of optics.

2.2 Introduction of the proposed system

2.2.1 System configuration

Generally speaking, the hardware of a shape measurement system based on fringe projection includes: (1) a fringe pattern generation component; (2) an imaging sensor for recording deformed fringe patterns on an object surface; and (3) components which will store and process acquired fringe pattern data.

Figure 2.3 describes the layout of the proposed system. A laser beam at a fixed wavelength (842.4 nm for current experimental system) is generated from a source. A 50/50 beam splitter is used to separates the laser beam into two identical beams.

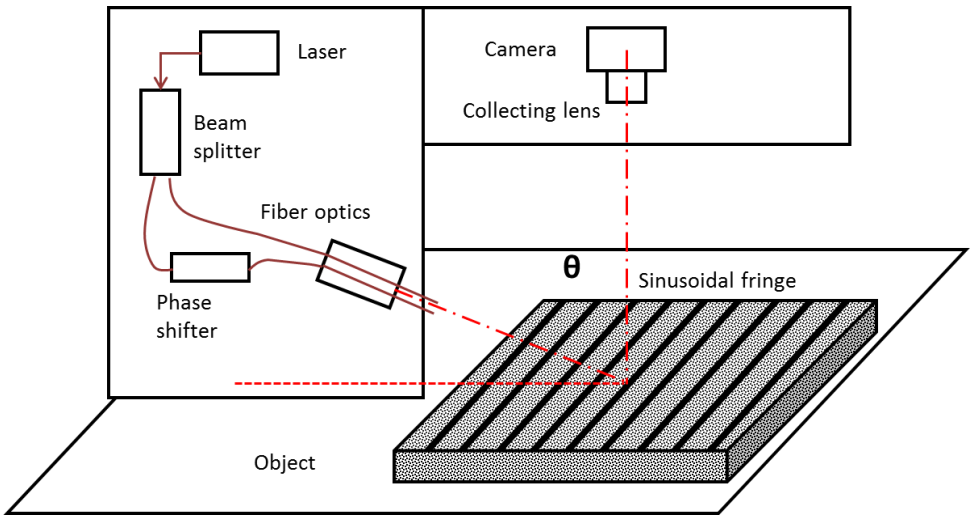

Figure 2.3 Schematic diagram of the proposed system

A phase-stepping technique is used in the developed system to generate phase-shifted fringe patterns.

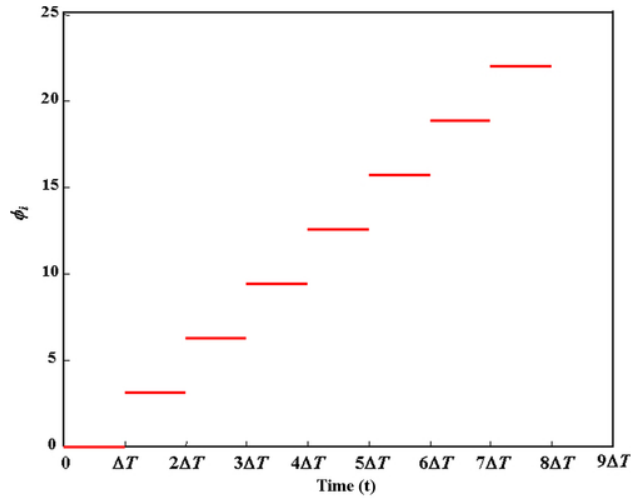

Figure 2.4 Illustration of phase stepping interferometry

At location (x, y) the instantaneous signal can be described as:

$$I(t) = a + b \cdot \cos(\Delta\varphi + 2\pi \cdot \phi(t)) \quad \text{.....} \quad (2.1)$$

a and b are the background intensity and modulation amplitude at time t. $\Delta\varphi$ is the original phase at this particular pixel that is the quantity we want to obtain and then can be

converted into height. If the signal is integrated by the detector during the time interval Δt_i during which $\phi(t)$ is actually a constant and equals to ϕ_n, then the above equation can be written as:

$$E_n = a + b \cdot \cos(\Delta\varphi + \phi_n) \quad \text{..... (2.2)}$$

The values registered for each phase step follow a sinusoidal wave, which is represented with the dot line with the same modulation and phase. This is how the phase is shifted in the developed system. Successive phase values are imposed on the signal (Figure 2.5).

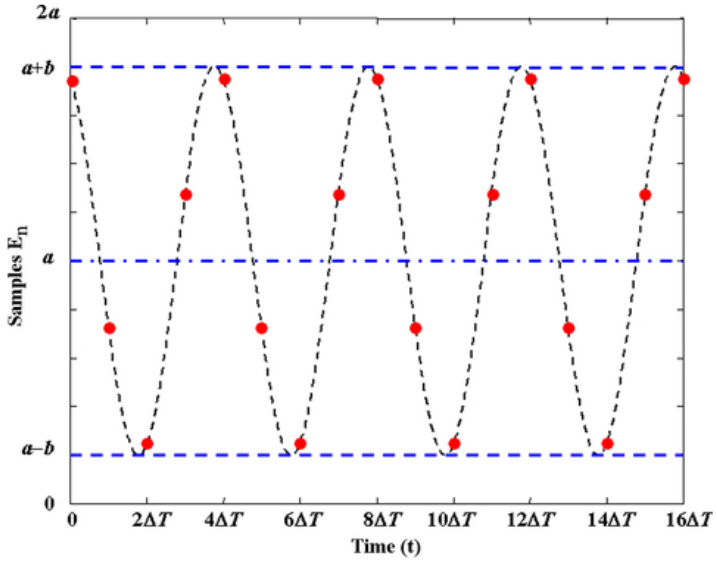

Figure 2.5 Registered samples shown on sinusoidal wave

The phase shifted fringe patterns are projected directly onto the object surface at an angle of θ (illustrated in Figure 2.3) . A digital camera of 2048 x 2048 pixels is placed above the object surface which will record the changing fringe patterns on the object surface. A series of N phase shifted images are captured and transferred to a computer for each measurement. Developed algorithms will be applied in sequence to the set of these images to obtain a single wrapped phase map. To obtain the final three-dimensional height map of a measurement, the wrapped phase map needs to be unwrapped and adjusted.

The system has flexibility to be adjusted for the measurement of different objects. The projection angle θ is adjustable. Changing the angle θ will affect the light distribution over the object surface. Operator can adjust this angle by looking at the real time image captured from camera to make sure the area of interest is completed illuminated. Operator should be aware of the change of angle θ will also affect the height change represented by per 2π phase change. The distance (denoted as d) between the two fibers is also adjustable. By changing the distance d , the density of the fringes will change. Hence, the resolution of the measurement can also be changed. The system is capable of measuring objects from a near-flat surface to surface with curvatures. The chosen field of view depends on the required lateral and axial resolution of the measurements.

Figure 2.6 shows the whole experimental system in the laboratory. The measurement chamber includes all the components shown in Figure 2.3. The entire chamber is mounted on a platform, which is isolated from excessive vibration. The system controller is used to turn on/off the laser and stepping voltage and control system data collection timing. The controller connects both the computer and the camera. When the laser is on, fringe patterns will be projected on the surface, the operator can monitor it in live video on the computer screen. When a "measure" command is issued, the system will automatically collect N frames continuously and store them in the computer. The phase information is calculated when each data acquisition process is completed.

Figure 2.6 Illustration of experimental system

The camera pixel spacing at the object was determined from the array spacing and the optical magnification of the camera lens system. The digital camera array pixel spacing is 7.4 x 7.4um. The optical magnification can be estimated from the focal length of the lens and the distance of the lens to the camera plane (Figure 2.7) or a calibration artifact can be used.

$$m = \frac{h'}{h} = \frac{f}{x + f} \quad \text{..... (2.3)}$$

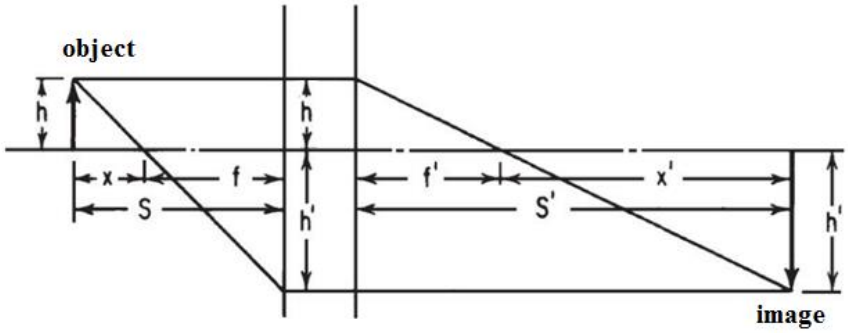

Figure 2.7 Estimation of optical magnification

2.2.2 Advantages of the proposed measurement system

Compared to other aforementioned conventional optical system using phase-shifting interferometry in which a number of different optical components are installed between the laser source and the object surface, the proposed system does not require any lens, only a 50/50 beam splitter is required to separate the laser beam into two identical beams. This innovative design has advantages listed as follows:

(1) The laser beams will not be distorted before reaching the target surface since they do not go through a series of lens, in which distortions are inevitable;

(2) It has good flexibility to measure various objects at high accuracy (it has been demonstrated that phase shifting interferometry measurements can be generated that have residual errors less than 1/1000 of a wavelength, [Schwider et al., 1983; Cheng and Wyant, 1985]);

(3) The system has a much simpler configuration such that it can be adjusted for each specific application.

(4) A calibration is needed to get the projection angle and scale factor, no other complicated alignment is needed;

(5) The cost of the entire system is relatively low.

2.3 Phase calculation in the proposed measurement system

2.3.1 Review of the phase calculation methods

Acquired images with deformed fringe patterns need to be demodulated to obtain the wrapped phase distribution or phase map. The quality of an obtained phase map plays an important role in phase unwrapping. To obtain the phase map in high quality, two

implementations can be applied. The first option is to use highly accurate optical components in system to guarantee the acquired images are at the best quality. For instance, Kwon and Kim [2011] developed an optical system to suppress vibrations in measurement. This kind of measurement system always has a relatively high cost and is difficult for installation. Moreover it could be difficult to take measurement due to the restriction of the layout of hardware. Therefore, the second option that aims to develop improved algorithms is usually considered as the better and more convenient option in calculating the phase map. The criteria for a good algorithm should be: (1) immune or robust to noise; and (2) computationally efficient.

Multiple-step phase shift is the most widely used technique to calculate phase data information from three or more fringe patterns. To calculate the phase $\Delta\varphi$ in Eq. (2.2), at least three images are required. Algorithms called 3-frame, 4-frame, 5-frame, 7-frame, average 3&3 and average 4&4 are among the most widely applied methods. Good reviews about these algorithms can be found in [Novák, 2008; Zhang, 2012]. These algorithms always require accurate known phase shift either by calibrating the phase shifter or by measuring the amount of actual phase shift each time. The Carré method [Carré, 1966] is independent of the phase shift by assuming the phase is shifted by certain ϕ between every two consecutive measurements. The major advantage of the Carré algorithm is that phase shifts do not need to be calibrated, although they still need to be equal.

It is a significant challenge to keep the desired phase shift stable between frames considering that many sources of errors (e.g., incorrect phase shifter calibration, vibration, or air turbulence) may cause incorrect phase steps. Using only three or four measurements is not robust for producing correct phase information. Researchers prefer to develop supplementary

algorithms that can reduce the calculation error brought by inconsistent phase shifts over using complicated optical configuration to keep precise phase shift.

One of these approaches to determine the phase is using a least squares fit on more than three measurements. The least squares estimation (LSE) method was introduced by [Morgan, 1982] to minimize the intensity error between the imaged intensity map and the estimated one on the parameter of the measured phase. The commonly used version of LSE was established by [Greivenkamp, 1984]. Greivenkamp used the same interference equation but minimized the intensity errors according to three parameters (background, cosine, and sine function of the phase shifter). Greivenkamp's LSE is linear and removes several restrictions when designing the phase steps.

The benefit of using a least squares fit is that the phase steps do not need to be evenly spread and can be spread over a range greater than 2π, while three step or four step algorithms usually have to use a fixed 90 degree for phase shifts. For the system used in this research, robust least squares fit is used to obtain a cosine function directly from all the N frames measured.

Many phase calculation algorithms have been developed and each of them can be used under specific situation. However, no algorithm can work consistently well when many sources of errors present. Each algorithm is usually focusing on solving one particular problem and requires additional information to cover all cases.

2.3.2 The robust phase calculation algorithm

The normal procedure for performing the least squares fit can be described as follows [Greivenkamp, 1984]. Considering Eq. (2.2), we can rewrite it by applying the properties of trigonometric formulas [Sharma, 2004].

$$E_n = a + b \cdot \cos(\Delta\varphi + \phi_n) = a + b \cdot \cos(\Delta\varphi) \cdot \cos(\phi_n) - b \cdot \sin(\Delta\varphi) \cdot \sin(\phi_n) \quad \text{(2.4)}$$

In Eq. (2.4), the original unknowns a, b and $\Delta\varphi$ can be replaced by $a_0 = a$, $a_1 = b \cdot \cos(\Delta\varphi)$ and $a_2 = b \cdot \sin(\Delta\varphi)$.

$$E_n = a_0 + a_1 \cdot \cos(\phi_n) + a_2 \cdot \sin(\phi_n) \qquad n \in [1,2,..., N] \quad \text{(2.5)}$$

The least square function now can be described as:

$$\varepsilon = \sum_{n=1}^{N} [E_n - (a_0 + a_1 \cdot \cos(\phi_n) + a_2 \cdot \sin(\phi_n))]^2$$

Error ε is minimized by differentiating with respect to each of the three unknowns and equating these results to zero:

$$\frac{\partial \varepsilon}{\partial a_0} = \frac{\partial \varepsilon}{\partial a_1} = \frac{\partial \varepsilon}{\partial a_2} = 0 \quad \text{(2.6)}$$

Therefore, we can obtain a linear system of three equations with three unknown parameters:

$$\begin{aligned}
&\sum_{n=1}^{N} a_0 + a_1 \cdot \cos(\phi_n) + a_2 \cdot \sin(\phi_n) = \sum_{n=1}^{n=N} E_n \\
&\sum_{n=1}^{N} a_0 \cdot \cos(\phi_n) + a_1 \cdot \cos^2(\phi_n) + a_2 \cdot \cos(\phi_n) \sin(\phi_n) = \sum_{n=1}^{n=N} E_n \cdot \cos(\phi_n) \\
&\sum_{n=1}^{N} a_0 \cdot \sin(\phi_n) + a_1 \cdot \cos(\phi_n) \sin(\phi_n) + a_2 \cdot \sin^2(\phi_n) = \sum_{n=1}^{n=N} E_n \cdot \sin(\phi_n)
\end{aligned} \quad \text{(2.7)}$$

The simultaneous solution of these three equations produces the least square result. To simplify the expression, we can rewrite it as:

$$A(\phi_n) X = B(E_n, \phi_n) \quad \text{(2.8)}$$

$$A(\phi_n)=\begin{bmatrix} N & \sum_{n=1}^{n=N}\cos(\phi_n) & \sum_{n=1}^{n=N}\sin(\phi_n) \\ \sum_{n=1}^{n=N}\cos(\phi_n) & \sum_{n=1}^{n=N}\cos^2(\phi_n) & \sum_{n=1}^{n=N}\cos(\phi_n)\sin(\phi_n) \\ \sum_{n=1}^{n=N}\sin(\phi_n) & \sum_{n=1}^{n=N}\cos(\phi_n)\sin(\phi_n) & \sum_{n=1}^{n=N}\sin^2(\phi_n) \end{bmatrix},$$

$$X=\begin{bmatrix} a_0 & a_1 & a_2 \end{bmatrix}^T,$$

$$B(E_n,\phi_n)=\begin{bmatrix} \sum_{n=1}^{n=N}E_n & \sum_{n=1}^{n=N}E_n\cdot\cos(\phi_n) & \sum_{n=1}^{n=N}E_n\cdot\sin(\phi_n) \end{bmatrix}^T$$

Take the inverse of Eq. (2.8)

$$X=A^{-1}(\phi_n)B(E_n,\phi_n) \quad \text{(2.9)}$$

The phase shift value ϕ_n is usually a known value, although it changes around the desired number due to perturbations, so we can take the average of all the ϕ_ns. Hence, we can obtain a_0, a_1 and a_2. The optical phase is given by:

$$\Delta\varphi=\arctan\left(\frac{a_2}{a_1}\right) \quad \text{(2.10)}$$

The main disadvantage of the least squares fit is its sensitivity to outliers. Outlier could be pixel that has saturation or no modulation in a single frame. These outliers have a large influence on the fit because squaring the residuals magnifies the effects of these extreme data points. Therefore, a robust least squares fit based on bisquare weights is selected for phase calculation in our application [Kong and Kim, 1994].

The bisquare weights are used to minimize a weighted sum of squares, where the weight given to each data point (from the N measurements at the pixel location) depends on how far the point is from the fitted curve. Points close to the curve get full weight. Points farther away get reduced weight as small as zero. The algorithm follows this procedure:

(1) Fit the model by weighted least squares (the initial weights could be set the same for all data points);

(2) Calculate the adjusted residuals and standardize them. Adjusted residuals are given by: $r_{adj} = \frac{r_i}{\sqrt{1-h_i}}$ ……. (2.11)

r_i are the usual least squares residuals and h_i are scalars used to adjust the residuals by reducing the weight of data points which have large effects on least squares fit. Standardized adjusted residuals are given by

$$u = \frac{r_{adj}}{K_s} \text{ ……...…….. (2.12)}$$

K_s is a weighting constant with a default setting at 4.685 [Coleman et al., 1980]. s is the robust variance given by $\frac{MAD}{0.6745}$, MAD is the Median Absolution Deviation of the residuals [Street et al., 1988] and the constant 0.6745 makes the estimate unbiased for normal distribution;

(3) Robust weights are calculated as a function of u . The bisquare weights are given by

$$\omega_i = \begin{cases} \left(1-(u_i)^2\right)^2 & |u_i| < 1 \\ 0 & |u_i| \geq 1 \end{cases} \text{ ……...….. (2.13)}$$

(4) The final results can be obtained once convergence is achieved. It should be noted that using bisquare weighting function can have difficulties in converging or may yield multiple solutions. This problem does not occur in our application due to the simplicity of the structure of acquired data (a series of phase-shifted images is collected. Then values of each point on every frame are extracted to calculate the phase value. Normal data shows simple sinusoidal pattern).

2.4 Demonstration of the proposed system in the measurement of laser weld samples

The laser welds on electrical vehicle battery packs are critical to the functional performance, system reliability and safety. However, welding the electrodes on the battery pack with consistent high integrity has proven to be very challenging. Therefore, the finished weld seam needs to be inspected carefully. For instance, operator needs to detect and measure the depth and total length along a weld of voids (holes) and cut-throughs (linear defects where the welding laser cuts almost all the way through the welded metal). High accuracy and fast processing speed (usually require measurement to be completed in seconds) are required on these measurements, which puts challenge on current measurement systems.

For the given test samples of Aluminum laser welds (Figure 1.3 in Chapter 1), two metrics are of interest: the depth of a laser weld seam and the percentage of the cut-throughs in the total length. Acceptable criteria for given samples are: (1) The depth of the cut-through is less than 160 μm; and (2) The percentage of defective cut-through is less than 17% of total length . Figure 2.8 gives an illustration of these two metrics.

The developed measurement system was used to measure the test samples. The projection angle is set at 68 degrees. The width of one fringe includes approximately 13.3 pixels. The horizontal resolution is 23.53 μm/pixel.

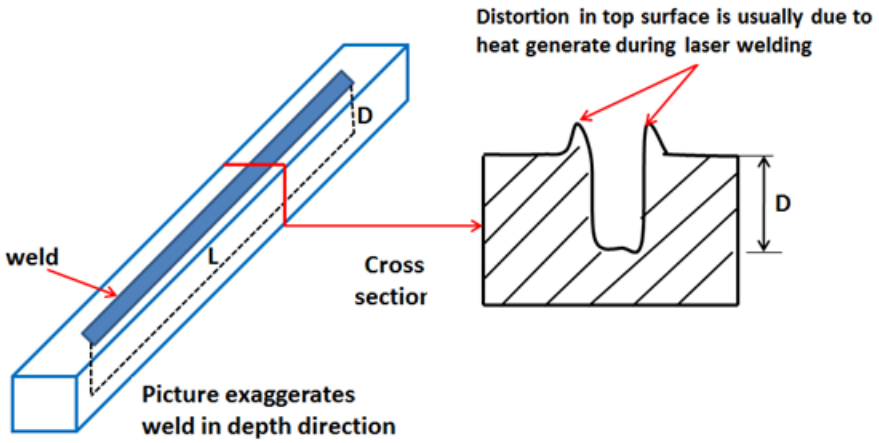

Figure 2.8 Geometrical description of a laser weld seam

A height map reconstructed with the bisquare least square algorithm for the aluminum weld is shown in Figure 2.9. The defective cut-through has been identified and two traces are selected to show the cross section of the cut-through.

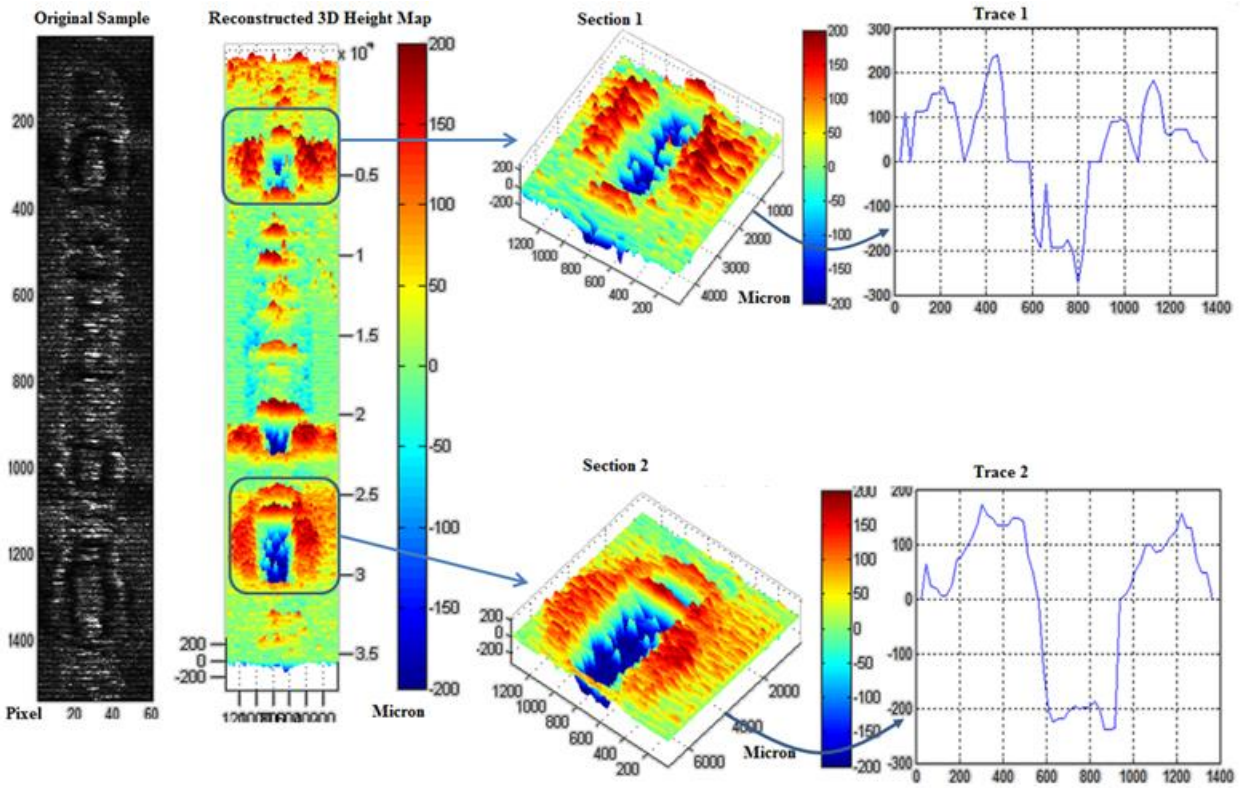

Figure 2.9 Reconstructed height map of a laser weld sample

The calculated height map of the weld will be the input to calculate the desired metrics. The procedures are described as follows:

1) Find out all pixels that are at least 160 μm deep (Th1 = -160 μm);
2) Evaluate the weld row-by-row and only mark objects that have at least Th2 continuous pixels (Th2 = 5 in this case study);
3) Evaluate the weld column-by-column and only mark objects that have at least Th3 continuous (Th3 = 5 in this case study) pixels. Most of voids found in weld have a nearly round shape. This is why we look at the weld in two perpendicular directions consecutively. true voids are recorded when both conditions are met;
4) The percentage of voids in total length of weld will be calculated;
5) The location and height of all selected pixels will be saved in an excel file. These final pixels will be plotted on a gray scale image for the purpose of demonstration.

For this given test sample, the total length of the weld is 32.73 mm. Percentage of the voids and cut-throughs is 22.43%, which exceeds the acceptable value. Green dots shown in Figure 2.10 represent the identified pixels at least 160 μm deep.

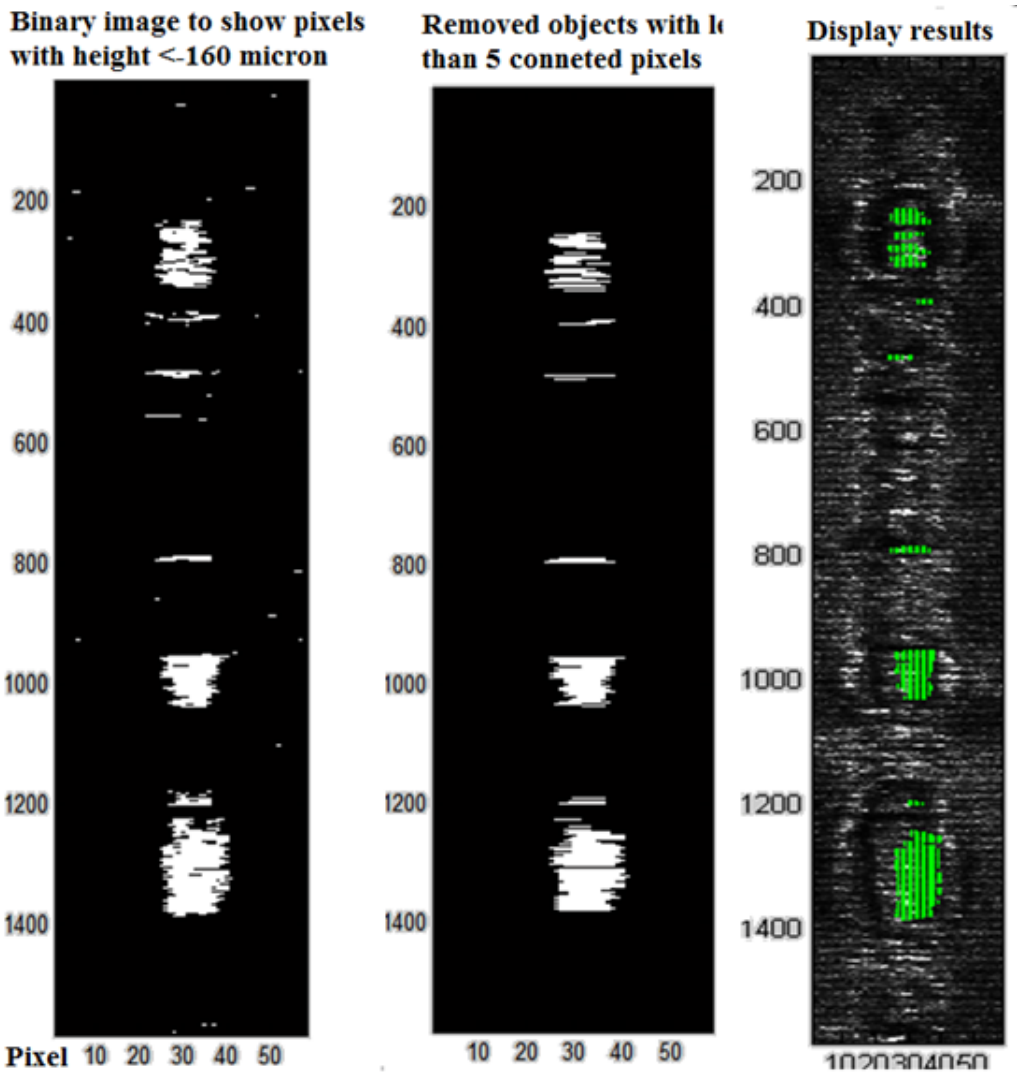

Figure 2.10 Final result of detected defective areas on a laser weld sample

2.5 Validation test

2.5.1 Equipment introduction

Certified third party measurement systems are used to validate that the sample results measured by the developed fringe projection system are acceptable. Olympus LEXT OLS4000[1] laser microscope system is used to conduct the validation test.

The OLS4000 is equipped with a confocal optical system that only captures images that are in-focus. As only thin image planes of same height are captured at a fixed position, a 3D height image is constructed by letting the objective lens move in Z direction at high accuracy. If the area of interest of a test sample is larger than the visual field range of OLS4000, it has a stitching function that is able to combine multiple images together to form one consolidated measurement. Figure 2.11 shows an image of the OLS4000 system used in this validation experiment. The OLS4000 has five different objective lenses for different magnification usage. The 20x lens is used in this experiment. Resolutions in the X, Y, and Z directions are 0.625 μm, 0.625 μm and 0.01 μm, respectively. The scanning step in Z direction is 0.1 μm per layer. And the corresponding Field Of View (FOV) is 640 μm by 640 μm. Table 2-1 lists some other key specifications of the OLS4000 system.

[1] http://www.olympus-ims.com/en/metrology/ols4000/

Figure 2.11 Olympus LEXT OLS4000 system[2]

Table 2-1 Olympus LEXT OLS4000 specifications

Optical System				**UIS2 Optical System (Infinity-corrected)**
Total Magnification				**108x - 17280x**
Field of View				**2560x2560 - 16x16 µm**
Microscope Frame	**Observation Method**			**BF/DIC/Laser/Laser Confocal DIC**
	Laser			**405 nm Semiconductor Laser**
	White Light			**White LED**
	Focus	**Z Stage**	**Stroke**	**100 mm**
			Maximum Height of Specimen	**100 mm**
		Z Revolving Nosepiece	**Stroke**	**10 mm**
			Resolution	**0.01 µm**
			Repeatability	**σn-1=0.012 µm**
	Objective Lens			**5x, 10x, 20x, 50x, 100x**
	Optical Zoom			**1x - 8x**
Stage	**Motorized Stage**			**100x100 mm**
Dimensions				**276(W)x358(D)x405(H) mm**

2.5.2 Validation test of laser weld samples

During the validation test, we measured areas with defects on these five samples (Figure 2.12) via OLS4000 system and compared them with the results obtained from the fringe projection system. Two cases are presented below to illustrate the side-by-side comparisons of two types of defects.

[2] http://lnf-wiki.eecs.umich.edu/wiki/Olympus_OLS_4000_LEXT

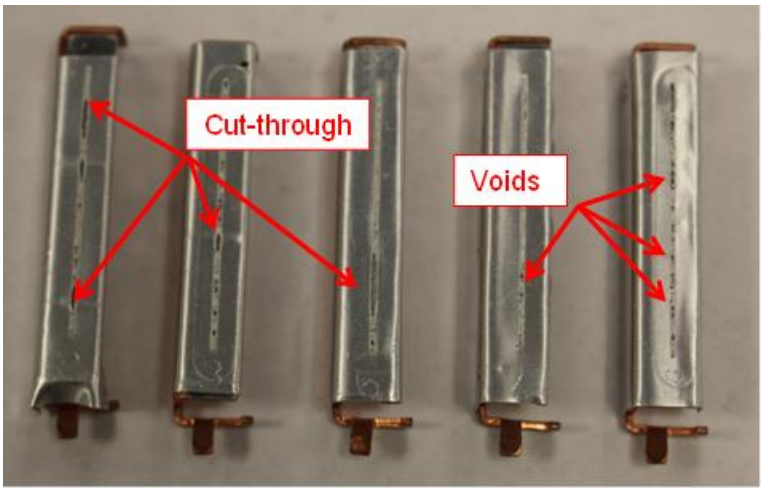

Figure 2.12 Illustration of five laser weld samples (No. 2, 3, 5, 7, and 8, from left to right)

A void on the laser weld sample No. 7 was measured by both systems. Figure 2.13 shows the measurement result obtained from the fringe projection system. The resolutions in X and Y directions are both 23.53 μm. The resolution in Z direction is 0.1 μm. Figure 2.13 (a) shows a photo of the original sample with the void highlighted in a red box. Figure 2.13 (b) is the reconstructed 3D image. Figure 2.13(c) is a zoom-in image of the void. The highest point is 322.7 μm above the weld surface and the lowest point is -230.4 μm. This gives us a peak-to-valley value of 553.1 μm.

Figure 2.14 presents the results obtained from OLS4000. Figure 2.14(a) displays the void defect under microscope and Figure 2.14(b) shows the 3D height map. The size of both images is 1,209 μm by 1,212 μm (four images are stitched together to cover the void defect). Unlike the fringe projection system that used the un-welded surface area as datum, OLS4000 automatically set the lowest point it could measure as zero. Therefore, the peak-to-valley value is the best metric to compare results from two systems. And this value is 567.3 μm in comparison with 553.1 μm obtained from the fringe projection system. The error is approximately 2.50%.

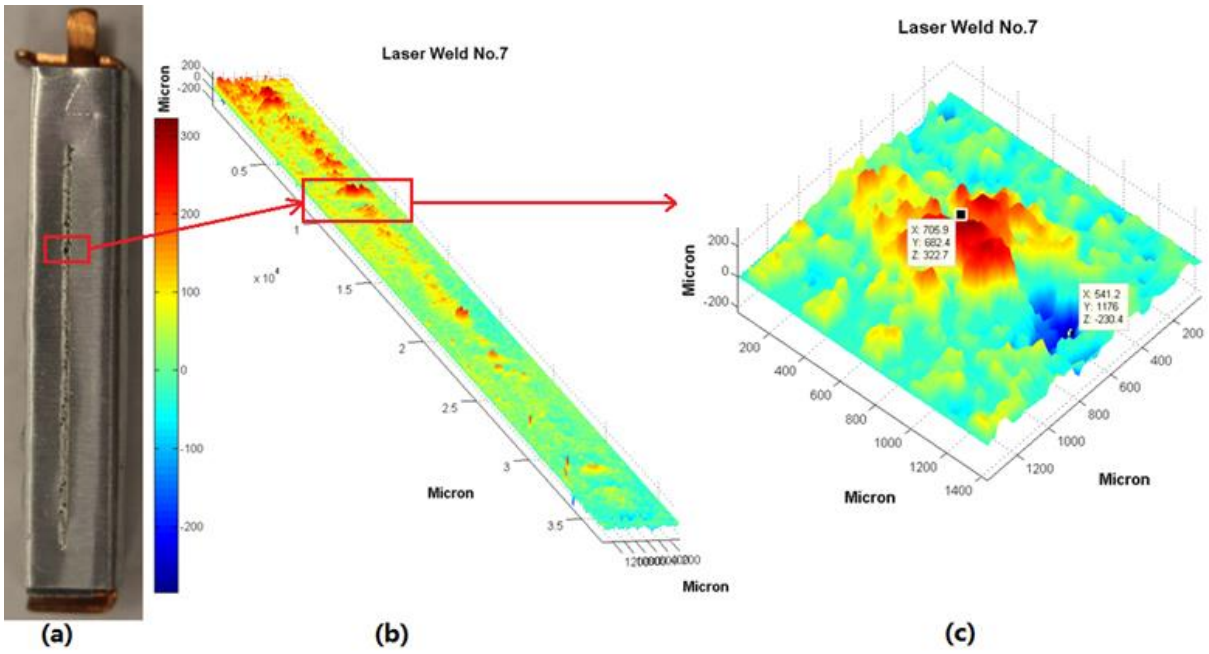

Figure 2.13 Measurement result of laser weld No. 7 via fringe projection system: (a) image of original sample; (b) reconstructed 3D image; (c) zoom-in height map of a void

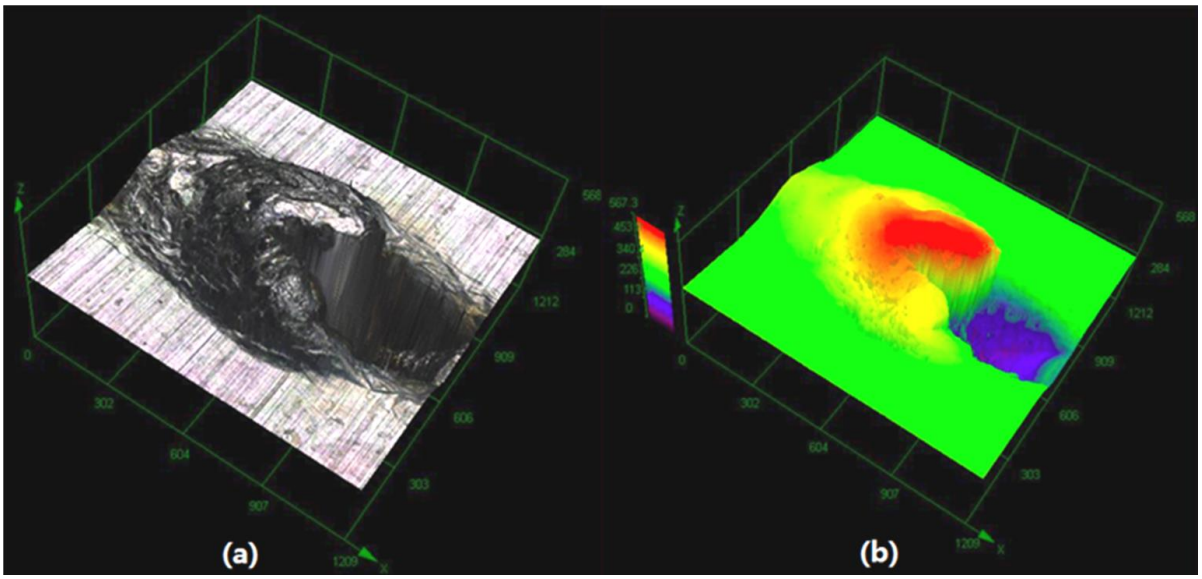

Figure 2.14 Measurement result of laser weld No. 7 via OLS4000: (a) original image under microscope; (b) reconstructed 3D image of the void

A cut-through on the laser weld sample No. 2 was measured by both systems. Figure 2.15 displays the measurement result obtained from the fringe projection system.

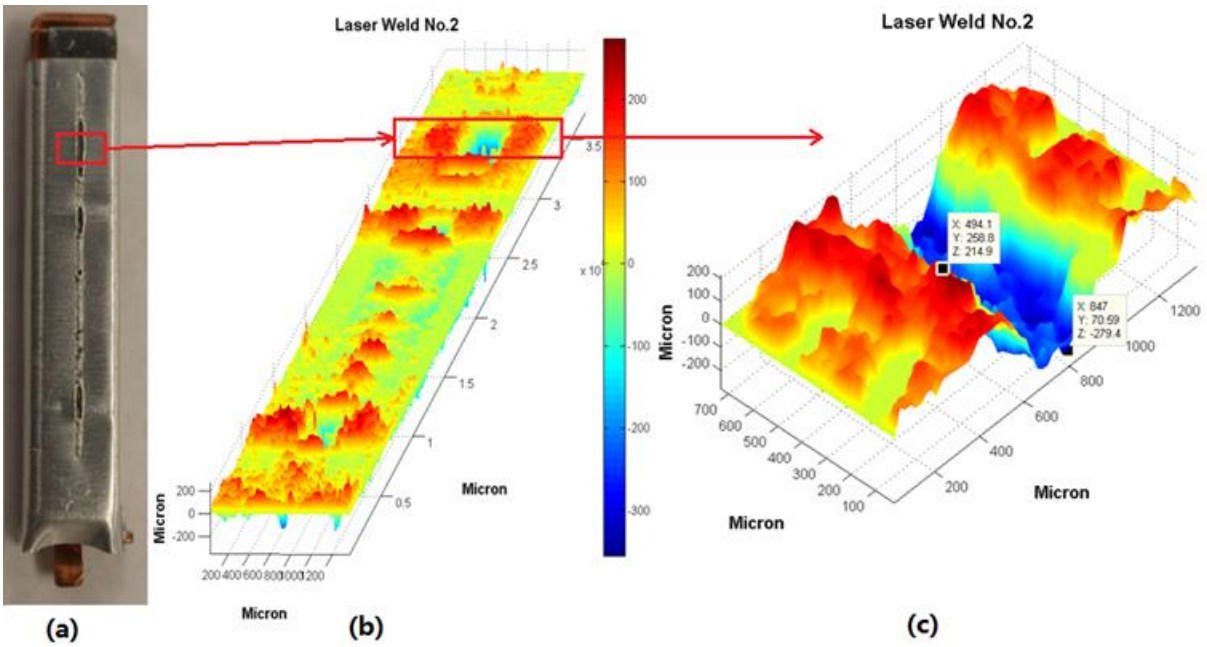

Figure 2.15 Measurement result of laser weld No. 2 via fringe projection system: (a) image of original sample; (b) reconstructed 3D image; (c) zoom-in height map of the cut-through

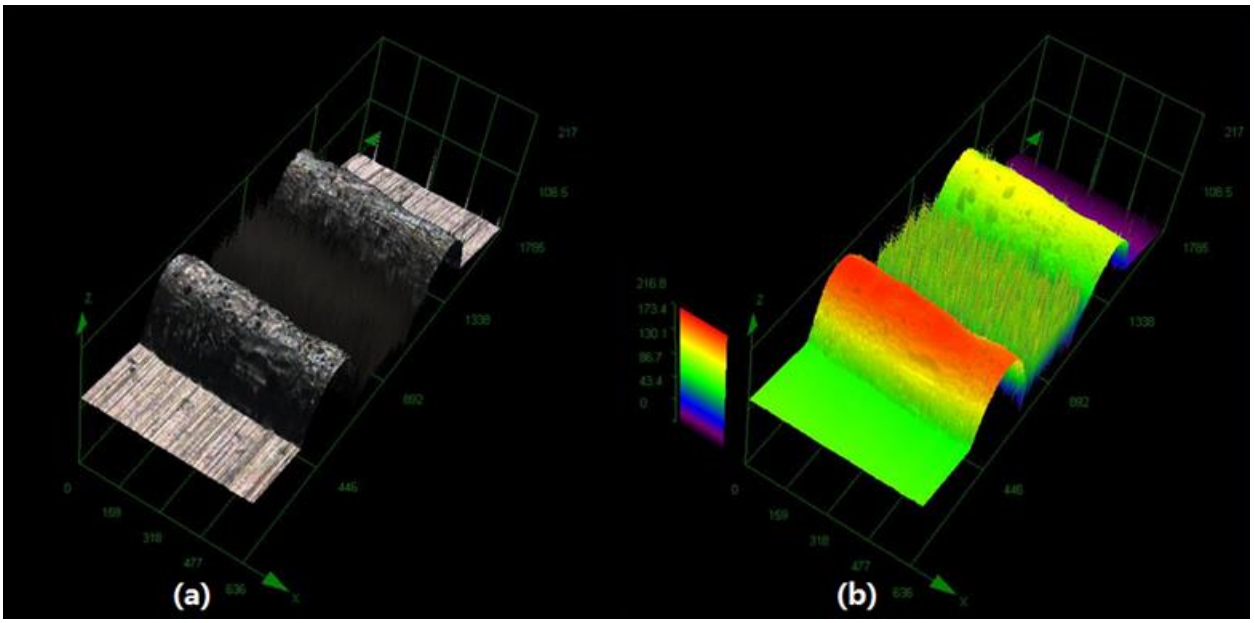

Figure 2.16 Measurement result of laser weld No. 2 via OLS4000: (a) original image under microscope; (b) reconstructed 3D image of the cut-through

The resolutions in X, Y, and Z directions are the same as shown previously in sample No.7. The highest point is 214.9 μm above the weld surface and the lowest point is -279.4 μm. This gives us a peak-to-valley value of 494.3 μm. Figure 2.16 shows the results obtained from OLS4000 of the same sample. The image size is 625 μm x 1,785 μm (three images are stitched

together to cover the cut-through). We can see the OLS4000 was unable to measure the deep through of the sample, it only returned lots of noise spikes as results. Thus, the OLS4000 marked the lowest point on the right side of the un-welded area of the sample. And the peak value of the measurement is 216.8 μm with regards to the identified zero point on the side of weld sample.

In order to conduct comparison on the results obtained from these two systems, we need to make some adjustment on the result measured from the fringe projection system. First of all, the valley data is excluded. Secondly, find the lowest point on the right side of un-welded surface and mark it as H_{adj}. Thirdly, adjust the remaining dataset by H_{adj} to make sure the marked lowest point in the second step is zero. After the aforementioned adjustment, the measured result from fringe projection system has a peak value of 226.7 μm (Figure 2.17). Comparing this with the peak value of 216.8 μm obtained from OLS4000, we can calculate the error is approximately 4.57%. This comparative result shows the developed system is capable of measuring surface height quickly and achieving relative good accuracy.

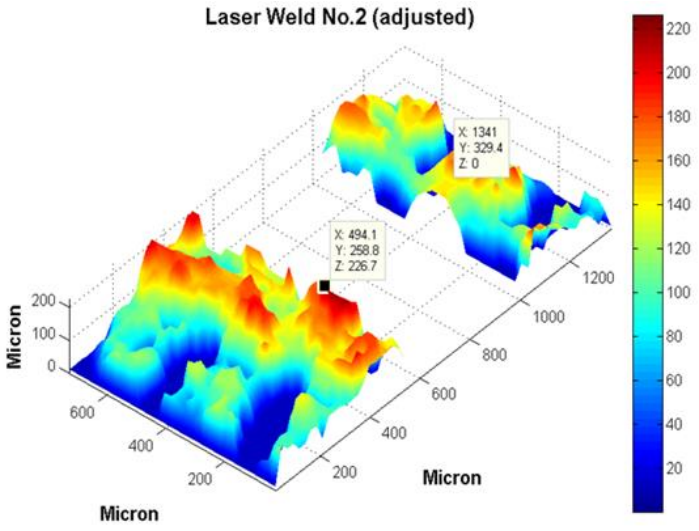

Figure 2.17 Adjusted measurement result of laser weld No. 2 via fringe projection system

2.5.3 Validation test of face-milled aluminum steps

An aluminum block was milled to be used in the validation experiment. The top and bottom surfaces of the aluminum block were milled. The top surface was milled three times to create three steps. Then a finish milling cutter was used to mill the top surfaces again to create better surface finish. Figure 2.18 (a) shows the shape of the block and 2.18 (b) shows the top surfaces of the block. The measurement results of Stage 2 from both systems are described below. The fringe projection system measured an area of 1,620 μm by 1,620 μm on Stage 2. In order to demonstrate the system can achieve good measurement result under high resolution, a different setup is applied in this test (a smaller area is measured under the same FOV). Thus, the measurement resolutions in X, Y, and Z directions are 5.4 μm, 5.4 μm and 0.1μm, respectively. The OLS4000 measured an area of 640 μm by 273 μm with resolutions of 0.625 μm in X and Y directions, and 0.01 μm in Z direction.

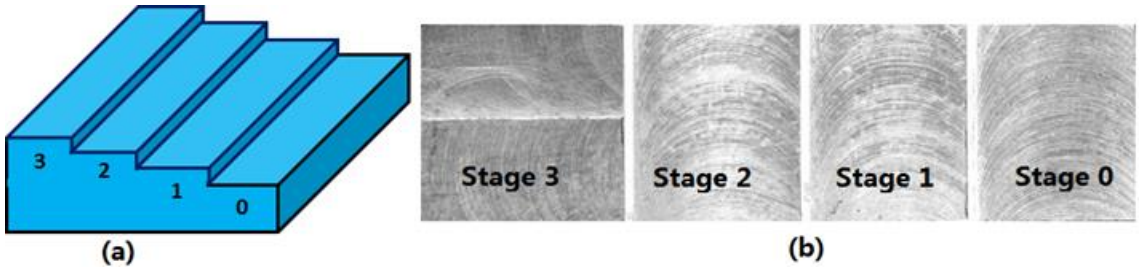

Figure 2.18 Aluminum block used in validation test: (a) side view of the block; (b) top surfaces of the stages after finish milling

Figure 2.19 shows the measured results from both systems. The area that the fringe projection system measured has an overall flatness of 13.6 μm and the area measured by OLS4000 has a flatness of 8.02 μm. To better compare with the result obtained from OLS 4000, zone flatness numbers are calculated on the measurement result from the fringe projection system. Considering the X and Y resolutions are both 5.4 μm, a zone size of 648 μm by 270 μm, which is in the similar size as the measured area by OLS4000 is selected for calculation.

Therefore, we calculated values of 44 zones with 50% overlapping areas between zones illustrated in Figure 2.20.

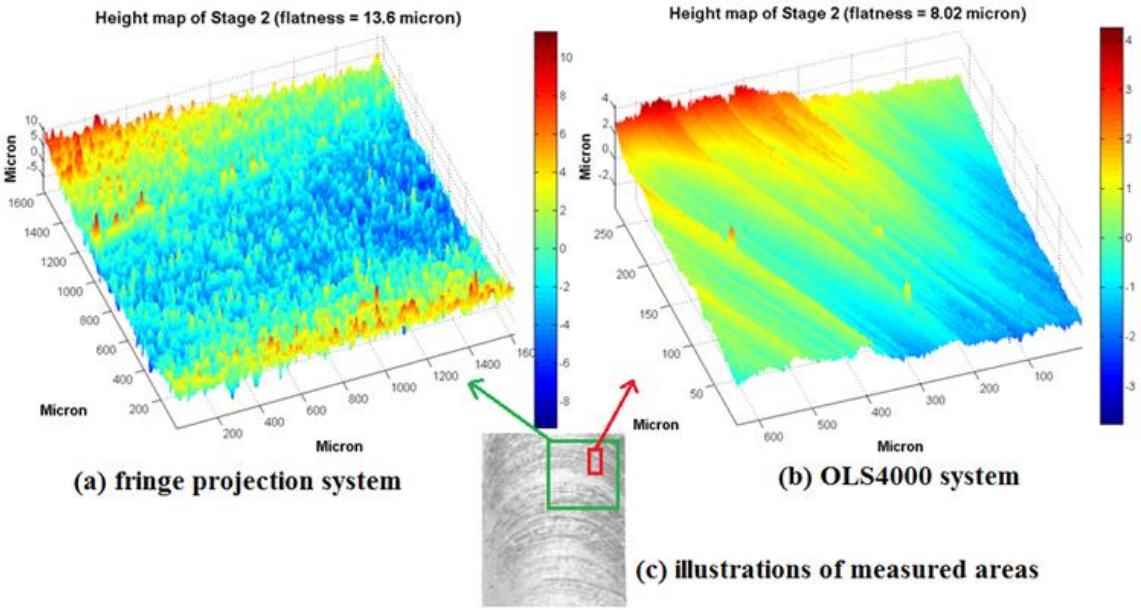

Figure 2.19 Measurement results of stage 2 by two systems: (a) fringe projection system; (b) OLS 4000 system; (c) illustrations of measured areas

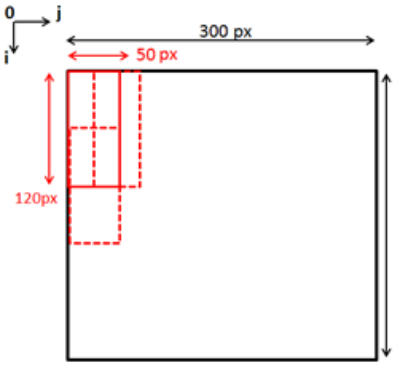

Figure 2.20 Illustration of zone flatness calculation

Calculated values of zone flatness are shown in Table 2-2. The mean value of the 44 zones is 9.8 μm and the standard deviation is 1.5 μm. This result comparable with the flatness measured using OLS4000 (8.02 μm).

Table 2-2 Calculated zone flatness values of measured area using fringe projection system

(i,j) μm	j=1	2.0	3.0	4.0	5.0	6.0	7.0	8.0	9.0	10.0	11.0
i=1	10.3	10.4	10.5	11.1	10.9	10.9	11.8	12.1	11.6	12.2	12.5
2	8.6	8.8	8.2	8.0	7.7	7.7	8.4	8.4	8.5	9.1	9.3
3	11.6	10.6	9.5	8.3	8.6	9.4	8.4	7.8	8.0	8.0	7.7
4	13.3	12.3	11.0	10.5	10.9	10.8	10.0	9.8	10.1	10.2	10.4

2.6 Analysis of sources of errors and compensation techniques

When an object surface is measured using a developed system such as that studied in this research, the result will be subject to an uncertainty due to the design and operation of the system. The total uncertainty will be the sum of many contributing factors. These may be due to uncertainties in measured physical quantities, and imperfection in the theory used to describe the phase shifting interferometry operation. It is important to estimate the uncertainty that could occur in the measurement.

There are two basic classes of error: random and systematic. Random errors can be seen when the measured value of a physical quantity is different under nominally identical conditions. They are caused by unknown and possibly unpredictable changes in the measurement. These changes may occur in any measurement system or due to change in the system or in the environmental conditions. Systematic errors, by contrast, are reproducible inaccuracies that consistently shift the measurement result in one direction or another. These errors are associated with either a flaw in the measurement equipment or in the design of the experiment or due to calibration errors.

These two types of errors have different impacts on the measurement results. Random errors often follow Gaussian normal distributions. The mean of a number of same measurements would be the best estimate or the correct value (in the absence of systematic errors). However,

systematic errors cannot be estimated by repeating the experiments with the same equipment. Successfully detecting both types of errors and obtaining estimates are important for precise measurements.

The rest of this section discusses the identified sources of error and corresponding proposed techniques to monitor and evaluate their effects on measurement.

2.7.1 Phase shift errors

This is an error due to both the nonlinear movement of the PZT and its miscalibration (linearity). Measurements rely on known phase shifts in PSI technique. The recorded intensity by digital camera forms a sinusoidal function of the introduced phase shift. If phase shifter error exists in the measurement system, the actual phase shift φ' can be described as [Brophy, 1990]:

$$\varphi' = (1 + \varepsilon + \varepsilon'\varphi)\varphi \quad \text{.....} \quad (2.14)$$

Where φ is the desired phase shift, ε is the normalized linear phase shifter error, and ε' is the normalized nonlinear phase shifter error. The measured phase φ is achieved by phase shifting technique. Therefore the measured error due to phase shifter can be written as:

$$\Delta\varphi = \varphi' - \varphi \quad \text{.....} \quad (2.15)$$

The calculation of the phase map in the system proposed in this research does not depend on the precise phase step as other algorithms required in the 3-bucket or, 4-bucket techniques, which are affected by the phase shifting errors. For those algorithms, residuals will occur if the phase shift is not kept the same between each two frames. And it is very challenging to keep the phase shift at the exact value. Therefore those algorithms need to adjust the phase shift errors [Hibino et al., 1995; Schmit and Creath, 1995; Langoju et al., 2006; Burke, 2010, 2012]. For the robust least squares phase calculation applied in our system, all the N captured images are used

to obtain the phase $\Delta\varphi$, therefor, the $\Delta\varphi$ will not be affected even there exists a linear error introduced by the phase shifter.

2.7.2 Extra scattering error

Our proposed configuration is a coherent phase measurement system that may give incorrect readings of phase information due to undesired scattering errors (reflected light is added into the object beam that gives readings in phase). Sources that can cause extra scattering errors can include multiple reflections in a fiber giving a secondary wavefront in the system, multiple reflections on the surface of measured object, etc. To estimate the impact of potential scattering errors, we use Figure 2.21 to illustrate this situation.

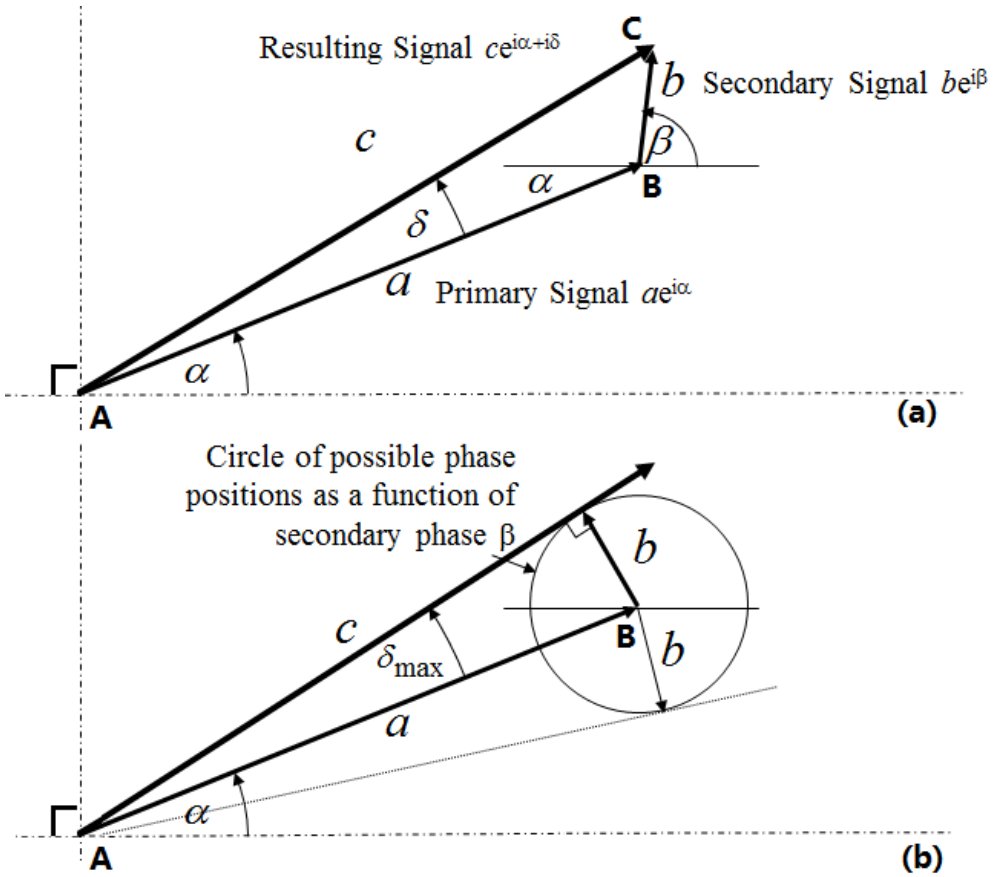

Figure 2.21 Illustration of potential extra scattering error: (a) description of geometry; (b) estimation of maximum phase error

Figure 2.21(a) shows the relationship of the primary signal at point A, the secondary signal at point B, and the resulting signal that will be collected by the detector at point C. α represents the true phase value, β reflects the undesired secondary angle being added into the primary signal and δ is denoted as the phase error. δ can be calculated as follows:

$$\delta = \arcsin\left(\frac{b\sin(\alpha-\beta)}{\sqrt{a^2+b^2+2ab\cos(\alpha-\beta)}}\right)$$

$$for \quad a >> b, \delta \approx \arcsin\left(\frac{b\sin\beta}{a}\right) \qquad \text{.....(2.16)}$$

$$\delta_{max} = \arcsin\left(\frac{b}{a}\right), when \quad c = \sqrt{a^2+b^2}$$

As we do not know where the secondary signal might come, a circle is drawn to show the possible phase position as a function of phase β in the Figure 2.21(b). The δ_{max} can be found when the secondary signal is perpendicular to the primary phase under the assumption that secondary signal has a much smaller magnitude than the primary signal. Figure 2.22 shows the estimated impact on primary signal. It can be seen that a 1% secondary power level with respect of the primary signal can give about a 5 degree (0.087 radian) angular error in the measurement.

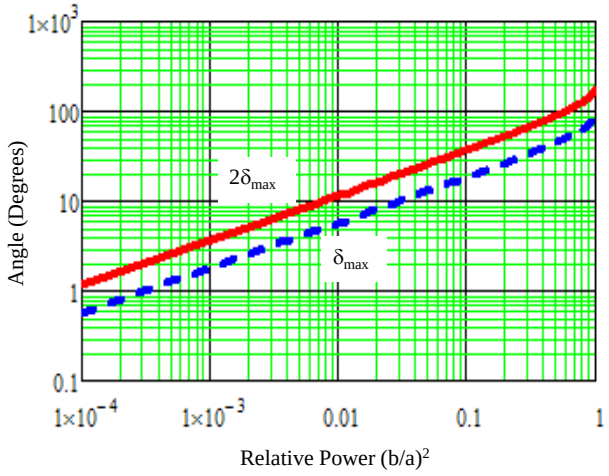

Figure 2.22 Estimated primary signal error caused by extra scattering

2.7.3 Quantization error

Quantization error is induced by truncating an infinitely precise intensity measurement to a nearest-integer representation. This is a random error which is unpredictable. The most effective method to reduce this error is to increase the number of bits used to sample the intensity range.

This error happens in the process of digitization of the output from a digital camera. Digitization is carried out within the camera using 8 bits (0~255) or 12 bits (0~4095) to quantize the output image. [Wingerden, 1991] had derived a result for the error $\delta\varphi$ in calculated phase due to quantization error in the digital camera for a generalized phase-stepping technique where R images were used at N bit quantization with a fringe intensity modulation depth of m. The mathematical expression is written as:

$$\delta\varphi = \frac{1+m}{(\sqrt{3R})2^{N+1/2}m} \quad \text{(2.17)}$$

For the algorithm used in the proposed system, all the R frames have been used, and the measurements are stored as 12-bit images. The error in measured phase is approximately 0.00006 rad. This is equivalent to 0.0000095 fringe or 0.0026 μm for the resolution of 17.27 μm setup shown in Chapter 3 for the gear tooth flank measurement.

$$\delta\varphi = \frac{1+m}{(\sqrt{3R})2^{N+1/2}m} = \frac{1+0.9}{(\sqrt{3\times 12})2^{12+1/2}\times 0.9} = 0.00006 \text{ rad}$$

2.7.4 Vibrations

The sensitivity of measurement systems using phase shifting interferometry is rooted in the fundamental principles of the instrument. Phase shifts may be introduced by a time-dependent phase function, such as the rotation of a mirror attached to a PZT that is controlled by changing voltage, etc. The fact that measurement requires time means that other time dependent

factors, such as vibrations could be involved in the measurement. [Groot, 1995; Rajshekhar and Rastogi, 2012] conducted thorough quantitative analysis of the relative merits of the various phase shifting interferometry algorithms in the presence of vibration. Generally, the vibration noise can be classified into two categories based on the vibration frequency: high frequency vibration and low frequency vibration [Fu, 2010]. If a vibration effect has frequencies higher than sampling frequency of the digital camera, it is regarded as high frequency vibration. Otherwise it is considered as low frequency vibration. According to results found by [Zhang, 2010], low frequency vibrations have larger impacts on the results of phase calculation compared to high frequency vibration. For instance, environmental vibration is normally considered as a low frequency noise. The phase variation caused by environmental vibration can be written as:

$$n(t) = A \cdot \cos(2\pi\nu t + \beta) \quad \text{(2.18)}$$

A is the vibrational amplitude, ν is the vibrational frequency, β is the phase offset. The intensity of the interferogram with consideration of vibration can be written as:

$$I'(t) = a + b \cdot \cos(\Delta\varphi + 2\pi \cdot \phi(t) - n(t)) \quad \text{(2.19)}$$

Two approaches are commonly applied to reduce the influence of vibrations: (1) Prevent vibration through improvement on the hardware. This could be done by optimizing the system configuration to eliminate or isolate factors that could bring vibration errors [Melozzi et al., 1995; He, 2006]; and (2) Identify types of vibration on the developed system and apply specific algorithms which reduce the influence from vibration during the phase calculation process [Wizinowich, 1990; Deck, 2009]. In our system, we took the first approach by implementing three Goodyear air springs under the platform to reduce the influence from potential vibrations.

2.7 Conclusions

A novel measurement system for measuring objects in three dimensions has been proposed. The system uses phase stepping technique to generate shifted fringe patterns. Unlike other systems that use multiple lenses between the laser source and the object for measurement, the developed system only uses a beam splitter. No other optical lens is used between the laser source and object surface. The system has the following advantages compared to existing measurement systems: (1) phase distortions due to lenses are eliminated by using the developed system configuration. The system achieves good measurement accuracy efficiently; (2) the system is significantly simpler compared to other systems that also use phase shifting techniques for measurement. It takes less time to setup the developed system; (3) the developed system has good flexibility to measure various kinds of objects due to its adjustable resolution and projection angles; (4) the cost of the entire measurement system is low ; and (5) the system is simple for installation and maintenance.

CHAPTER 3 ROBUST PHASE UNWRAPPING ALGORITHMS BASED ON FLOOD FILL FOR IMAGE PROCESSING

3.1 The State-of-the-Art phase unwrapping algorithms

Phase unwrapping is the process to ensure that all appropriate multiples of 2π can be recovered from the principal values $(-\pi, +\pi]$ for the points with wrapped phase values [Zebker, 1998]. Assume a true phase value of a point on an object surface is Ψ and the measured or computed value is $\varphi = W(\Psi)$. The wrap function W can be defined as:

$$W(\Psi) = \Psi + 2\pi n \quad \text{(3.1)}$$

Where n is an integer such that $-\pi < \Psi \leq \pi$

In practice the wrapped phase map is first obtained and the next step is to reconstruct the unwrapped phase map to recover the real height image buried in the wrapped phase map. Theoretically phase unwrapping is a straightforward problem. The major process is to reconstruct the physically continuous phase variation by adding or subtracting multiples of 2π. However, it is often a challenging problem because the noise and errors are inevitable and they will degrade the data. The sources of error that could occur in a fringe pattern include:

(1) Electronic noise produced during data acquisition;

(2) Low modulation on data point;

(3) Abrupt phase change due to surface discontinuities;

(4) Violation of the sampling theorem (spatial sampling rate in phase map must be at least twice of the highest frequency of the change of the phase, known as Shannon sampling theorem); and

(5) Geometric distortion in the camera's Field Of View (FOV).

As the widely applied techniques of interferometry, a large amount of interferometric images that correspond to different information need to be phase unwrapped correctly. Various applications have stimulated the development of different methods for phase unwrapping.

Much work has been done on 2D phase unwrapping. Most of the available algorithms can be classified into two major categories: spatial phase unwrapping [Su and Chen, 2004] and temporal phase unwrapping [Zuo et al., 2016]. Spatial phase unwrapping technique retrieves the phase information following a continuous path on the wrapped phase map. With different considerations, a large amount of spatial phase unwrapping algorithms have been developed. In general, all spatial methods can be classified into three groups: (1) simple path-following method [Pritt, 1994; 1997]; (2) Goldstein's method [Goldstein, 1988]; and (3) quality-guided methods [Zhang et al. 2007; Zhao et al., 2010]. Comparing to spatial approaches that use a single wrapped phase map, temporal phase unwrapping algorithms employ a set of wrapped phase maps with at least one of them has no phase ambiguity. Phase information is then retrieved from the relationships among wrapped phase maps. Common methods have been developed and commonly adopted by researchers include: multiple-wavelength algorithm [Cheng and Wyant, 1985; Zhang, 2009] and multiple-frequency algorithm [Huntley, 1993; 1997]. Other available methods include color encoding algorithm [Wang et al., 2010] and N-D phase unwrapping [Jenkinson, 2003].

As we can obtain one wrapped phase map from the current configuration of the developed fringe projection system, we focus on spatial phase unwrapping method in this dissertation primarily.

3.1.1 Least squares methods

Least squares method unwrap a wrapped phase map by discretized partial differential equations (PDEs). The solution leads to a linear equation. Then the algorithm integrates the residues to minimize the gradient differences. This technique usually seeks a phase function whose unwrapped phase gradients are both path-independent and as close as possible to the measured wrapped phase gradients. Parameters such as L_2 are used to evaluate fitting error (for least squares method). The optimization problem has an analytical solution. Unweighted least squares problem can be described as discretized Poisson equation that can be solved by methods such as fast Fourier transforms (FFTs) [Pritt, 1994; Xie, 1998; Arines, 2003], and discrete cosine transforms (DCTs) [Kerr, 1996]. The iterative methods like Picard iteration are required to solve the weighted least squares problems [Pritt, 1997]. Algorithm based on data-dependent weights has also been developed [Liang, 1996], which updates the weights during iterations for the remained wrapped phases using already unwrapped data.

Advantages and limitations: the unweighted least squares method is very fast because of using FFTs, which in turn requires the dimensions of the wrapped phase map to be the powers of two. Moreover, the solution is sensitive to the presence of noises that may cause corruption throughout the result image. This method is generally not suitable in applications with complicated features, especially when features are sharp. Some modification and enhancement to

this method could include adding a reliable guidance map to assist the phase unwrapping. By doing this, the computation efficiency might need to be sacrificed.

3.1.2 Branch-cuts algorithms

These techniques restrict the unwrapping path through the image without discontinuities [Goldstein, 1988]. A basic assumption of this type of algorithm is that phase discontinuities lie on the paths between the positive and the negative residues that are defined as branch cuts. This algorithm is developed to select a path that avoids these discontinuities. The optimal strategies vary among algorithms. Some algorithms will search the phase map only once and select the optimal branch cuts. Some other approaches use a quality map to assist the selection of branch cuts [Huntley, 1989]. Hybrid algorithms combine both the branch cuts and region growing methods have also been proposed with success [Prati, 1990].

Advantages and limitations: the branch-cuts methods visit each pixel on wrapped phase map only once, so images can be processed very fast and demand for computation power is low. It could provide a robust and efficient unwrapping solution for wrapped phase map with low noise and errors in many cases. However, the output might be spatially incomplete in regions with large noise because the optimization is performed locally instead of on the entire input image.

3.1.3 The network flow methods

These methods use the same assumption as branch-cut algorithms [Flynn, 1997; Chen, 2000]. Instead of avoiding the discontinuities, the network flow methods explicitly quantify the discontinuities and then minimize the overall discontinuities in the unwrapped phase map.

Similar to the aforementioned algorithms, guidance map can also be combined in the algorithms to help to reduce the effects of noise and errors.

Advantages and limitations: since a global optimal solution will be used for phase unwrapping in this approach, it can provide robust phase unwrapping in many cases of isolated areas of low noise. By combining this quality map, it can assign a spatially dependent weight per unit flow. However, this approach requires large computation power and processing speed is much lower than other methods.

An algorithm can be evaluated in terms of the computation time, robustness to noise, and sensitivity to propagated errors during unwrapping. The general tradeoffs are between the accuracy of solution and computational requirements. As the complexity of many approaches increases, more efficient computation power is demanded. Improved hardware performance can compensate for some of the increased demands. New challenge occurs on dealing with large volume of data without human intervention.

Phase unwrapping is not a new topic. Apparently, it is a challenge task, especially with more strict requirements on performance from various applications. Nowadays, more and more additional information and adjustment techniques are implemented into the phase unwrapping algorithms. How to successfully incorporate additional information still remains as an open issue and is application-dependent.

3.2 Design of improved phase unwrapping algorithm

The structure of our improved phase unwrapping algorithm is shown in Figure 3.1. There are five steps in the proposed phase unwrapping algorithms. The details of each step will be explained in the following sub-sections.

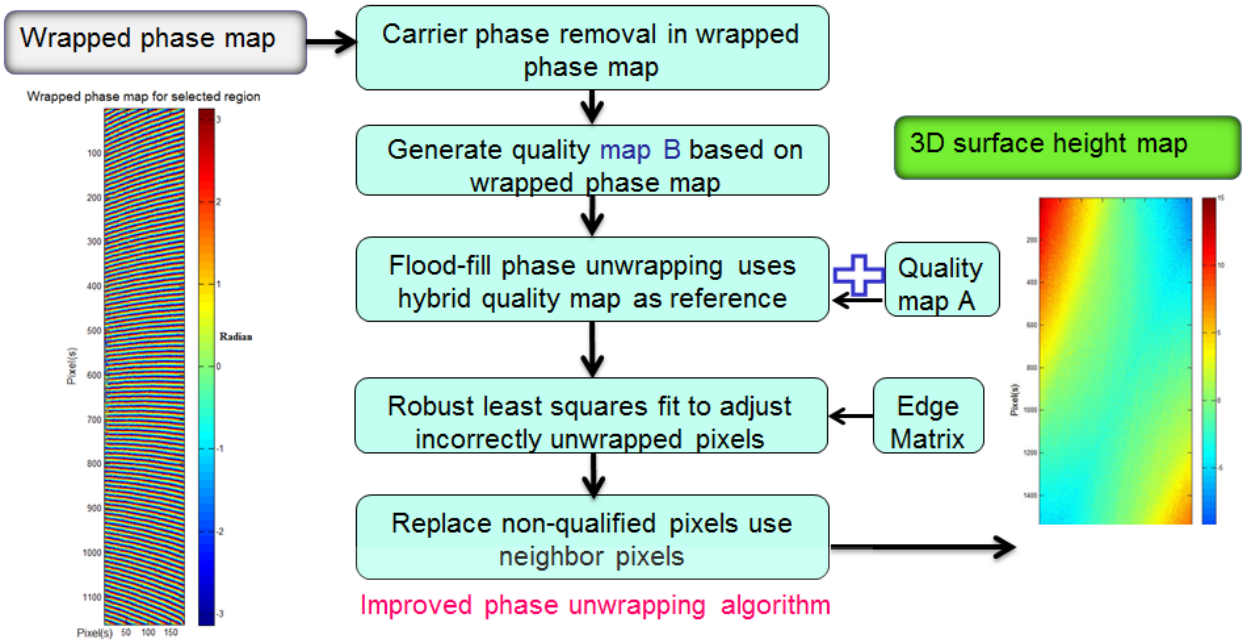

Figure 3.1 Flow chart of improved phase unwrapping algorithm

The processing steps for the proposed phase unwrapping algorithm are:

(1) Remove phase tilt in input wrapped phase map to obtain spatial relative phase measurement map;

(2) Run a quick quality check of the relative phase measurement map and generate a quality map that identifies poles in relative phase measurement map;

(3) Unwrap the spatial relative phase measurement map and set poles as empty pixels that are marked in corresponding quality map;

(4) Apply two one-dimensional robust least square filters to identify and adjust any falsely represented pixels in the image by adding/subtracting 2π; and

(5) Replace the empty pixels using values of neighbor pixels to produce the three-dimensional (3D) height map.

3.2.1 Phase tilt removal

As tilt exists between the two fiber orientations, the original images contain the tilt fringe patterns, which present as an inclined linear surface if it is unwrapped. Phase tilt needs to be removed in order to get the relative height map for the object surface. The phase differences in both X and Y directions are calculated separately for each pixel. The calculation starts from the top left corner of the input image all the way down to the bottom right corner. Mathematical expressions for this operation can be formulated as the following:

$$\Delta\varphi_{x(i,j)} = \frac{\varphi_{(i,j+1)} - \varphi_{(i,j)}}{\Delta j} = \varphi_{(i,j+1)} - \varphi_{(i,j)} \quad (3.2)$$

$$\Delta\varphi_{y(i,j)} = \frac{\varphi_{(i+1,j)} - \varphi_{(i,j)}}{\Delta i} = \varphi_{(i+1,j)} - \varphi_{(i,j)} \quad (3.3)$$

The tilt can be considered as an ideal linear surface $\varphi_{ref}(x,y) = a_0 + a_1 \cdot x + a_2 \cdot y$, so the surface can be separated into two orthogonal directions:

$$\varphi_{ref,x}(x,y) = a_{x0} + a_{x1} \cdot x \quad (3.4)$$

$$\varphi_{ref,y}(x,y) = a_{y0} + a_{y1} \cdot y \quad (3.5)$$

The calculation of $\Delta\varphi_x$ and $\Delta\varphi_y$ can be considered as calculating the slope between two adjacent pixels as Δi and Δj are set to one in Eq. 3.2 and 3.3. After calculating all the $\Delta\varphi_x$ and $\Delta\varphi_y$, automatic adjustments are required as some of the calculation across the boundaries between –π and +π, or 0 and +2π. We apply the following equation to adjust $\Delta\varphi_x$ and $\Delta\varphi_y$:

$$\begin{aligned} &if, \Delta\varphi_* > +\pi, \Delta\varphi_* = \Delta\varphi_* - 2\pi; \\ &if, \Delta\varphi_* < -\pi, \Delta\varphi_* = \Delta\varphi_* + 2\pi \\ &* represents \quad x, y \end{aligned} \quad (3.6)$$

When the adjustment is finished, the average value of all calculations is taken to obtain two mean slope values: $\overline{\Delta\varphi_x}$ and $\overline{\Delta\varphi_y}$. Two linear surfaces of the same size of wrapped phase

map are generated with these two slope values. These two fitted surface are denoted as $\overline{\varphi_{ref,x}(x,y)} = \overline{\Delta\varphi_x} \cdot x$ and $\overline{\varphi_{ref,y}(x,y)} = \overline{\Delta\varphi_y} \cdot y$, respectively. We can obtain the spatial relative wrapped phase map by subtracting the two surfaces from the wrapped phase map.

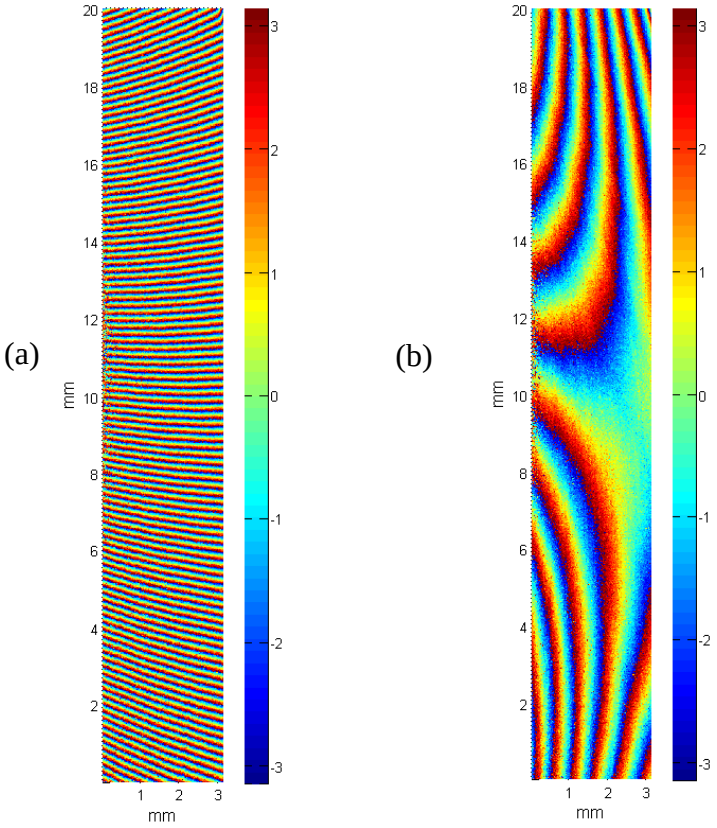

Figure 3.2 Example of phase tilt removal: (a) Wrapped phase map of selected region of interest, (b) Wrapped phase map of same area after removing phase tilt

3.2.2 Quality check to identify poles in wrapped phase map

This step uses the property that as unwrapping is a path independent procedure in a noise-free wrapped phase map, the sum of signed phase wraps around any closed loop should be zero [Dirac, 1931]. Conversely, if different paths between the same pair of pixels give different unwrapped values, there will be loops with a nonzero sum. In this research, the data is sampled in a rectangular lattice. If the signed sum around a given 2-by-2 pixel rectangles is nonzero, then the pixels are denoted as poles [Bone, 1991]. The goal of this step is to detect fake

discontinuities (true discontinuities are the real features on surface, which do have a step change in height) in the wrapped phase map before sending it for phase unwrapping.

The output of this step is a binary map the same as the input wrapped phase map with ones representing detected poles and zeros as pixels with good quality. The procedures developed to detect the poles can be described as follows:

(1) A window of the size 2-by-2 is used to scan the entire input image;

(2) Calculate the phase difference between the four pixels in current window clockwise;

(3) A counter k is set to zero and starts to look at the calculated four phase differences in sequence. k is added by 1 if the difference is less than $-\pi$, or subtracted by 1 if the difference is larger than $+\pi$. k stays unchanged if the absolute difference is less than π;

(4) After going through all the four phase differences, if the final value of k is not equal to zero, all the four pixels will be set as poles. Otherwise, all the pixels are marked as qualified pixels; and

(5) Reset k to zero and repeat the steps from (1) to (4) until all the pixels are checked.

Figure 3.3 explains how the above procedures are operated. And one example is given on how the pole is detected and marked.

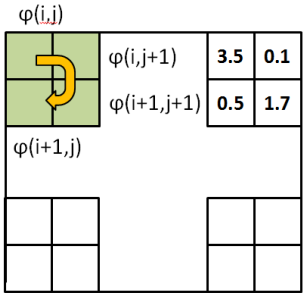

$$\Delta\varphi_{21} = \varphi(i, j+1) - \varphi(i, j) = 0.1 - 3.5 = -3.4 < -\pi;$$
$$\Delta\varphi_{32} = \varphi(i+1, j+1) - \varphi(i, j+1) = 1.7 - 0.1 = 1.6;$$
$$\Delta\varphi_{43} = \varphi(i+1, j) - \varphi(i+1, j+1) = 0.5 - 1.7 = -1.2;$$
$$\Delta\varphi_{14} = \varphi(i, j) - \varphi(i+1, j) = 3.5 - 0.5 = 3.0.$$

Figure 3.3 Illustration of detection of poles in wrapped phase map

We have one phase difference less than –π, which changes k to -1. All the other phase differences will not change the sign of k. Therefore, the final value for k is -1, which will trigger the alarm for pole detection. The same positions of the four pixels on the binary guidance map will be marked as one.

The judging condition includes two parameters: +/-π for the phase difference evaluation and the counter k. Since all the wrapped phase values are restricted in a 2π range, when any two adjacent pixels have more than π in phase difference, it is considered remarkably large. Typically, most of these adjacent pixels with large phase jumps have false phase information. These errors are usually caused by noise during image acquisition or incorrect calculation of phase values. The counter k is developed to make sure the true discontinuities are retained. For surfaces with real discontinuities, in a selected 2x2 window, it looks like a vertical, horizontal or diagonal line (Figure 3.4). The example of Diagonal 2 in the figure below is evolved from the first three conditions. It is easy to find that none of the real discontinuities is identified as poles based the developed algorithms shown below.

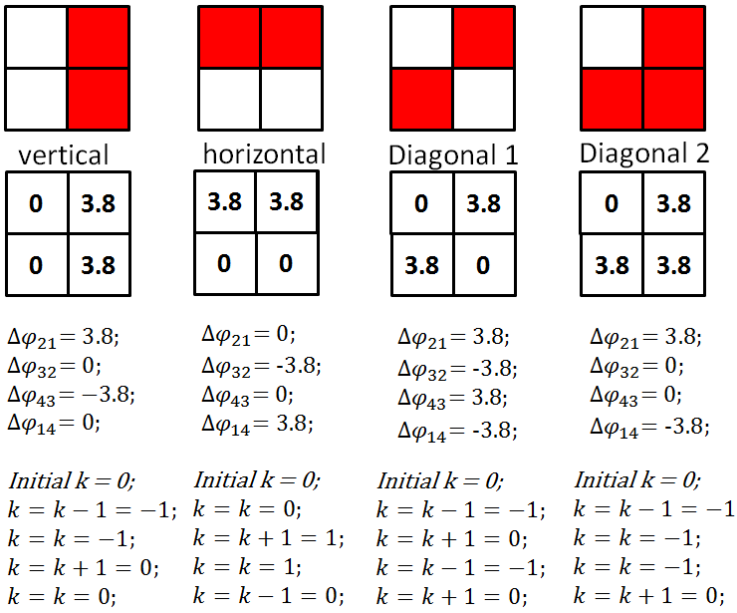

Figure 3.4 Criteria for pole detection not violating the real discontinuities

3.2.3 Flood fill phase unwrapping

The flood fill algorithm has been developed and used for a long time in phase unwrapping [Asundi, 1998]. The basic concept of this algorithm can be described in Figure 3.5. The algorithm always checks the generated guidance map from section 3.2.2 before doing phase unwrapping on any of the pixels. The procedures can be described as below:

(1) Given the location of start pixel (x, y), the phase value is unwrapped;

(2) Look at the pole map generated from last step for the nearest four neighbors of the unwrapped pixel. Skip the pixel if it is identified as pole, otherwise unwrap it based on the phase difference compared to the starting pixel;

(3) Check the surrounding pixels for the unwrapped pixels at the boundaries of the flood filled area. Repeat step 2) until all the pixels are unwrapped; and

(4) Replace the values in locations of poles with 'Not-a-Number' (NaN) to distinguish them from unwrapped phase map.

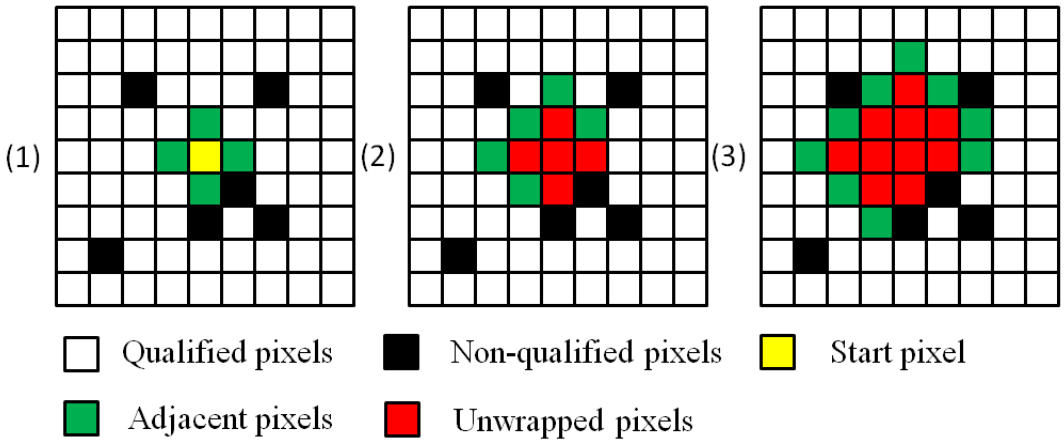

Figure 3.5 Illustrations for flood fill algorithm

3.2.4 Adjustment of incorrectly unwrapped pixels based on robust least squares fit

After unwrapping the phase map, robust least squares fit is used to adjust any remaining incorrect pixels. Since the major operation of phase unwrapping is adding/subtracting single or multiple 2π(s) to recover the pixel to the real phase value, it is possible that incorrect numbers of 2π(s) are applied. Therefore it is necessary to adjust the incorrect phase unwrapping pixels to avoid unwanted errors. One dimensional robust least squares fitting based on bisquare weights are applied in both the X and Y directions for the unwrapped image. The reason why selecting the bisquare weights is because it simultaneously searches for a curve that fits the input data using the usual least squares approach, and minimizes the effect of outliers by updating the weights in each iteration. The residuals will be examined after each iteration, any residual larger than 2π will be taken back by adding/subtracting 2π(s) until the difference of the residual value of that pixel and its adjacent pixel is less than 2π (Figure 3.6).

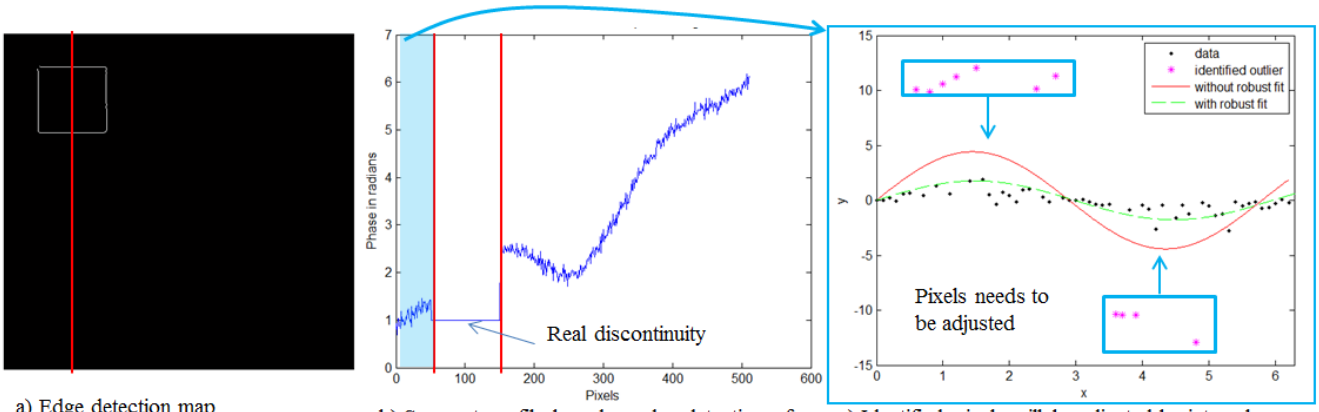

a) Edge detection map

b) Segment profile based on edge detection of original image

c) Identified pixels will be adjusted by integral multiple of 2π without affecting the real discontinuity

Figure 3.6 Illustration of adjusting outliers using robust least squares fit

It is straightforward to apply this technique on measurements of flat surface or surface with curvatures. However, it cannot be used directly on surfaces with complicated features like real discontinuities which may have more than 2π height differences. A proposed method is to take a measurement of the surface under normal light condition. Then apply edge detection algorithm to extract the edges and save that for adjusting outliers after phase unwrapping.

3.2.5 Replacement of non-qualified pixels using neighbor pixels and scale conversion

This step will process those detected non-qualified pixels (poles and other faulty pixels) that have been avoided during the phase unwrapping procedure in section 3.2.4. These non-qualified pixels will be replaced using median values of its nearest eight pixels. If a block of poles are detected, the pixels on the boundaries will be adjusted at first. Then, the interpolation goes inside to replace all the poles.

After the above procedures, the 3D surface map has been recovered. However, the values in X and Y orientations are shown in number of pixels, and the Z axis, which represents the surface height, is shown in radian. It is appropriate to show the result in micron or millimeters

instead of radian for easy understanding. The scale for the conversion can be calculated based on the geometrical setup of the system for a given measurement.

3.2.6 Comparison to existing phase unwrapping algorithms

A continuous phase map is generated by a computer to evaluate the performance of proposed phase unwrapping algorithms comparing with other existing methods. The size of test image is 512-by-512. Figure 3.7 (a) and (c) show the created continuous phase map and wrapped phase map under ideal condition. Figure 3.7 (b) shows the same image as (a) with the addition of a normally distributed noise that has a variance of 0.5 radian. Figure 3.7 (d) shows the corresponding wrapped phase map of (c).

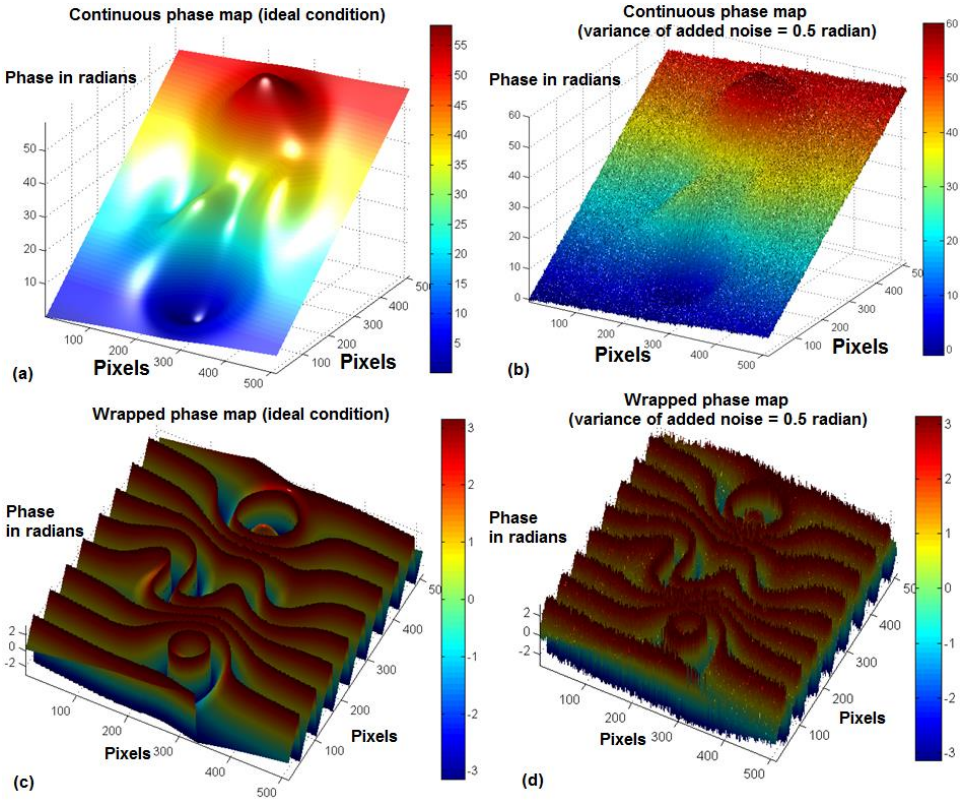

Figure 3.7 Created ideal and noisy continuous phase maps and associated wrapped phase maps

Two existing algorithms, a simple-path following method and conventional flood fill algorithm, are selected to compare with the proposed method. Figure 3.8 shows the result comparison among these three algorithms. Result obtained by simple-path following method shows a clear error stripe, this propagated error represents a classic type of error usually occurs in spatial phase unwrapping algorithm. Result from conventional flood fill method is better, only several spikes are observed. The proposed algorithm delivered very smooth result with no obvious error is observed. The processing times of simple-path following method, flood fill method and proposed method are 0.366 seconds, 1.999 seconds, and 2.193 seconds, respectively. For this image with size of 512 pixel-by-512 pixel, we have 262,144 pixels in total. Counting the occurrences of incorrectly unwrapped pixels, we have 195 for simple path following method, 42 for flood fill method, and 8 for the proposed method.

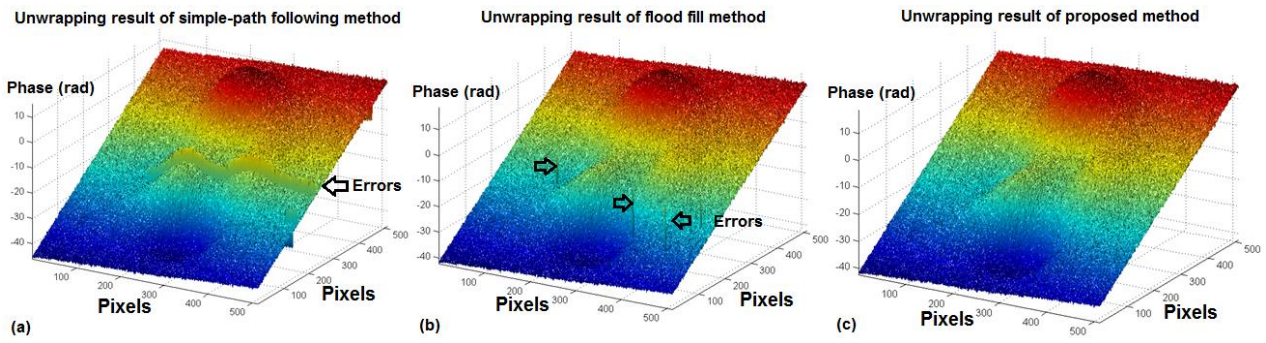

Figure 3.8 Comparison results of different unwrapping methods with noise variance = 0.5

We doubled the variance of added noise to 1.0 radian with all other factors unchanged. Figure 3.9 shows the unwrapping results of three elevated algorithms in 2D and 3D views. The result from simple-path following method contains a large amount of errors. Many errors are propagated. Floor fill method recovered most of the phase information. However, many noisy pixels are unwrapped incorrectly and cause spikes on the final result. Proposed method performed robustly in the presence of big noise. 279 out of 262,144 pixels are incorrectly unwrapped using the proposed method, comparing 55,973 incorrectly unwrapped pixels with

flood fill method. There are over 200, 000 pixels incorrectly unwrapped with the simple-path following method, which means the result can be hardly used. The processing time for these three methods are 0.471 seconds (simple-path following), 2.606 seconds (flood fill), and 3.834 seconds (proposed).

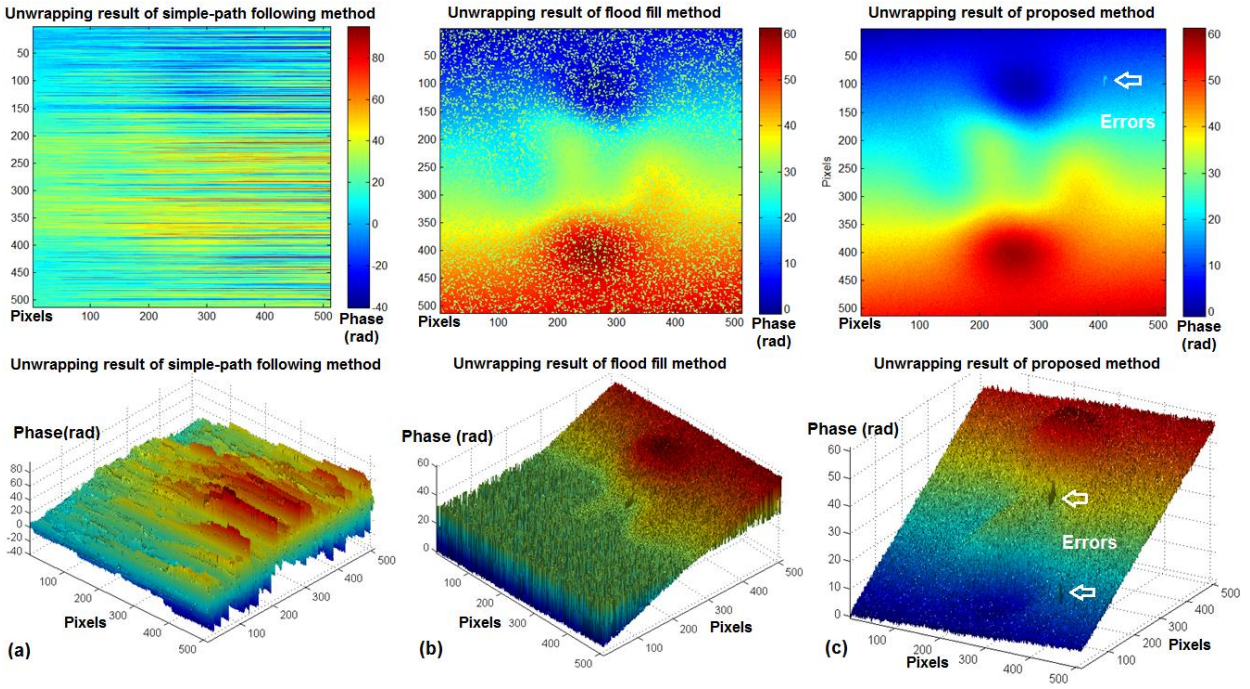

Figure 3.9 Comparison results of different unwrapping methods with noise variance = 1.0

3.3 Case studies

3.3.1 Measurement of gear tooth flank

Various types of gears are used widely in mechanical devices such as transmission in automotive vehicles. Their quality is critical to the performance of the whole system. Gears with bad qualities may result in problems such as loss of power, vibration and severe noise. Serious problems may cause malfunction of the system or even damages to the system. It is a challenging task to measure the gear tooth flank precisely due to its complicated geometrical shape. With the

proposed system, we are able to measure the area of the tooth flank quickly and accurately. Two examples are given below to show the feasibility of the proposed system.

3.3.1.1 Measurement of the tooth flank of a helix gear

The general shape of the tooth flank of a helix gear is of interest. To conduct measurement on this gear tooth, it is held on a steady adapter. Fringe patterns are projected directly on the target tooth flank, and a digital camera continuously takes a series of images for processing. Figures 3.10 (a) and (b) show the image of a whole gear and the tooth for measurement.

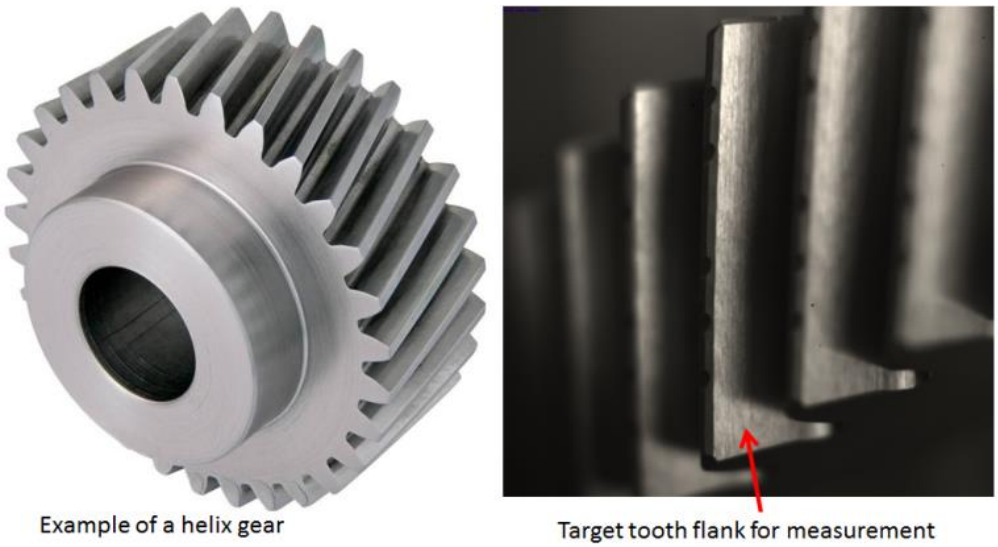

(a) (b)

Figure 3.10 Helix gear tooth flank: (a) example of a helix gear, (b) target tooth for measurement

When the data acquisition is completed, the algorithm will follow the steps we have described above to obtain the result. The average pixel size is 15 μm/pixel in X and Y directions. The selected area for process represents 4 mm-by-24 mm on the tooth flank.

Figure 3.11 (a) shows one frame of the helix gear under measurement, the fringe patterns can be seen clearly on the gear flank. Figure 3.11 (b) shows the calculated wrapped phased based on all the phase-shifted images within the target area. Following the algorithm of phase unwrapping, the unwrapped image can be obtained. To get the general shape profile of the tooth flank, a low pass filter with cutoff wavelength at 0.6 mm is added to obtain the final result in Figure 3.11 (c) and all the scales have been converted into millimeter or micron. A profile line is selected to show the general shape of the gear flank in Figure 3.11 (d). It shows clearly the general shape of the measured area on the tooth flank, which can be used for quality investigation on the height variation.

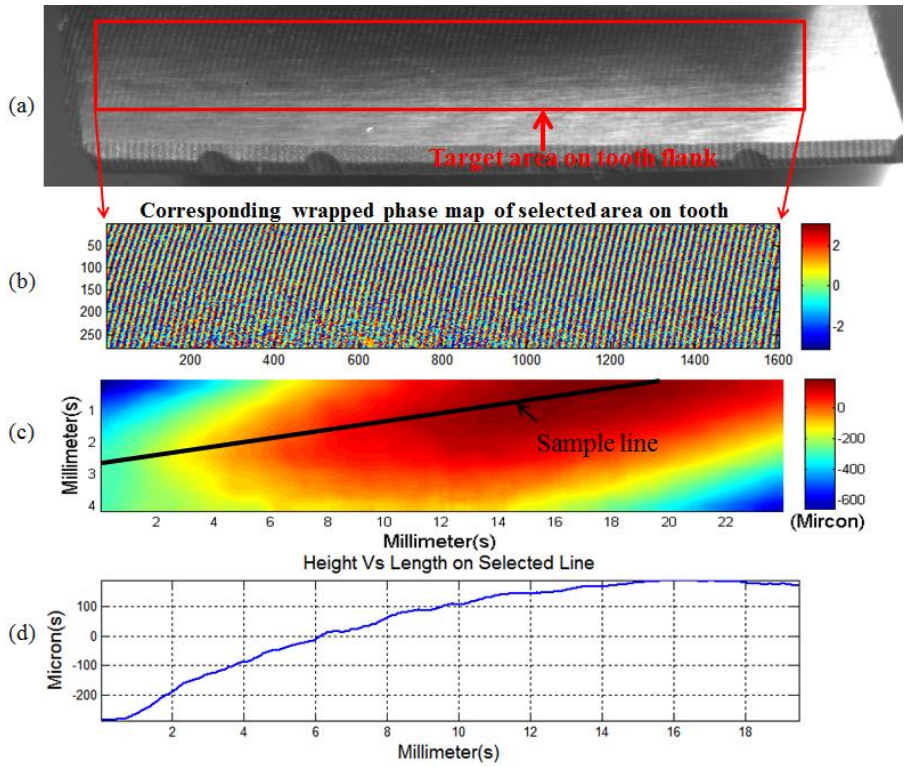

Figure 3.11 Measurement result of tooth flank of a helix gear

3.3.1.2 Evaluation of surface waviness of the tooth flank of a pinion gear

This example will show how the waviness on a pinion gear flank surface is extracted from measurement taken by the developed fringe projection system. We received several pinion

gears of the same type from an automotive manufacturer to measure the surface waviness on the tooth flank. The setup is similar to what we have done in the measurement of a helix gear.

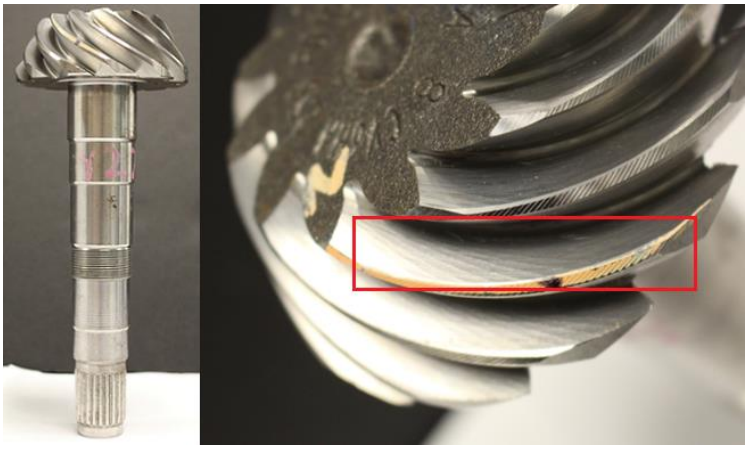

Figure 3.12 Illustration of a pinion gear and targeted measurement area

A pinion gear is shown in Figure 3.12, the tooth flank is of interest to measure. A mounting platform is used to clamp and hold the gear for measurement. Phase stepping is added on the dual laser beams between frames (Ch. 2.2). Fringe patterns are projected directly on the targeted tooth flank surface. The camera records 12 consecutive images and stored them on the computer. The robust phase calculation algorithm starts to calculate the phase information for each pixel and generate the phase map of measured area. Figure 3.13 shows a sample result of measuring one flank surface on a pinion gear. The image on the left shows how the gear looks like under normal illumination. One of the 12 frames is used to illustrate a typical fringe pattern. The wrapped phase map is shown on the next to the figure with fringe patterns. Finally a selected area is magnified for better illustration.

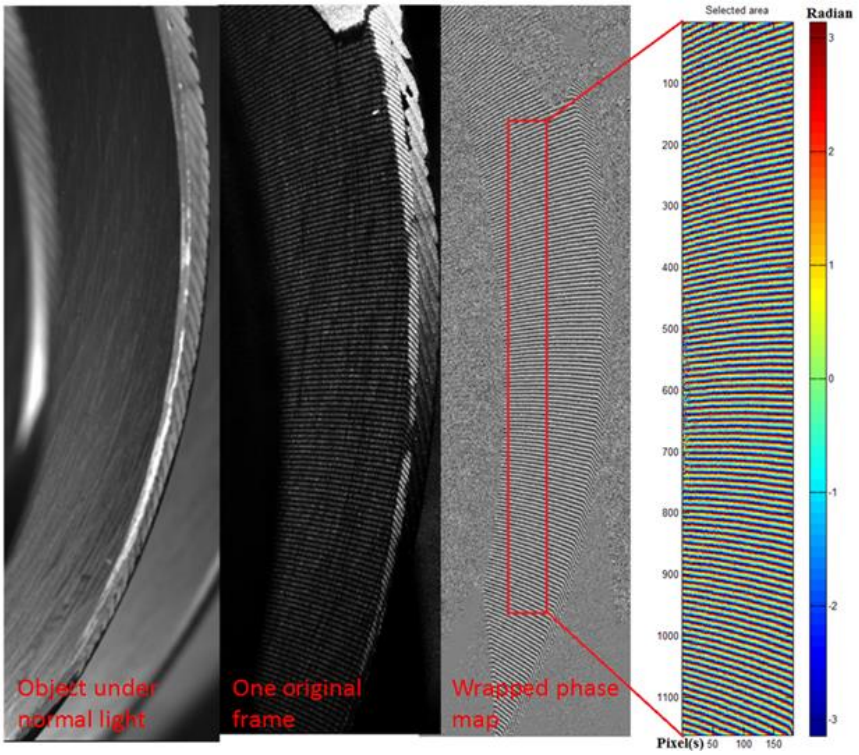

Figure 3.13 Illustration of measurement of tooth flank of a pinion gear, from left to right: (a) object surface under normal light, (b) one frame with fringe pattern, (c) calculated phase map and (d) zoom-in figure of selected area

Then the phase tilt of the phase map will be removed and the remaining phase map is denoted as wrapped spatial relative phase map. After this process, the phase unwrapping algorithm described above will be applied to produce the surface 3D ("height") map.

The input image size is about 1160 pixels by 180 pixels, which represents an area of 20.03 mm by 3.11 mm (average pixel size is 17.27 μm /pixel).

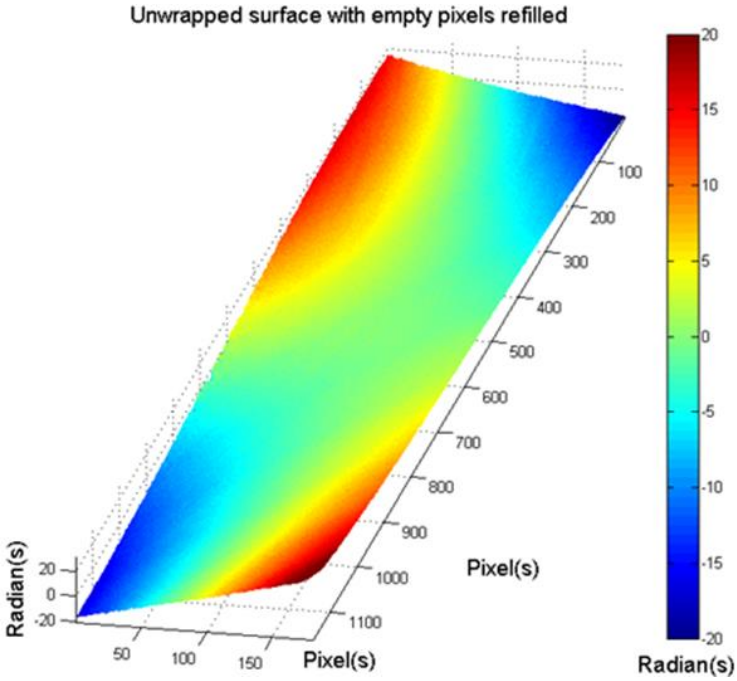

Figure 3.14 Unwrapped phase map of tooth flank of pinion gear

As the Z values in above unwrapped phase map are shown in radians, which is not easy to understand. We have the following parameters to calculate the scale for converting radian to micron based on the current system configuration. Figure 3.15 illustrates how the vertical fringe spacing is calculated. Top left is the light source that fringe patterns will be generated. The vertical fringe spacing is dependent only on the horizontal fringe spacing L in a radial direction relative to a vertical axis that passes through projector fiber. L is measured in the direction of r . The vertical fringe spacing at any point H is equal to the horizontal fringe spacing at that point times the tangent of ε ($\tan\varepsilon = z / r$).The resolution in this example is 17.27 μm/pixel, and the projection angle is 20 degrees. The fringe spacing between two adjacent horizontal fringe patterns contains approximately 15.5 pixels. Therefore, for every 2π phase change in horizontal direction it represents L = 17.27 x 15.5 = 270.8 μm. Convert this value into height H , which equals to 98.56 μm. Divide H by 2π, the scale equals to 15.68 μm /pixel.

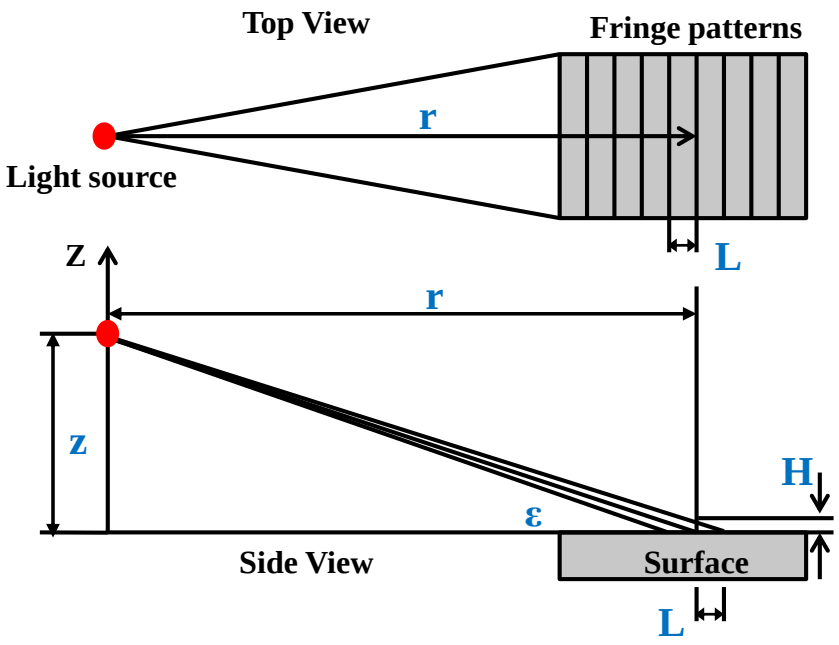

Figure 3.15 Illustration of scale conversion

The waviness of the gear flank is of interest in this application. Two 2D low-pass filters at different cut-off wavelengths ($\omega_1 < \omega_2$, ω_1 = 0.8 mm and ω_2 = 2.5 mm in current application for waviness extraction) are applied on the surface height map separately. The corresponding filtered surface height maps are denoted as FS_1 and FS_2 (Filtered Surface). By subtracting FS_2 from FS_1, only the waviness data will be retained. Then surface waviness measurement can be conducted on the retained surface depending on the operator's request.

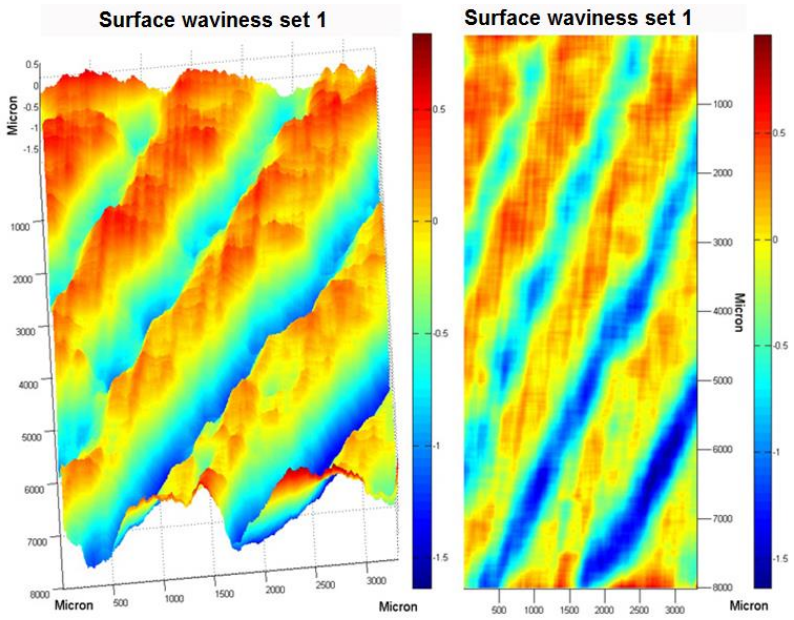

Figure 3.16 Surface waviness for pinion gear tooth flank (perspective and top view)

Compared to conventional profilometers that can only measure a trace on the object surface, we now have an entire area measured that can be used to evaluate the quality of the gear tooth flank (Figure. 3.16). Currently, we extract traces that are perpendicular to the waveforms on the waviness height map. And then calculate the total waviness W_t values [ASME B46.1, 2009] for the selected traces. The final W_t is calculated based on all the calculated W_t values to represent the evaluation result of the measured area on gear tooth flank. The overall W_t for this measured gear is 2.18 μm. Examples are shown in Figure 3.17 to illustrate the calculation of W_t .

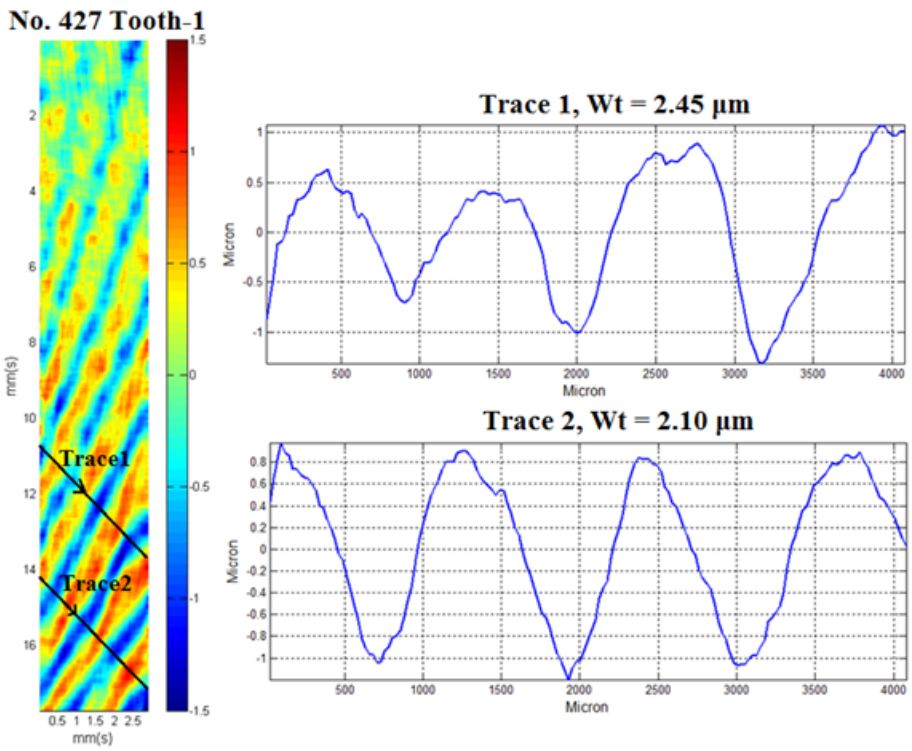

Figure 3.17 Waviness map of gear No. 427 tooth 1 after phase unwrapping and filtering

3.4 Repeatability test

3.4.1 Evaluation of repeatability

To evaluate the repeatability of the proposed measurement system, several sets of tests are designed. The configuration has a basic X and Y resolution (average) of 17.27 µm/pixel, and the projection angle of the sensor is at 20 degrees. The selected region of interest on the tooth flank is approximately 18.3 mm by 2.9 mm.

Before experiments, the system was warmed up for approximately 30 minutes. Group 1 test consists of 100 measured data sets and 12 continuous frames in each data set. All tests were collected in approximately 55 minutes. Then the system was left with power on for about 1.5 hours. Group 2 test collects another 100 data sets over another period of 55 minutes. During the entire experiments, no adjustment was made and the measured part stayed untouched.

The parameters used in the repeatability test are defined below (Figure 3.18): Evaluation Length L **:** a two dimensional profile that corresponds to the length of the slice, it is defined as 1.2 mm in the repeatability test in the measurement of gear tooth flank.

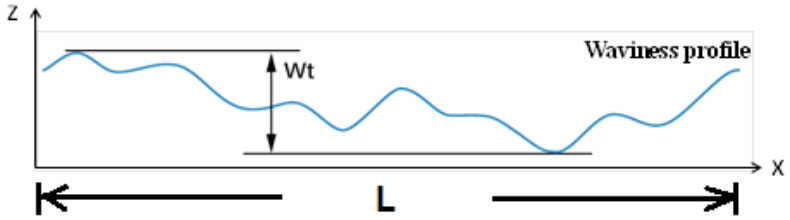

Figure 3.18 Definition of the waviness parameter used in calculation

W_q : the root-mean-square (rms) waviness of all points on the profile in one evaluation length

$$W_q = \sqrt{\frac{1}{L}\int_0^L [z(x)]^2 dx} \quad \text{..... (3.7)}$$

W_t : the peak-to-valley value on the profile in one evaluation length

$$W_t = \max(z) - \min(z) \quad \text{.....(3.8)}$$

3.4.2 Repeatability test to check system drift

This test will process the data in the direction that is perpendicular to the propagation direction of the reconstructed surface waviness. The goal is to eliminate the variable-directionality of the hundreds of traces can be produced from measurement result in section 3.3.1.2. The procedures can be described as follows:

(1) Pick 80 traces on the result image at a vertical spacing of 8 pixels (Figure 3.19). The perpendicular distance from one trace to the other trace is $\frac{8*17.27}{\sqrt{2}} = 97.69$ μm

(2) Divide each trace into three segments at equal length

(3) Calculate W_t for each segment and select the biggest of three to represent that trace

(4) Do all the calculations for the selected 80 traces

(5) Rank the 80 selected local maximum W_t values in descending order

(6) Pick the 90th percentile highest value to represent this data set

(7) Repeat steps (1)-(6) for all the 100 data sets in each group and get 100 W_t values

(8) Calculate the Mean and Stand Deviation (STD) of the 100 W_t values from step 7.

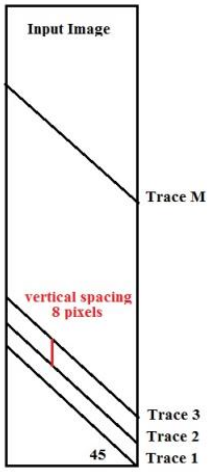

Figure 3.19 Illustration of trace extraction on waviness surface

Table 3-1 Result for repeatability test on system drift

Area Waviness Metric	Group 1 (1-100)	Group 2 (101-200)
Wt Mean	2.16 μm	2.19 μm
Wt Std	0.022 μm	0.023 μm
Wq Mean	0.418 μm	0.424 μm
Wq Std	0.0021 μm	0.0023 μm

In Table 3-1, the calculated mean W_t values for the two groups are close and the standard deviation of the W_t is very small. This demonstrates good repeatability performance of the current system. The system is stable without showing any significant drift.

3.5 Validation test for pinion gear measurement

Due to the curved shape of pinion gear flank surface, it is impossible to use OLS 4000 system to conduct measurement. Contact probing system is a traditional method adopted by manufacturer to complete the measurement. Figure 3.20 illustrates how a gear flank is measured using a Jenoptik system.

Figure 3.20 Measuring a pinion gear on Jenoptik probing system

Obtained raw measurement data from the Jenoptik is called primary profile. Additional data filtering procedures need to be applied in order to get the waviness profile. Table 3-2 lists details of the evaluation conditions. The time needed to complete one measurement profile is 9.6 seconds. Waviness metric W_t will be calculated after measurement.

Table 3-2Evaluation conditions for the measurement of pinion gear flank

λc:	0.80 mm	Measuring points:	9600
λf:	1.20 mm	Traverse length:	4.80 mm
Remove form:	ON	Distance between points:	0.5 μm
Alignment:	ON	Speed:	0.50 mm/s
Filter ISO 4287:	ISO 16610-22	Stylus tip radius:	0.005 mm

One flank tooth on each one of the two pinion gears (No. 427 and No. 587) are measured by both systems. We will use gear No. 427 as an example to show the result comparison. Figure

3.21 is a scanned explosion of the measurement result of gear No. 427 tooth-1. The measured profile has a W_t value of 2.5 μm.

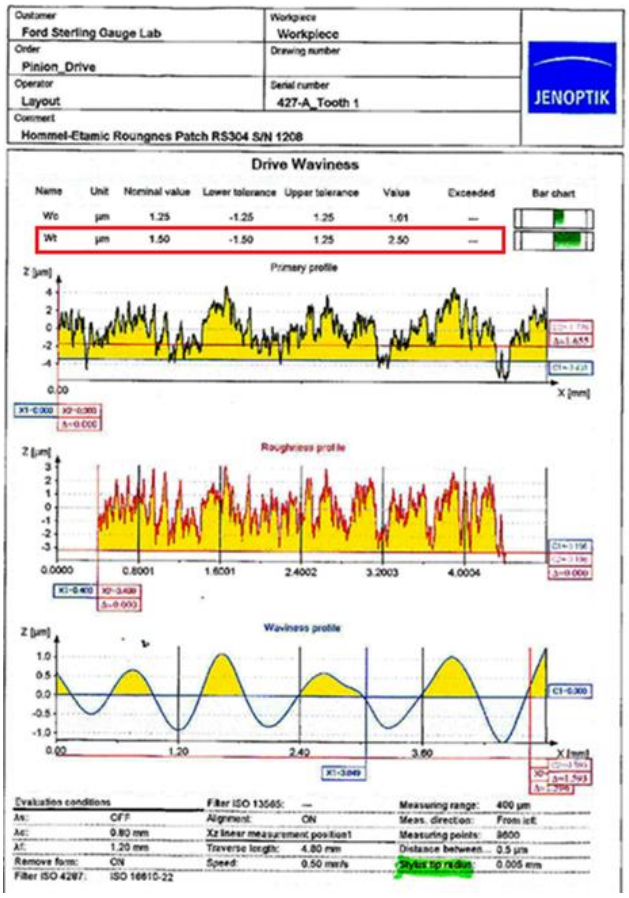

Figure 3.21 Measurement result of gear No. 427 tooth 1 by Jenoptik

Figure 3.17 shows the filtered result of the waviness surface of gear No. 427 tooth 1. Two traces are selected to illustrate the values of W_t. Trace 1 and trace 2 have W_t values of 2.45 μm and 2.10 μm, respectively. Although we cannot find the exact location of the line profile measured by the Jenoptik probing system, we do know it is extracted from the surface measured by the fringe projection system. So we randomly select 80 traces across the measured area with 100 μm spacing between each two traces and calculate the W_t. Then we calculate the mean and standard deviation of all the 80 W_t s and compare it with the result obtained from Jenoptik. We

believe this is an appropriate method to check if the measured results from two systems are comparable or not. Table 3-3 listed the results for comparisons. For gear No. 427 tooth 1, the mean value of 80 traces is 2.20 μm (standard deviation is 0.036 μm) in comparison with the single profile measured by Jenoptik which has a W_t value of 2.50 μm. Following the same steps described above, we obtain the mean value of 2.82 μm (standard deviation of 0.034 μm) for the gear No. 587 tooth 1. In comparison, the single line profile measured by Jenoptik gives a W_t value of 2.60 μm.

Table 3-3 Calculated results from Jenoptik and fringe projection system

Pinion Gear	Method	Wt	Wt Mean	Wt Std
No. 427 tooth 1	Jenoptik	2.50 μm		
	Fringe projection		2.20 μm	0.036 μm
No. 587 tooth 1	Jenoptik	2.60 μm		
	Fringe projection		2.82 μm	0.034 μm

3.6 Conclusions

A phase unwrapping algorithm with improved performance to noise and discontinuities is developed based on flood fill technique. The algorithm is robust in processing wrapped phase map of various measurements in comparison with existing phase unwrapping algorithms such as simple-path following method and conventional flood fill method. The proposed algorithm can retrieve phase information at high success rate even under high noise condition.

Real case studies are conducted on the measurement of helix gear and pinion gear. A validation test is performed to demonstrate that the developed fringe system and proposed phase unwrapping algorithm can measure pinion gear accurately.

CHAPTER 4 MULTI-SCALE SURFACE CHARACTERIZATION AND CONTROL BASED ON HIGH DEFINITION MEASUREMENTS[3]

4.1 Introduction

4.1.1 Motivation

In Chapter 1, some limitations of current GD&T specification for the characterization of surface shape have been introduced. New metrics can be developed to accurately characterize surface shape by using advanced metrology system. Another comparison is given here to emphasize the advantages of using advanced metrology system that can provide high definition measurement. Current industry practice obtains the measurement of a machined surface via a combination of several metrology systems with different accuracy and resolutions such as a coordinate measuring machine (CMM) to measure the shape and a profilometer to measure local areas. Traces in Figure 4.1a are usually measured to represent the entire marked area for the evaluation of surface parameters such as flatness.

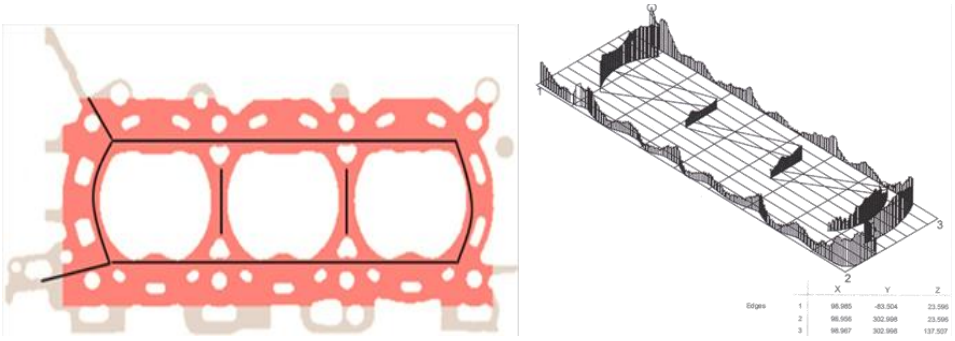

(a) (b)

Figure 4.1 Measurement of an engine head using CMM: (a) traces to be measured using CMM, (b) Measurements result

[3] This chapter is based in part on [Weng, 2014].

On the other hand, selected small patches (Figure 4.2a) are measured for the evaluation of the surface quality in fine scale using equipment such as areal profilometer. Different techniques on different platforms have to be utilized in order to measure a machined surface. This is a time consuming process and various errors may occur during different measurement setups. Moreover, since estimations are made on this limited information of the surface, abnormal patterns may be overlooked due to the large unmeasured areas.

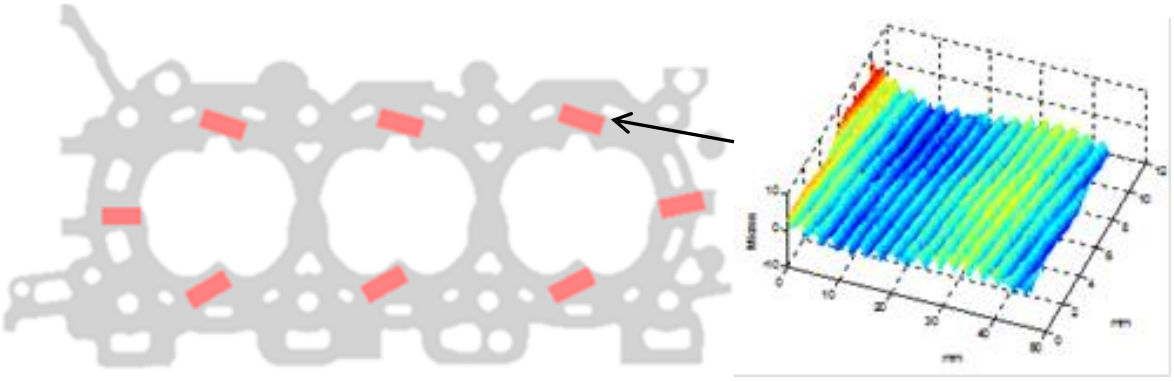

(a) (b)

Figure 4.2 Measurement of an engine head using profilometer: (a) patches to be measured, (b) measurement result of a selected patch

With the advances in new surface metrology system, engineers have the capability to obtain sub-micron level surface height information at fine lateral resolution over a relative large field of view (FOV). For example, Coherix can offer a ShaPix product that has lateral resolution of 150 μm for FOV up to 300x300 mm^2 or 80 μm for FOV up to 80x80 mm^2 based on different configurations[4]. Both systems can provide micron level vertical resolution. Obtained abundant information can be analyzed to further the understanding of the machining process. Figure 4.3 shows a measurement of the deck face of a machined engine head using digital holographic interferometry. The 3D height map provides a complete view of the entire surface such that both

[4] http://coherix.com/solutions/shapix3d-planar-flatness/

general shape and local variations can be seen clearly. Thus, the potential assembly performance can be evaluated, such as a possible leakage path between the deck face and engine block. Moreover, the tooling patterns observed on the deck face reflect the machining conditions that can be potentially utilized for process monitoring. Therefore, high definition surface measurements present new opportunities to understand the mechanism of surface generation in large and medium scales (e.g., flatness and waviness).

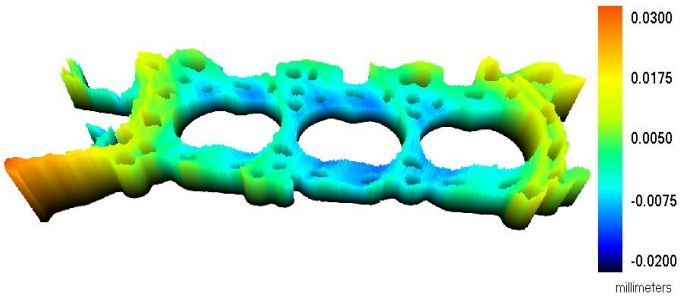

Figure 4.3 Measurement of a deck face of an engine using digital holographic interferometry

This research proposes a framework for the utilization of high definition measurements. A two-step data analysis methodology is presented. The first step focuses on extracting the generalized surface shape while the second step focuses on the development of tools for specific engineering applications. The combination of these two steps can help engineers to effectively evaluate the quality of machined surfaces and obtain valuable information for process condition monitoring and control.

4.1.2 The State-of –the-Art surface shape characterization

This section provides a review of current techniques and specifications in the characterization of surface shape (for surface wavelength > 0.15 mm, as our focus scope is in form scale shape characterization).

4.1.2.1 Mathematical characterization of surface shape

Research has been extensively conducted on mathematical representation and characterization of three-dimensional shape. Eshleman and Meriwether [1966, 1967] expanded the understanding and usefulness of cubic and bicubic Hermitian forms of curves and surfaces. A key point they made was the use and evolution of geometrical model through the whole manufacturing process. Generality and variability of a model's mathematical representation had been emphasized. In the 1970s new ideas emerged, including piecewise curves, surfaces, and the joining together of multiple separated curve segments or surface patches to form more complex shapes. A very thorough survey of the methods developed before 1985 can be found in [Besl and Jain, 1985]. Methodology [Schwartz and Sharir, 1987] was developed to solve the free-form space curve matching problem without feature extraction in the late 1980s. Implicit algebraic non-planar three-dimensional curve and surface estimation was introduced by Taubin [1988].

Since 1990s, research has been conducted on expanding parameters from 2D to 3D surface texture and topography. Stout [1993] defined the so-called Birmingham 14 parameters for assessment of surface finish in 3D. It covered a broad range of topics on 3D micro-topography. Whitehouse [1994, 2004] also thoroughly summarized research related to surface metrology. At the same time, advanced optical systems have been developed for small measuring surfaces in 3D. Chen [2000] provided a review of 3D surface shape measurement using various optical methods. Raja [2002] reviewed the evolution of filters that were defined in standards for surface characterizations. Later, Blunt [2003] proposed 3D surface parameters and the utilization of advanced filtering techniques including wavelets and robust Gaussian methodologies. Other approaches to characterize surface shape include interpolation and extrapolation using spatial

dependent data points [Yang et al., 2000; Xia et al., 2008; Jin et al., 2012], least squares algorithm [Zhu et al., 2004], B-spline [Grove, 2004], etc.

4.1.2.2 Characterization of machined surface form/texture

Another line of research has been focused on the impact of machining process conditions on surface form and texture at multiple scales. At fine scales (micron level), surface textures were correlated to a number of process conditions. Tool conditions were found to have a significant impact on surface texture [Wilkison et al., 1997; Liao et al., 2009). Schmitz et al. [2006] correlated tool runout, stability, and surface location errors to surface finish. Baek at al. [1997] introduced a model to predict surface roughness based on cutting conditions, edge profile, insert runout, and dynamic characteristics. Kline et al. [1983] showed the effects of radial runout and chipload on surface finish. Surface errors were also predicted along with cutting force considering system deflections [Sutherland et al., 1986]. At coarse scales (> several millimeters), Takeuchi et al. [1964] studied the effects of spindle tilt and thermal expansion on the surface form error. Camelio et al. [2004] investigated the effect of fixturing and clamping on surface form error. Liao et al. [2001] used finite element analysis to study the influence of clamping and machining force on the machined surface quality. The method proposed by Gu et al. [1997] using the equivalent flexibility influence coefficient could predict the relative position between the cutter and workpiece and thereby estimate surface errors. Aris [2008] investigated the surface generation during the machining process and the associated functionality formation.

Thanks to the advances of high definition metrology system, many researchers have taken various approaches in characterizing 3D surfaces. [Zhang, 2007] proposed a measurement scheme and classification methods for dimensional and surface quality characteristics in powertrain manufacturing processes. [Li, 2009] further proposed strategies to integrate

dimensional and non-dimensional information for better quality inspection, process diagnosis and performance analysis. An as-manufactured CAD model is developed to encode high definition features that can include geometry dimensions, surface texture, and physical attributes. [Liao, 2010] proposed methodology on extracting 3D surface features from waviness scale and related extracted features in predicting tool wear, and surface function. [Nguyen, 2013] focused on charactering surface variation and control in face milling. High definition surface patterns are extracted and correlated with cutting force. High cutting force variation was found to have a positive correlation with surface variation. A model that can optimize cutter path and cutting condition to redistribute cutting force was proposed to reduce surface variation. [Puchala, 2013] proposed methods to achieve surface variation control by considering both the process variables and high definition measurements (HDM) in developed surface model. In addition, HDM data was also applied in development of a morphing-based model to monitor multistage variation.

4.2 Proposed methodology

Approaches to extract surface shape can be classified into two general categories: the parametric method and non-parametric method. The first approach has the advantage of having explicit expression of the surface while the second approach normally can preserve more local details (e.g., B-splines). The framework we proposed is based on the parametric method because one of the objectives of our research is to extract an explicit expression of the surface that can describe the general shape of a machined surface. Variations in process usually result in different types of shape of the machined surfaces. Extracted parameters can be used to classify these surface shapes into different categories. Control charts can also be established to monitor the shape variation for each type of shape. The impact of different process parameters on the

generation of machined surfaces can be analyzed by correlating the identified surface shape and process information. This can help engineers to make appropriate adjustments in process to improve the surface quality and reduce manufacturing cost.

Some local details will be lost in the first step to extract general shape of a machined surface. However this would not affect the second step for multi-scale analysis since raw data is still used. Details in high definition data will be extracted based on different applications. For example, known machining parameters can be applied to extract specific sub-surface from high definition measurement that contains tooling marks in the inspection of abnormal surface patterns. Unlike other researchers' work, which focuses on the extraction of general shape for CAM/CAD or just quality evaluation, the proposed methodology takes a full measurement of a machined surface. It produces a framework on how to analyze surface at different spatial scales that can help researchers to develop tools for better surface characterization and control. Figure 4.4 explains the strategy used to extract surface shape and conduct the evaluation of functional performances.

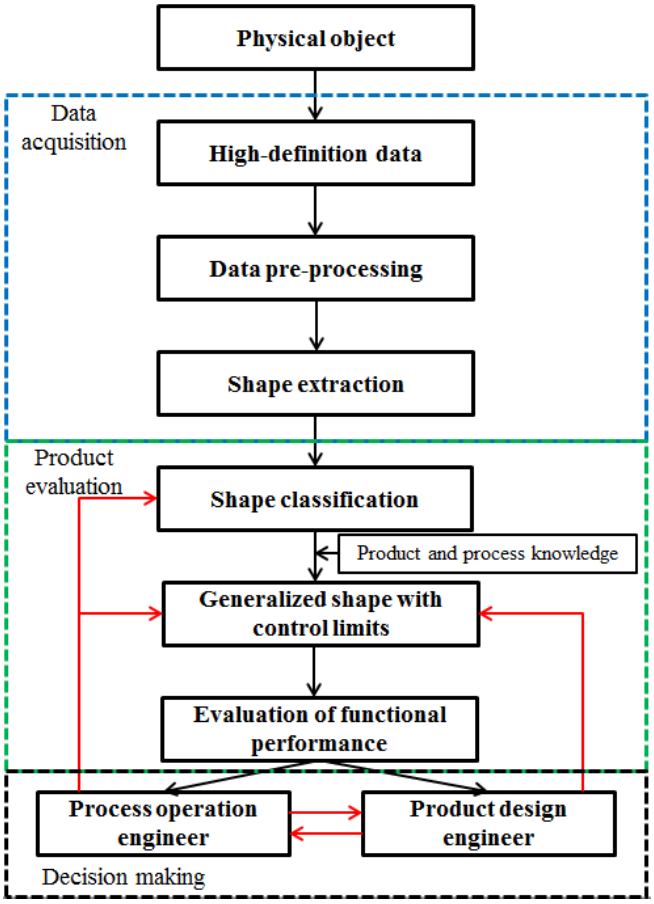

Figure 4.4 Flowchart of surface shape extraction and evaluation

In this research, the machined surfaces were measured using a digital holographic interferometry system. The lateral resolution is 150 μm and vertical resolution is 0.05 μm [Coherix, 2008]. The field of view of each measurement is 300 mm by 300 mm. Data will be pre-processed to exclude noise and outliers. The shape is extracted using an enhanced robust least squares surface algorithm [discussed in Sec 2.3.2]. The case study in 4.3 has a detailed explanation of conducting quadratic surface approximation as an example. Then, all extracted surfaces will be classified into different categories based on their types, such as parabolic surface, hyperbolic surface and etc. Generalized shape with control limits can be established with the consideration of product and process knowledge. Shape of a machined surface reflects the

impact of process parameters. Thus, classified shapes can be analyzed to study how different process parameters can affect the shapes of machined surfaces. The above strategy can be described as follows: 1) categorize different shapes with similar measurements of flatness; 2) correlate the abnormal surface shape with process parameters; 3) cross-link the shape with functional performance of the produced parts; and 4) adjust process parameters to improve machining quality.

An example of functional performance evaluation is the prediction of potential surface distortion in assembly. Machined surface with undesired shapes may cause distortion in product after assembled with mating surface. Applying the proposed methodology to characterize surface shape can help engineers take actions to prevent the occurrence of inappropriate assembly. Moreover, process engineers can also gain knowledge revealed from this analysis and make adjustment in machining process to produce product component with desired shape that can achieve the functionality of a product. This is superior to use a single flatness value to evaluate the entire surface of a machined component: 1) better capability to monitor critical areas; and 2) cost-effective process control can be established to avoid excessive cost on machining.

At fine scale, multiple methodologies can be applied to analyze the surface at different lateral resolutions. Figure 4.5 shows the proposed strategy. The data being used in fine scale comes from the raw high definition data after pre-processing. With the consideration of product and process information, data at specific lateral scale can be extracted to be used in specific analysis. For example, tooling marks observed on a surface after face milling can be extracted to estimate the tool wear. Given the machining parameters (e.g., feed rate, spindle speed and number of inserts), the spacing between two adjacent tooling marks can be estimated. Then the surface information of this specific scale can be reconstructed. [Liao et al., 2010] has conducted

research on the development of metric in surface waviness range that correlates to tool wear. The developed metric S_{wa} from surface measurement can then be used to evaluate the real time tool wear condition. Developed metrics at fine scale are usually independent, thus the applications can be conducted simultaneously to improve the efficiency of analysis.

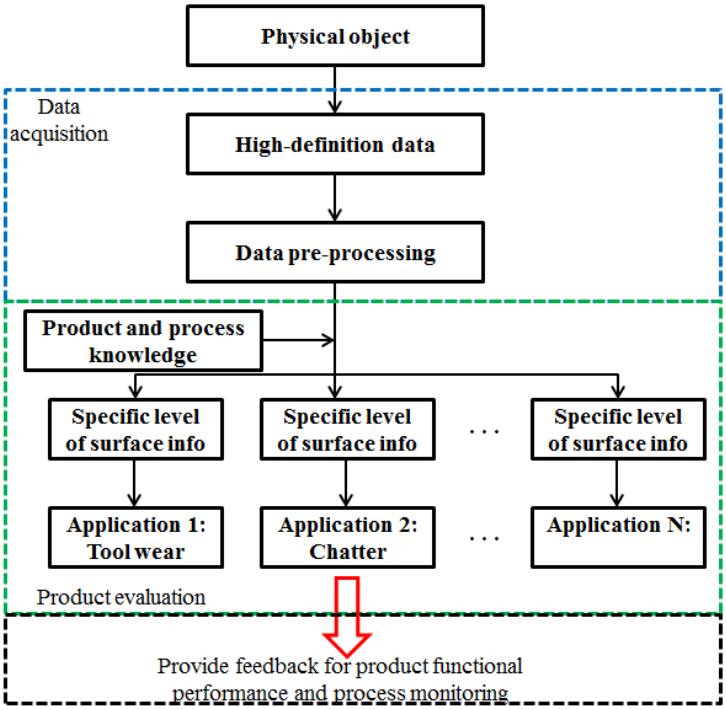

Figure 4.5 Flowchart of surface characterization at fine scale

In the next two sections, case studies will be given to demonstrate how to analyze high definition surface measurements using the proposed methodology. One focuses on the utilization of generalized shapes and the other one demonstrates how to develop an application for machining condition monitoring at fine scale with the consideration of machining parameters.

4.3 Surface quality inspection using generalized surface shape

Clutch piston is an important component in the automotive transmission. Figure 4.6 shows a schematic plot of the position of a clutch piston in working. The contact surface of the clutch piston should be flat to guarantee pressure is distributed evenly. Otherwise some local

areas will have high pressure that may damage the clutch disk. Parts are cast by a supplier. Each die has 4 cavities (Figure 4.7). The outer ring of the clutch piston (4&5 in Figure 4.7) is machined on lathe.

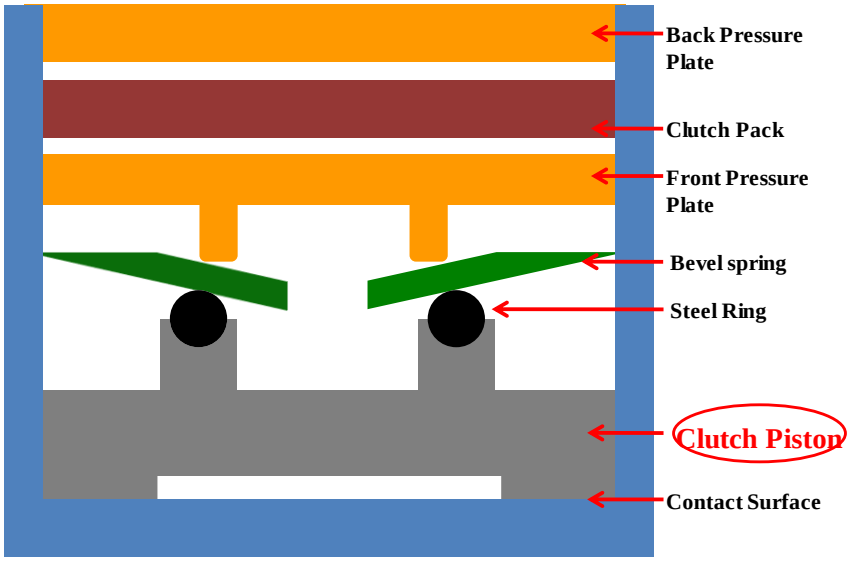

Figure 4.6 Schematic plot of a clutch piston in working condition

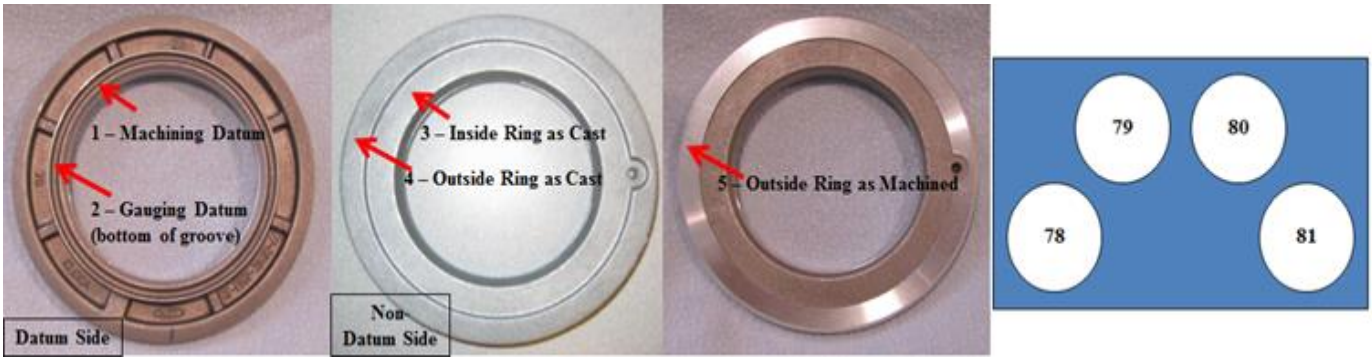

Figure 4.7 Image of clutch piston and illustration of casting die and cavities

The specification on the outer ring is 250 μm for overall flatness. Due to high scrap rate, the cast parts were inspected 100% by the supplier using dial indicator before sending out to OEMs. And the OEMs also conducted 100% measurement of the outer ring surface using dial indicator after machining.

Both the machined surface and cast surface of the inside ring of 20 parts were measured using a Coherix ShaPix 3000 system. All the parts were from cavity No. 78. Figure 4.8 shows the measurement results of overall flatness for machined surface (outside) and cast surface (inside). 8 out of the 20 parts had overall flatness of machined surface above 250 μm. The correlation coefficient of the machined and cast flatness is 0.9926. They are highly correlated. This means the measurements of overall flatness of the inside cast ring can be used to estimate if a cast part is good or not before taking the milling operation. However, incorrect judgment might occur as the flatness from inside ring is always smaller than the flatness of machined outside ring of same part based on our observations.

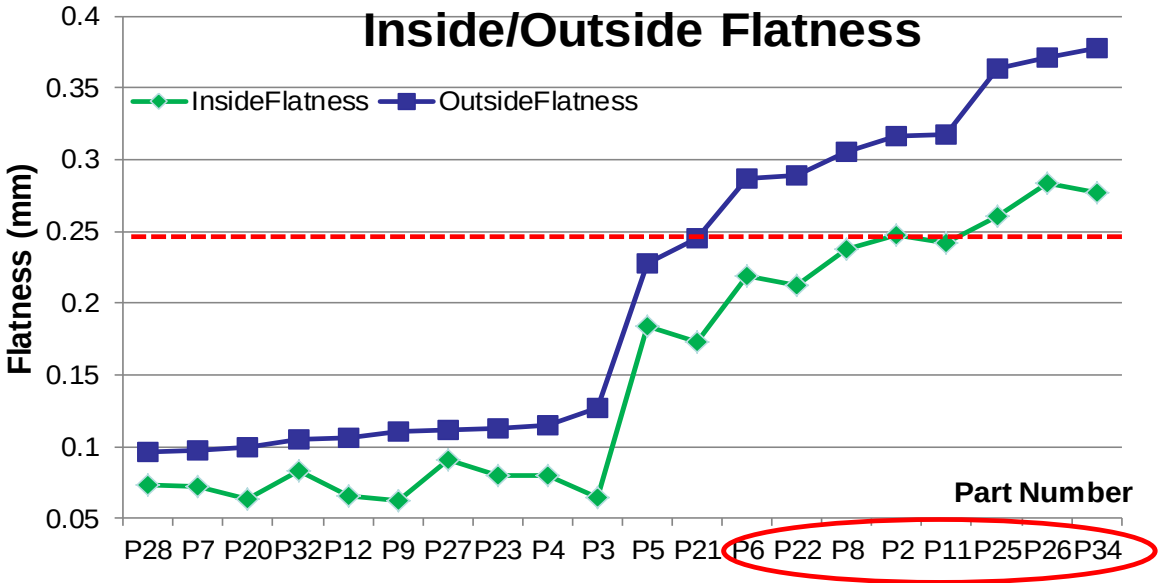

Figure 4.8 Measured flatness of machined surface and cast surface

Instead of using only the flatness to evaluate the surface quality, we fitted polynomial surface of the measurements. Generally speaking, a polynomial surface can be expressed as:

$$z(x,y)=\sum_{i=0}^{n}\sum_{j=0}^{i}a_{[i-j,j]}x^{i-j}y^{j} \quad \text{.....(4.1)}$$

And the corresponding sum of squares of surface asperity departures from this polynomial plane is given by:

$$\varepsilon^2 = \sum_{l=1}^{N}\sum_{k=1}^{M}(z_0(x_k, y_l) - z(x_k, y_l))^2 = \sum_{l=1}^{N}\sum_{k=1}^{M}(z_0(x_k, y_l) - \sum_{i=0}^{n}\sum_{j=0}^{i} a_{[i-j,j]} x^{i-j} y^j)^2 \quad \text{.....(4.2)}$$

For the simplicity, we can denote that,

$$q_p = z_0(x_k, y_l),\ g_p = z(x_k, y_l),$$

$$u_p = x_{p-[p/M]\cdot M} = x_k,\ v_p = y_{[p/M+1]\cdot} = y_l \quad \text{.....(4.3)}$$

Where, $p = (l-1)M + k$ and [.] in Eq. (4.3) represents taking the integer part of the result. Thus Eq. (4.2) can be simplified as

$$\varepsilon^2 = \sum_{p=1}^{M\times N}(q_p - g_p)^2 = \sum_{k=1}^{M\times N}(q_p - \sum_{i=0}^{n}\sum_{j=0}^{i} a_{[i-j,j]} u_p^{i-j} v_p^j)^2 \quad \text{.....(4.4)}$$

The coefficients a_{ij} are determined by minimizing Eq. (4.4) Thus, by differentiating Eq. (4.4) with respect to the coefficients and equating them to zero, we get

$$\frac{\partial \varepsilon^2}{\partial a_{ij}} = 0 \text{ , (} i = 0, 1, 2, \ldots, \text{n, } j \le i \text{)} \quad \text{.....(4.5)}$$

The normal equation of the least square problem can be represented in matrix form:

$[V]^T[V]\{A\} = [V]^T\{Q\}$, Where,

$$[V] = \begin{bmatrix} 1 & u_1 & v_1 & u_1^2 & u_1v_1 & \cdots & u_1v_1^{n-1} & v_1^n \\ 1 & u_2 & v_2 & u_2^2 & u_2v_2 & \cdots & u_2v_2^{n-1} & v_2^n \\ \vdots & \vdots & \vdots & \vdots & \vdots & \cdots & \vdots & \vdots \\ 1 & u_p & v_p & u_p^2 & u_pv_p & \cdots & u_pv_p^{n-1} & v_p^n \end{bmatrix},\ \{A\} = \begin{Bmatrix} a_{00} \\ a_{10} \\ a_{01} \\ a_{11} \\ a_{20} \\ \vdots \\ a_{1(n-1)} \\ a_{0n} \end{Bmatrix},\ \{Q\} = \begin{Bmatrix} q_1 \\ q_2 \\ \vdots \\ q_p \end{Bmatrix} \quad \text{.....(4.6)}$$

Eq. (4.6) can be solved by employing the Gauss-Jordan elimination and the LU decomposition to perform the linear algebra, and finally leads to

$$\{A\} = ([V]^T [V])^{-1} [V]^T \{Q\} \quad \text{.....(4.7)}$$

After deriving the above equations, another important issue is to determine the order of the polynomial surfaces. Stout [1993] had evaluated different orders of polynomial surface fitting. In their test, the non-biased residual variances of the first order polynomial (n=1) are much higher than those of higher orders, while their reduction is not significant from n = 2, to n = 4. For even higher orders, the results became divergence. Therefore, we selected n =2 for this clutch piston surface. There are six coefficients generated from Eq.4.6 for quadratic least squares surface fitting. To standardize the evaluation of the fitted surface, the function representing the quadratic surface can be described as:

$$Z(x, y) = a_1 \cdot x^2 + a_2 \cdot y^2 + a_3 \cdot x \cdot y + a_4 \cdot x + a_5 \cdot y + a_6 \quad \text{.....(4.8)}$$

A quadratic function can be converted into canonical form which provides simple ways to present a machined surface shape using up to only three parameters and each parameter has a clear geometric interpretation (Figure 4.9). The quadratic surface function can be converted to its canonical form by substituting Eq.(4.9) into Eq.(4.8)

$$a_1 = \frac{\cos^2\theta_z}{A^2} + \frac{\sin^2\theta_z}{B^2}$$

$$a_2 = \frac{\sin^2\theta_z}{A^2} + \frac{\cos^2\theta_z}{B^2}$$

$$a_3 = \frac{\sin 2\theta_z}{B^2} - \frac{\sin 2\theta_z}{A^2} \quad \text{.....(4.9)}$$

$$a_4 = \frac{2x_0\cos^2\theta_z - y_0\sin 2\theta_z}{A^2} + \frac{2x_0\sin^2\theta_z + y_0\sin 2\theta_z}{B^2}$$

$$a_5 = \frac{2y_0\sin^2\theta_z - x_0\sin 2\theta_z}{A^2} + \frac{2y_0\cos^2\theta_z + x_0\sin 2\theta_z}{B^2}$$

$$a_6 = \frac{(x_0\cos\theta_z - y_0\sin\theta_z)^2}{A^2} + \frac{(x_0\sin\theta_z + y_0\cos\theta_z)^2}{B^2}$$

A canonical form of Eq.(4.8) can be shown as:

$$Z(x,y) = \pm\frac{x^2}{A^2} \pm \frac{x^2}{B^2} \quad \text{.....(4.10)}$$

The values of A, B and the $\pm$ signs are extracted as metrics to evaluate the shape of the surface of clutch piston.

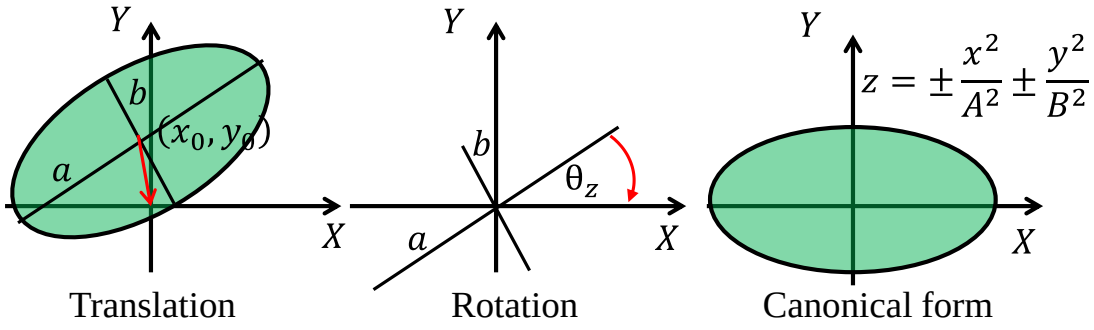

Figure 4.9 Converting a quadratic surface into canonical form via translation and rotation

Thus, the general shape of a measured clutch piston surface can be fitted using method described above. We discovered parts that failed to meet the flatness requirement had the same type of shape for its cast inside ring surface and machined outside ring. Figure 4.10 shows the four types of shape observed in the 20 parts. All of the 8 defective parts had the (-1, 1) type hyperbolic shape in inside cast surface, and none of the normal parts had this type of surface. For

a quadratic surface in canonical form, a surface can be categorized into one of the four groups by looking at the signs of coefficients (i.e**.,+ +, + -, - -, - +).** The milling process on outside ring will not change the overall surface shape of a cast clutch piston. Therefore, the OEMs can replace the manual inspection with the digital holographic interferometry system. It can conduct surface inspection on inside cast surface before machining and rejecting nonqualified cast parts based on the extracted shape of measured surface. This can increase the throughput and reduce the scarp rate and costs.

	Inside (cast)		Outside (machined)	
Part Name	Sign of A x axis	Sign of B y axis	Sign of A x axis	Sign of B y axis
M78P9	-1	-1	-1	-1
M78P20	1	1	1	1
M78P3	-1	1	1	1
M78P12	1	1	1	1
M78P7	-1	1	1	1
M78P28	-1	-1	1	-1
M78P23	1	1	1	1
M78P4	1	-1	1	1
M78P32	1	1	1	-1
M78P27	-1	1	1	-1
M78P21	1	-1	1	-1
M78P5	1	-1	1	-1
M78P22	-1	1	-1	1
M78P6	-1	1	-1	1
M78P8	-1	1	-1	1
M78P11	-1	1	-1	1
M78P2	-1	1	-1	1
M78P25	-1	1	-1	1
M78P34	-1	1	-1	1
M78P26	-1	1	-1	1

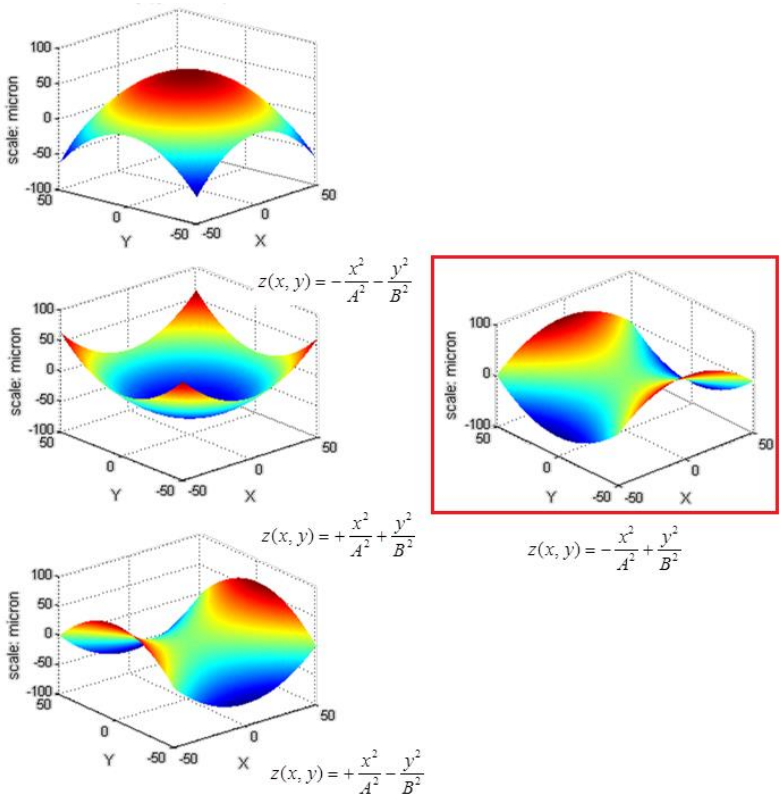

(a) (b)

Figure 4.10 Generalized surface shape of clutch piston: (a) Comparison of surface shape before and after machining, (b) Four identified surface shapes of fitted surface

4.4 Abnormal surface pattern detection

Abnormal surface patterns like chatter on machined surface have been discovered and studied for over a century since by [Taylor, 1906]. However, undesired surface pattern still exists and occurs unexpectedly due to various root causes, such as the inappropriate setup of fixture and machine tools. The impacts of abnormal process conditions cause poor product quality and lower throughput. Extensive research work has been conducted in order to detect these abnormal surface patterns [Khalifa and Densibali, 2006; Kim et al., 2007; Kuljanic et al., 2008; Wang and Liang, 2009; Yao et al., 2010;]. With the availability of high definition surface measurement, we are able to develop an abnormal surface pattern detection algorithm with the consideration of known process knowledge.

In the time-frequency domain, wavelet transform is capable of providing user with the frequency of signals and the time associated to those frequencies. This makes wavelets a widely adopted tool in the detection of faulty signals. Given surface measurements in spatial domain, we can apply different surface wavelengths to analyze the measurement in time-spatial domain. Different surface wavelengths are reflected by the sampling rate of the measurement data. A sample refers as the value of the pixel picked up in the space. For different sampling rate, samples are picked up at different spatial intervals. Figure 4.11 shows several different sampling rates applied on the same data set. Each cell represents a pixel of 150 μm by 150 μm. The black cells on the four rows represent pixels which are picked during sampling. They represent wavelengths of 0.15mm, 0.3mm, 0.6mm and 1.5mm, respectively. The sampling rate is defined as the reciprocal of wavelength.

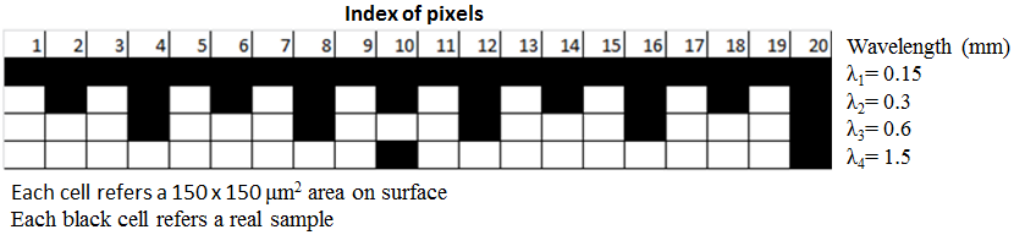

Figure 4.11 Sampling rate in spatial domain

Another advantage of applying wavelets in this study is due to its high efficiency in data compression. Wavelet compression has been commonly used for image compression. The goal of it is to store as many as details of an image while use as little space as possible. On one side, HDM data provides abundant details of a measured surface. On the other, the size of a HDM is usually much larger than measurements taken by conventional methods. Surface measurements of the same type of workpieces under normal condition tend to look similar to each other. Abnormal patterns occur when condition changes from normal level. Thus, a practical issue we have to face is we need to find a good method can process data efficiently and keep as many details as possible. Thus, wavelets are well suited for the approach proposed in this dissertation.

The developed algorithm will be described step by step. First of all, the wavelets used for decomposition are selected. After that, a reference surface set can be established on the dimension of the product, machining information of the operation, and other known process information. The reference set will serve as the initial benchmarks for identifying abnormal patterns. As the manufacturing process continues, new measurements of normal and abnormal surfaces become available. The algorithm can then establish benchmarks using real measurements to replace the initial reference surface.

4.4.1 Selections of wavelets

First of all, we need to determine which mother wavelet we will apply for data analysis. The objective is to select the correct wavelength regime that is more sensitive to the occurrence of abnormal surface pattern when we analyze high definition data. We want to avoid data loss as much as possible because the reconstructed data would be used to identify if a measurement contains abnormal pattern or not. There are two requirements need to be satisfied to achieve perfect reconstruction for a given filter bank:

1) $H(-z)\tilde{H}(z)+G(-z)\tilde{G}(z)=0$ to avoid aliasing……...……..…..(4.12)

2) $H(-z)\tilde{H}(z)+G(-z)\tilde{G}(z)=cz^{-k}$ to avoid distortion

Perfect reconstruction cannot be achieved if the same set of scaling and wavelet functions are applied for signal decomposition and reconstruction. This is the case when orthogonal wavelets are used (except Haar wavelet) since they are orthogonal and symmetric. Cohen, Daubechies developed a method to create biorthogonal basis with symmetry by sacrificing the orthogonality of scaling and wavelet function. The biorthogonal condition was used to replace the original condition for scaling and wavelet function. Thus, biorthogonal basis can be used to achieve perfect reconstruction of the signal. This is very important in our study since we focus on looking at data that is reconstructed from specific decomposed details.

Fu [2003] compared several common wavelets in analyzing engineering surfaces. Bior 6.8 is more suitable than other wavelets (shown in Figure 4.12). It inherits most of the aforementioned advantages. Moreover, it uses different functions for decomposition and reconstruction. The advantage of using different scaling and wavelet function in decomposition and reconstruction is that better accuracy in the reconstruction of data can be achieved. Since one

or more reconstructed signals are always being used in feature selection and fault diagnosis. The accuracy of the reconstructed signal is critical to the final results.

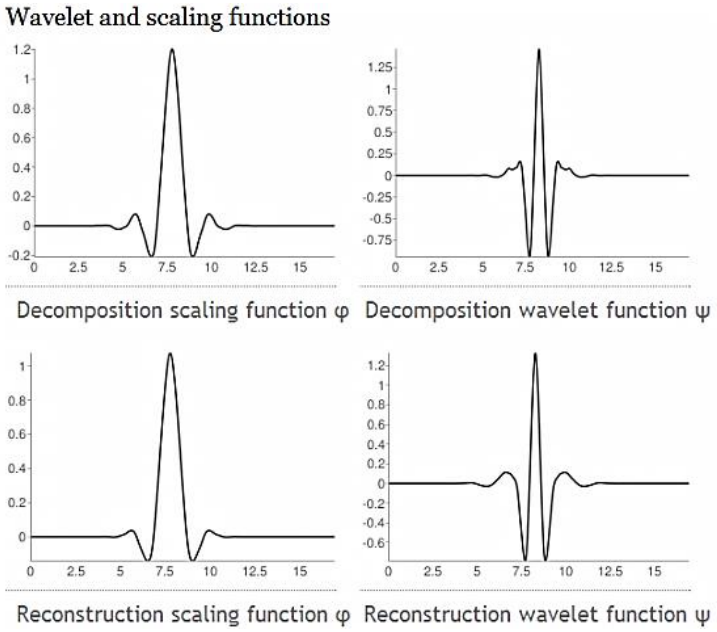

Figure 4.12 Bior 6.8 wavelet and scaling function for decomposition and reconstruction[5]

4.4.2 Establishment of the reference set

To establish the standard reference set, some information about the machining processes and the dimensions of the workpiece should be obtained in advance. In this section, we will propose an approach to establish a standard reference set based on the dimensions of workpiece, cutting tool information, feed rate, spindle speed and other parameters and constants. If possible, we also want to have a further classification on workpieces that are identified as defective workpieces based on the problem levels. For example, spindle bearing problems usually cause vibrations shown as short wavelength pattern while workpiece looseness in fixture usually cause vibrations shown as long wavelength. Since not all abnormal processes will leave marks that can

[5] http://wavelets.pybytes.com/wavelet/bior6.8/

be seen by human on the surface. We should be able to identify those processes would not leave clear mark. Here is an example of constructing a set of standard references on a workpiece.

In our study, a set of compacted graphite iron (CGI) measurements in the dimensions of 58.42 mm (2.3'') in width and 215.9 mm (8.5'') in length were milled on machine using a 101.6 mm (4'') cutter with 5 teeth. During the milling process, two sets of parts were machined. One set of workpieces were milled under normal condition, while workpieces in the other set were machined with intentionally loosened fixture. As excessive vibration would occur due to loosened fixture, the cutter would leave abnormal surface pattern during milling process. Thus, we can obtain two sets of initial measurements. As the dimension of the workpiece is known, the levels of decomposition can also be determined.

4.4.3 Automatic band selection and threshold establishment

As usual, machining process information is required and it should include: (1) Basic product dimensions (width and length); (2) Effective cutter size; (3) Spindle speed; and (4) Feed rate. Required measurements should include several workpieces under normal conditions (at least three measurements) and at least one defective workpiece with abnormal surface pattern.

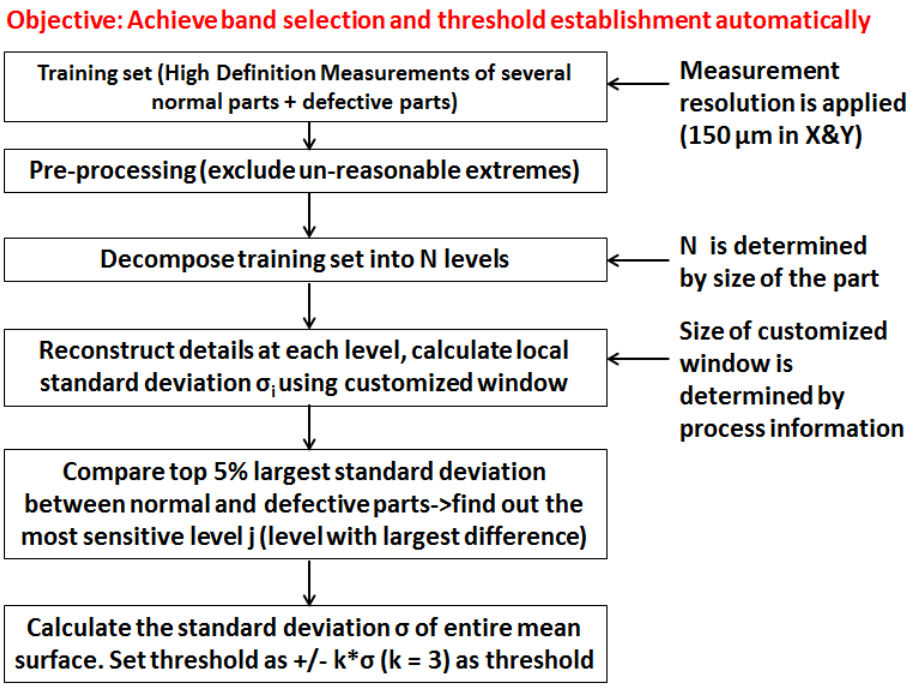

Figure 4.13 Flow chart of auto-band selection

Figure 4.13 shows the flow chart for automatic selection of band for abnormal surface pattern detection. The first step is to arrange all the eligible data in training set the same form. Then, a pre-processing will be taken on all eligible data sets to exclude unreasonable extremes. The definition of unreasonable extremes can be customized by operators. In this research, a data point is set as extreme value if it exceeds 20 times of the standard deviation of each individual surface.

The flowchart above explains how a specific level of wavelets is select. According to the theory of Nyquist sampling theory, a signal can be reconstructed without aliasing if the sampling rate is at least two times faster than the rate of desire signal. The X-Y resolution of measured surface equals to 150 µm. Thus, the minimum wavelength we can detect is above 300 µm. The geometric dimensions of workpiece (Length and Width) are used to determine the upper limit of detectable wavelength of a given workpiece. The minimum value between length and width is selected and denoted as $Min(L,W)$. To ensure the accuracy of result, a conservative move is

taken that the upper limit is defined as $\frac{Min(L,W)}{2}$. In summary, the range of wavelengths we can detect under current available data is $\left(0.3, \frac{Min(L,W)}{2}\right)$ (mm). And we know the relationship between the level of decomposition and the dimension of the workpiece. Therefore, we can also determine the total levels of decomposition (shown in Figure 4.14).

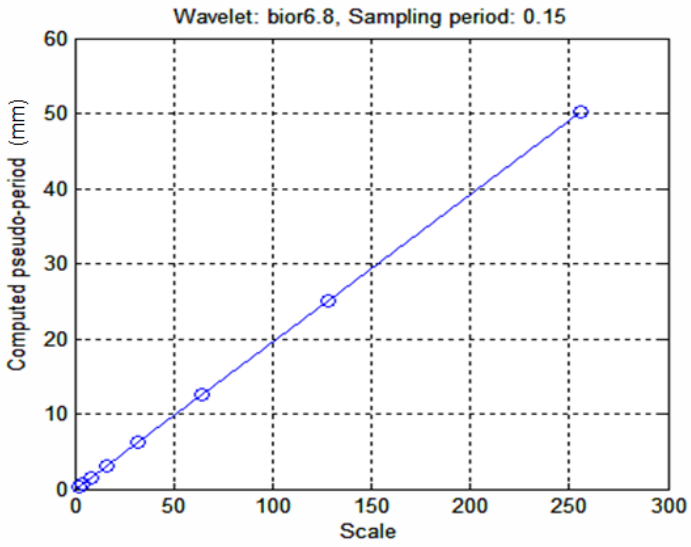

Level	1	2	3	4	5	6	7	8
Wavelength (mm)	(0, 0.39]	(0.39, 0.78]	(0.78,1.57]	(1.57, 3.14]	(3.14, 6.28]	(6.28, 12.55]	(12.55, 25.12]	(25.12,50.24]

Figure 4.14 Relationship between the level of decomposition and corresponding range of sensitive wavelengths

The moving window used in the algorithm (shown in Figure 4.15) is determined by considering the dimensions of the workpiece and machining parameters. The length of the moving window is set to equal the distance that the milling cutter completes one revolution in the feed direction. The width of the moving window is set to three. By selecting three pixels in the width, we can capture the variation in the direction that perpendicular to the feed direction. The moving window moves pixel by pixel, and we always would like to put the current pixel in the

center of moving window. Therefore, if an even number of the window length is calculated, we always ceil it up by one to make it an odd number.

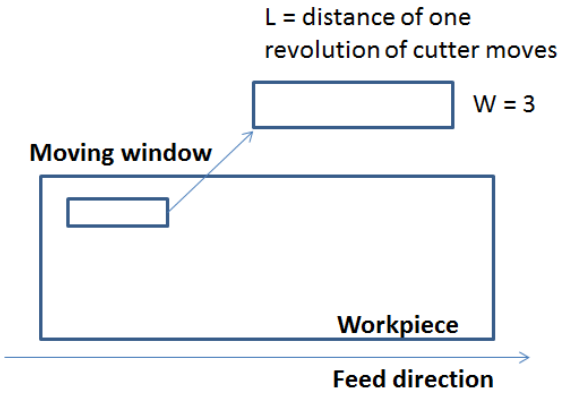

Figure 4.15 Definition of moving window used in algorithm

As more than one level will be decomposed for a measurement, looking at all of them every time is inefficient in terms of in computation efficiency. Also, when abnormal process occurs, it always has significant impacts on a specific spatial domain. Therefore, it would be more appropriate to focus on the specific spatial domain with largest variations.

After determining the total levels need to be decomposed on the high definition surface measurements, the top 5% largest standard deviation of each level of reconstruction of each workpiece is summed and denoted as $STD_{normal,i}$. The same statics is calculated for the known defective workpiece and denoted as $STD_{defectove,i}$. The differences between normal and defective measurements are then calculated on a level-by-level basis. And the level with largest difference is selected as the level for abnormal surface pattern detection $Max(DiffSTD_i)$, where $DiffSTD_i$ is defined as:

$$DiffSTD_i = STD_{defective,i} - STD_{normal,i}\ ,\ i = 1,...,N \quad \text{.....(4.9)}$$

The thresholds used for identifying abnormal surface pattern are defined as the variation of mean surface of all normal measurements in training sets. The k is set equals to 3 in this research as initial default setting and it can be customized by the operators.

4.4.4 Abnormal surface pattern detection algorithm using digital holographic data

All determined parameters and thresholds will be automatically saved for this specific type of workpiece with its corresponding process information. It can be applied immediately on any new measurement of the same type. And Figure 4.16 shows the detection logic is similarly to the previous step. The difference here is we can skip the step to select the most sensitive level to reconstruct among the decomposed levels as it has already been determined.

The reconstructed detail image will then be examined using the thresholds generated previously. Locations of data points which exceed the threshold will be automatically stored. The result has two components: a binary image of the measurement to show where the abnormal surface pattern locates and a file records the information of all recognized abnormal patterns.

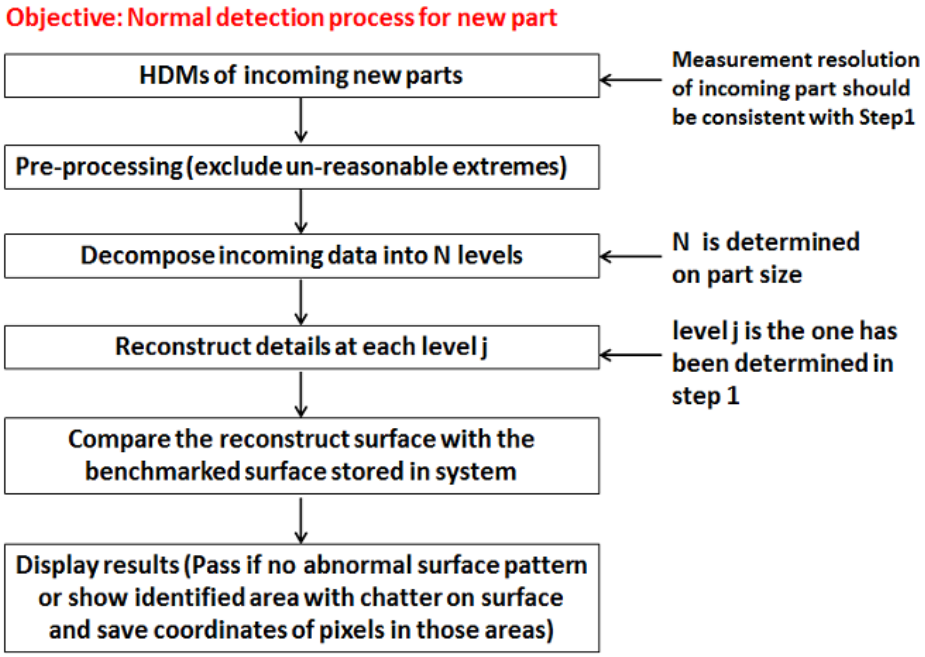

Figure 4.16 Abnormal surface pattern detection for incoming new measurement

CGI workpieces were milled using a 101.6 mm (4'') cutter with 5 teeth. The dimension of the workpiece is 58.42 mm (2.3'') in width and 215.9 mm (8.5'') in length. As the width of the workpiece is 58.42 mm and the range of wavelength that can be detected in spatial domain is (0.3mm, 29.21 mm). Therefore, N = 7 is set for decomposition based on the relationship between the level of decomposition and corresponding range of sensitive wavelength (Figure 4.14). The spindle speed is 470 rpm and the feed rate is 140 mm/min, feed per revolution is 0.29mm that equals to approximately 2 pixels. We set the window size to 3 to make it an odd number.

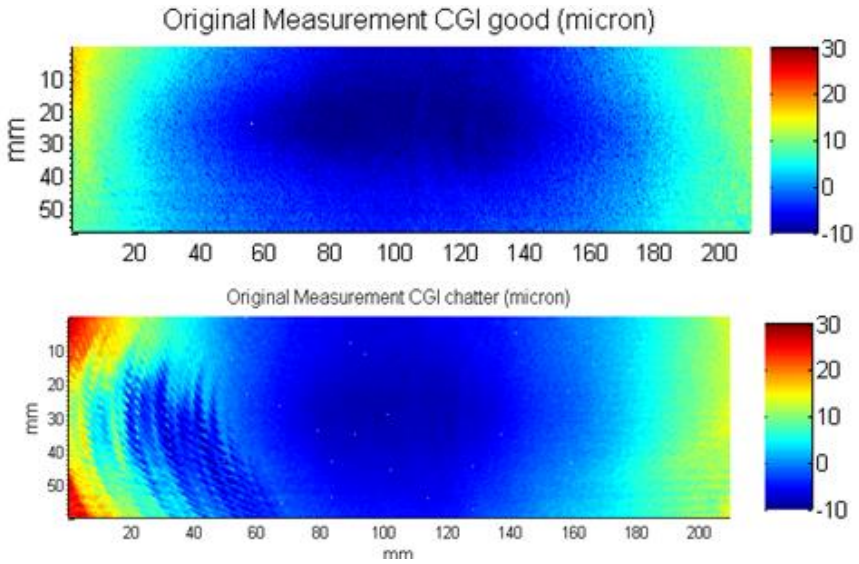

Figure 4.17 Measurements of CGI workpieces

Figure 4.17 shows the two images of CGI workpieces, the top one is a workpiece under normal condition, and the bottom one is the workpiece which has abnormal tooling marks. Based on the known dimension of the workpiece, the measurements are decomposed into seven levels respectively. Figures 4.18 and 4.19 show how the algorithm automatically identified the level with the highest surface height variations. Level 3 (represents wavelength ranges from 0.78 mm to 1.57 mm) is selected as the level for abnormal surface pattern detection. Figure 4.20 displays the reconstructed height map of CGI workpiece with identified abnormal surface patterns using coefficients from level 3. The binary map indicates where the abnormal pattern locates on the

surface. It shows clearly in Figure 4.20 (a) that these abnormal tooling marks have been successfully detected while normal part shows uniform surface.

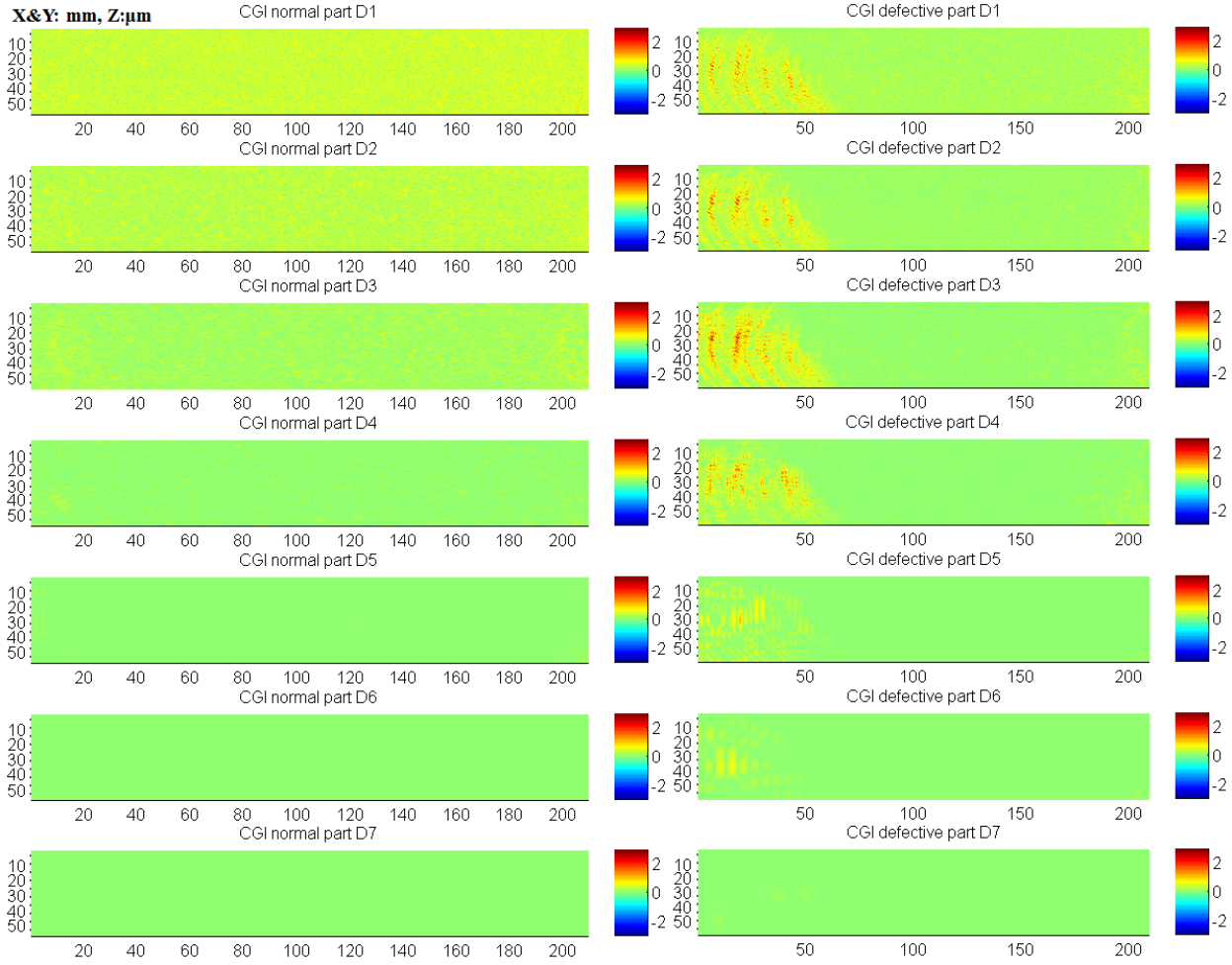

Figure 4.18 Comparison between normal and defective workpieces of reconstructed images from each level of CGI workpieces

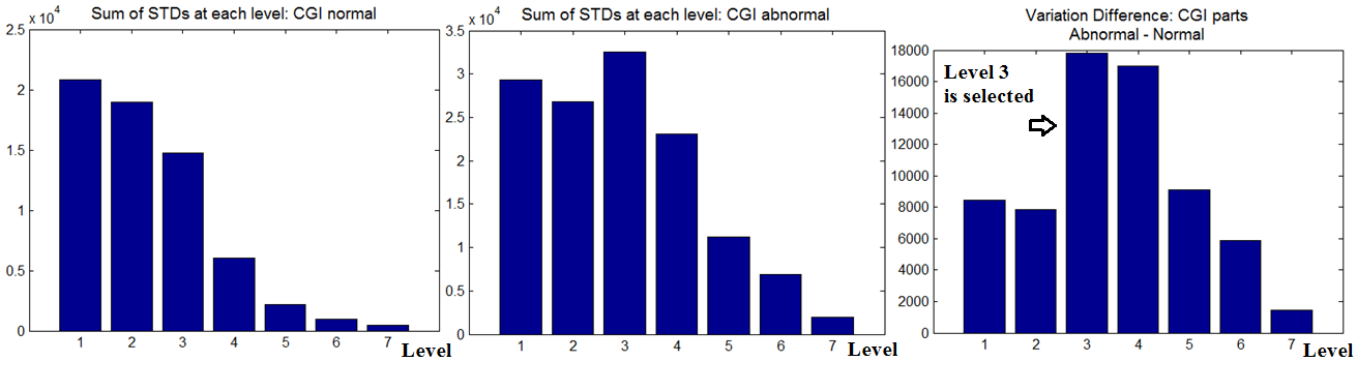

Figure 4.19 Automatic band selections for measurements of CGI workpieces

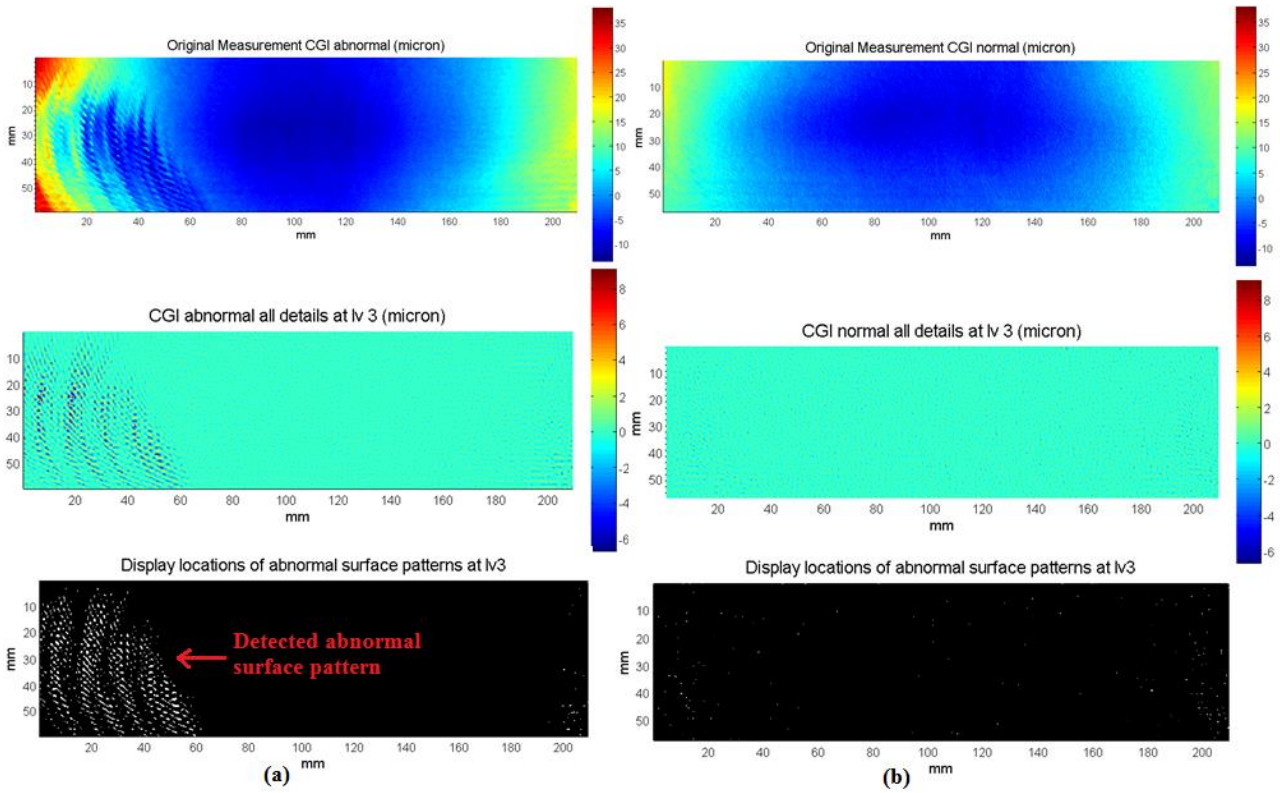

Figure 4.20 Abnormal surface pattern detection on CGI workpieces: (a) defective, (b) normal

Similarly, we are able to detect abnormal surface pattern automatically using this algorithm on aluminum workpieces (Figure 4.21). The original measurements are decomposed into seven levels after considering the size of work piece. The 4th level is automatically selected as it has the largest height variation between normal and defective parts (Figure 4.22). Comparison between normal and defective parts shows that the algorithm can clearly identify the location of abnormal tooling marks on defective part in Figure 4.23.

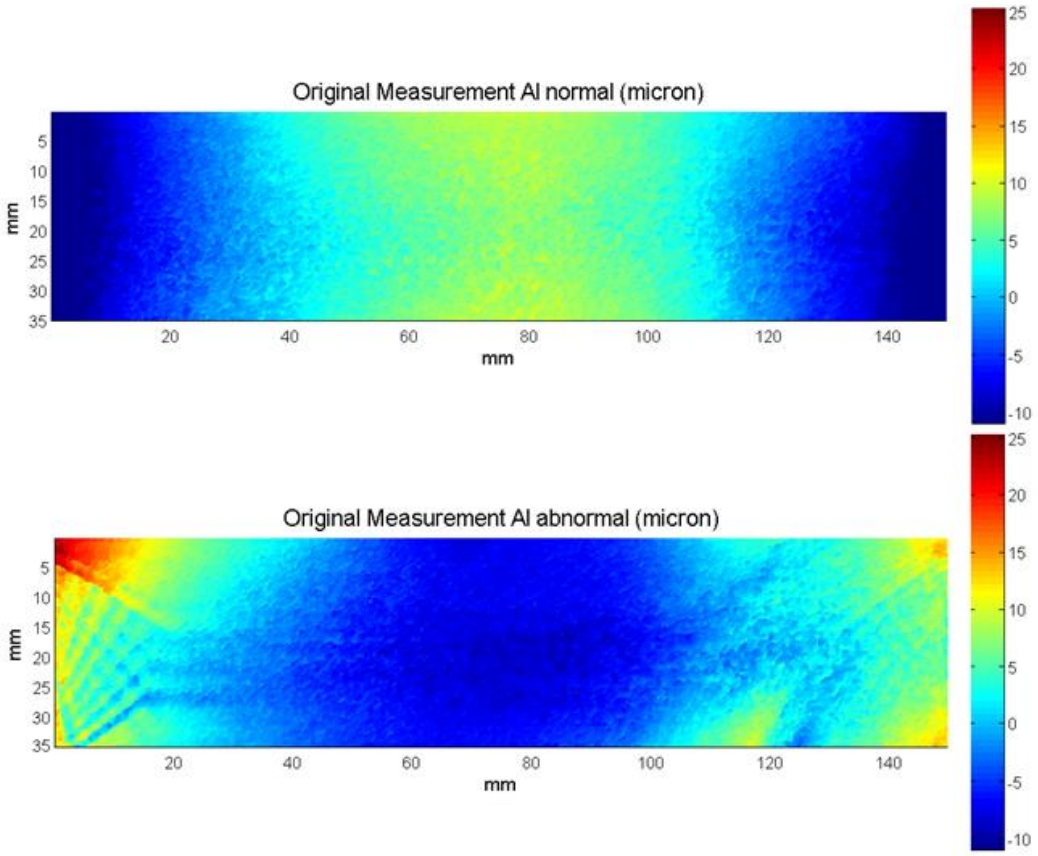

Figure 4.21 Measurements of aluminum workpieces

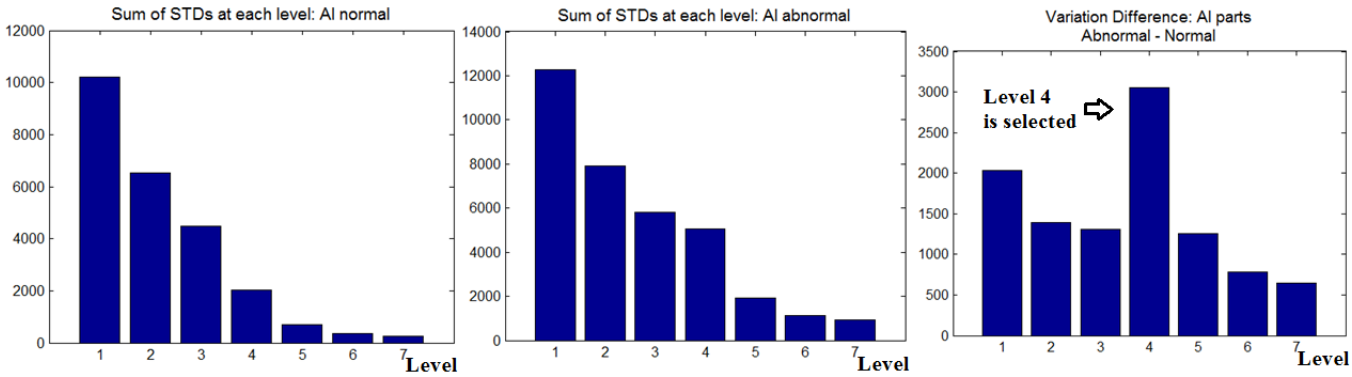

Figure 4.22 Automatic band selections for measurements of Al workpieces

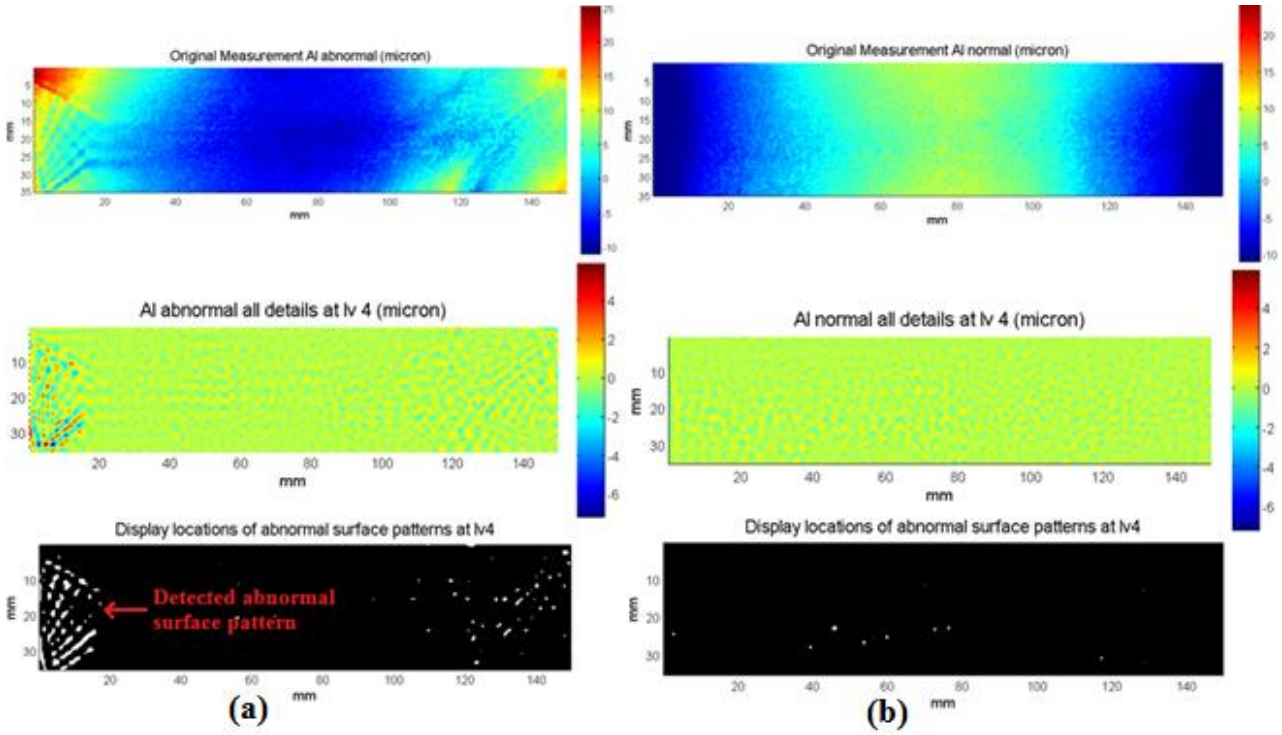

Figure 4.23 Detection results on Al workpieces: (a) defective, (b) normal

For surface with complicated features, the procedure is slightly different from analyzing simple flat surfaces. The major difference is that we add one extra step in the automatic band selection and threshold establishment. As border distortion will occur when using wavelets in analyzing data that is discontinuous, we apply a mask on data to reduce the unwanted effects brought by border distortion.

This addition step can be denoted as ‘Surface Mask’. First of all, the algorithm will perform a scanning over the entire input surface. It marks pixels with real number with ‘1’ and empty pixels with ‘0’. Secondly, it will perform a shrink function that the mask will shrink from any contours (either outer contours or inner features) by 2 pixels to avoid potential outliers that occur frequently at edges. Pixels that are recognized for shrinking will be replaced by ‘0’. In summary, the input is the reorganized surface and the output will be also a binary surface the same size as the input surface.

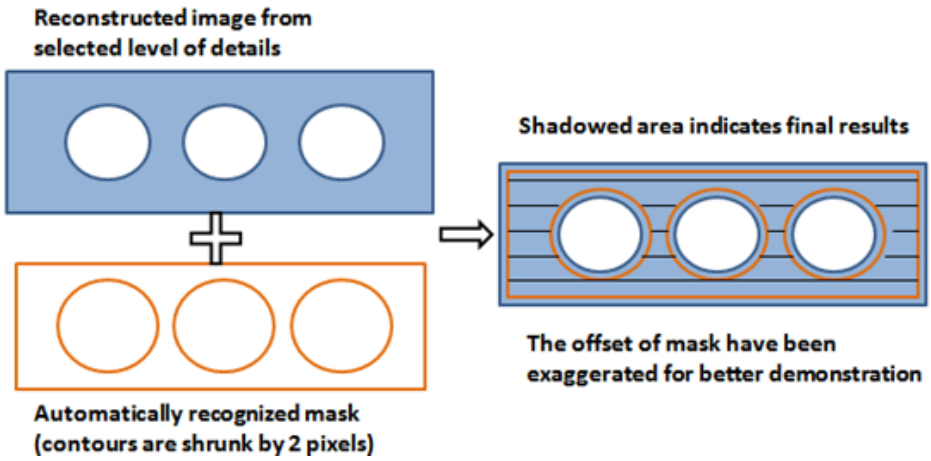

Figure 4.24 Illustration of generating a surface mask

Aluminum workpieces were cut using a water jet machine. The top surfaces of the workpieces were milled using a 101.6 mm (4'') cutter with 5 teeth. Figure 4.25 shows two images of measured aluminum workpieces after milling. The dimension of the workpiece is 68.08 mm (2.68'') in width and 177.8 mm (7'') in length. The width of the workpiece is 68.08 mm and the range of wavelength we can detect is (0.3mm, 34.04 mm). Therefore, N = 7 is set for decomposition. Figure 4.26 illustrates the reconstructed height maps at seven levels for both workpieces. The spindle speed is 3500 rpm and the feed rate is 2160 mm/min, feed per revolution is 0.62mm that equals to approximately 5 pixels (since it exceeds 4 pixels, so we round it up to 5 pixels). Thus the size of moving window is determined as 3 by 5. Figure 4.27 demonstrates that the algorithm can successfully identify the location of abnormal patterns on the surface at reconstructed level 2.

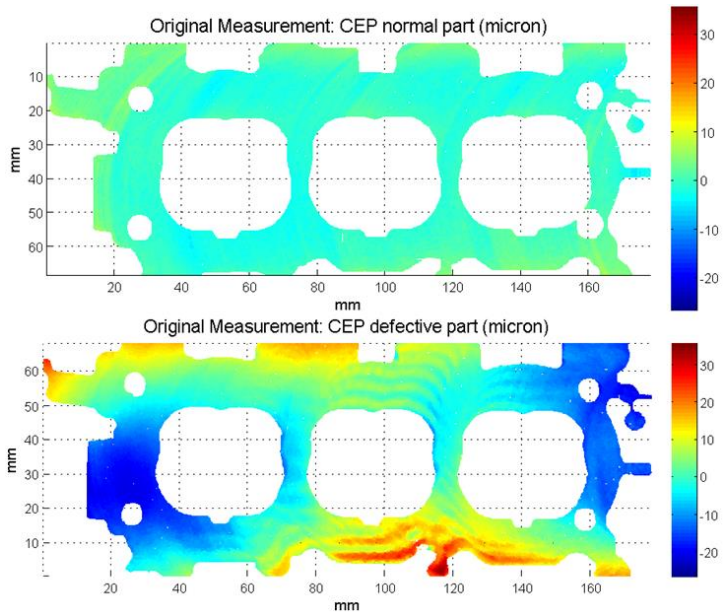

Figure 4.25 Measurements of aluminum workpieces with features

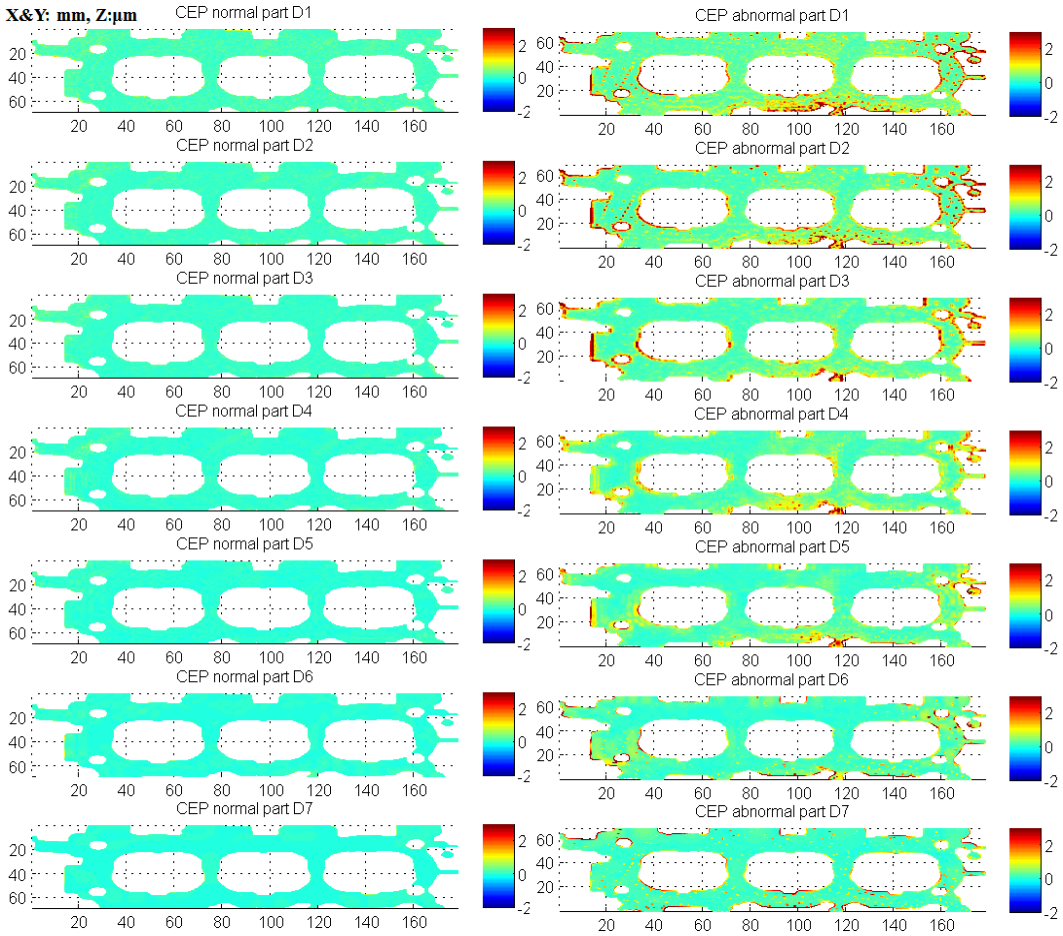

Figure 4.26 Comparison between normal and defective workpieces of reconstructed images from each level of aluminum workpieces

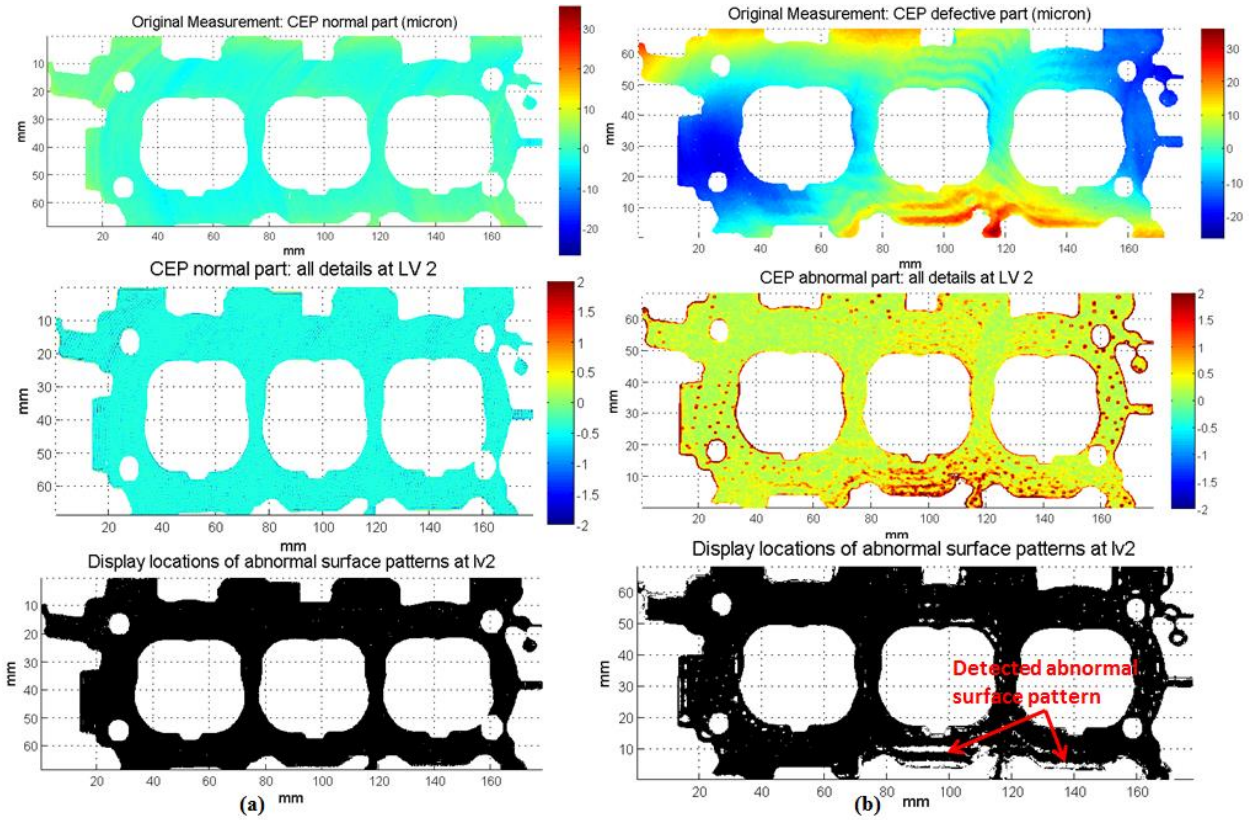

Figure 4.27 Detection results on Al workpieces with features: (a) defective, (b) normal

4.5 Conclusion

This research work presents a framework on the utilization of high definition data based on the digital holographic interferometry technique. The framework involves two steps. The first step focuses on the extraction of the generalized surface shape from measurements. The generalized surface shape can be utilized to monitor the process variations. The generalized surface shape can also be used as a reference for assembly process which surface distortion is an important factor to be considered. The second step focuses on the extraction of specific details. Metrics developed in the second step are application-oriented. For example, the applications of tool wear evaluation and abnormal surface pattern detection utilize surface details in different spatial ranges of surface wavelengths, algorithms can be developed to extract these specific

information for quality evaluation. These applications can also be operated simultaneously as they are independent. The outputs after applying the proposed framework can be implemented to monitor the process conditions and evaluate the quality of machined surfaces. Implementation of this technique in the characterization of the surface variation has several advantages compared to conventional GD&T: 1) one single measurement can provide multiple parameters that normally require multiple different measurements by using different conventional metrology systems; 2) meaningful tools can be used to further understand the mechanism of surface shape variation; 3) developed metrics can be directly related to process parameters that provide more accurate result for process monitoring; and 4) prevent sending parts with undesired surface shape to downstream, which would result distortion or leakage problem. There are still remaining challenges in this area and require further research efforts. For example, shape extraction strategy is desired to evaluate a machined surface that has highly asymmetric shape since current quadratic surface extraction is only good to process symmetric or near symmetric surfaces. Non-parametric methods can be used to extract the shape of highly asymmetric machined surface. However, no explicit expression can be obtained, which limits the adoption of this type of technique.

CHAPTER 5 CONCLUSIONS AND FUTURE WORK

5.1 Conclusions and contributions

A fringe projection system based on phase shifting interferometry was developed in Chapter 2. No optical lenses were used between the light source and the object plane. This system setup reduces the system complexity significantly and can obtain measurement at good accuracy and fast speed. The flexibility of the system enables it to conduct measurements over various types of surfaces. The cost of this system is low compared to other measurement systems that require a number of optical lenses and mirrors. Several real engineered surfaces that were difficult to be measured using conventional metrology systems were successfully measured. The accuracy of measured results was validated using a certified laser microscope (OLS4000) with at least one order of magnitude higher in accuracy in X, Y, and Z directions. The system performance was demonstrated and sources of error were analyzed.

An improved phase unwrapping algorithm was developed to assist the system in processing collected phase-shifted images in Chapter 3. A hybrid guidance map was the major contribution of this algorithm. Unlike conventional guidance maps that are generated based on the evaluation of the quality of wrapped phase maps, the hybrid guidance map also evaluates the quality of original acquired images. A combination of quality maps of the original obtained images and the calculated wrapped phase map can further reduce the impacts of noise and errors in phase unwrapping process. A detailed case study of measuring the flank surface of a pinion

gear was given. And the results were comparable with measurements obtained from contact probing system (Jenoptik).

A systematic surface analysis framework was proposed in Chapter 4 to embrace the availability of high definition measurements of machined surfaces. No matter which system is used to obtain high definition surface measurements, the proposed strategy can be applied to help researchers and engineers to uncover new findings from machined surfaces. The strategy emphasizes the characterization of generalized shape (form scale) and localized surface information (waviness scale) of a machined surface. Surface shapes at these two scales are related to various functionality requirements of a product. For example, generalized shape is critical to the quality of assembly, metrics extracted in waviness scale are closely related to potential leakage problems. Moreover, patterns observed on a machined surface also reflect the impacts of process parameters, features extracted from machined surface can be implemented for process condition monitoring. For example, the degradation of machine tool will always produce surface with undesired quality. Appropriate selection of the surface feature can be used to monitor the occurrence of undesired machining condition. Examples of automatic abnormal surface pattern detection were illustrated on aluminum parts, CGI parts, and aluminum parts with features.

5.2 Future work

This research may continue further in both of major topics covered in this dissertation. First, further improvements of the developed fringe projection system may be conducted to test the performance of current system at more details. Moreover, additional approaches such as multiple-wavelength or multiple-frequency technique can be considered to expand the system's capability in measuring surfaces with sharp discontinuities. Secondly, new metrics and applications will be explored under the proposed framework of surface shape characterization and feature extraction based on high definition measurements. Another area needs effort to be put in is how we can overcome the barriers of implementing developed applications in real plant.

For the developed fringe projection system, further research can be conducted on three areas:

(1) More detailed experiments to evaluate the performance of the current system

For the developed fringe projection system, more detailed system performance tests could be conducted. This is helpful to identify significant factors that contribute to the errors of measurements. Then compensations can be made to improve the accuracy and stability of the developed system. One issue frequently occurs in the adoption of optical system is the long setup time as there are always many parameters can affect the final performance of a measurement system. If a through performance analysis is conducted over the current system, an optimal strategy could be proposed to enable a quick setup when new workpiece is being measured.

(2) Tackle the problem of laser speckle effect occurred during measurement

When coherent diode laser is used as light source to measure rough surfaces (such as laser weld in this dissertation), speckle effect tends to occur. The presence of speckle on a target surface usually makes the camera unable to obtain sufficient information. Therefore, a reduction of speckle effect is highly desirable. Researchers have conducted extensive studies to find effective methods in reduction of speckle effect [Trisnadi, 2002; Yurlov et al., 2008; Tran et al., 2014]. Currently, we do not have an optimal method for speckle reduction. We often take approaches such as adjust projection angle and change the way a fixture holds an object to keep the speckle out of the area of interest of our measurement or reduce the area it affects as large as possible. Further study can be conducted to propose a better strategy to suppress speckle effect in our developed system.

(3) Expand current system's capability in measuring sharp discontinuous surfaces

Current system adopts a single wavelength laser source with constant phase-stepping to generate a series of phase-shifted fringe patterns on the surface of an object. This gives us a single wrapped phase map of the measured surface. This approach usually does not perform very well when the target object has a surface with isolated areas or big discontinuities in the height direction. Alternatives can be considered to improve the system's capability in measuring these kinds of surfaces include: 1) multiple-wavelength and 2) multiple-frequency measurement.

The brief idea behind these two techniques is to obtain more than one unwrapped phase maps with at least one of them without phase ambiguity. Assume two wrapped phase maps are

obtained and denoted as ϕ_1 and ϕ_2, with fringe wavelength of λ_1 and λ_2, respectively. Denote Φ_1 and Φ_2 as the retrieved continuous phase maps corresponding to ϕ_1 and ϕ_2. Eq. (5.1) can be used to describe the relationship between these two continuous phase maps:

$$\begin{aligned}&\lambda_1 \cdot \Phi_1(x,y) = \lambda_2 \cdot \Phi_2(x,y)\\ &\Phi_1(x,y) = \phi_1(x,y) + 2\pi k_1(x,y)\\ &\Phi_2(x,y) = \phi_2(x,y) + 2\pi k_2(x,y)\end{aligned} \quad \text{.....(5.1)}$$

As one of the wrapped phase map among these two does not need to be unwrapped (e.g., $\Phi_1 = \phi_1$), can be easily calculated based on the relationship shown in Eq.(5.1).

For multiple-wavelength methodology, two or more wavelengths are selected (we use a two-wavelength case as an example here). The equivalent phase ϕ_{eq} can be described as,

$$\phi_{eq}(x,y) = \phi_1(x,y) - \phi_2(x,y) \quad \text{.....(5.2)}$$

Denote λ_1 and λ_2 as the two selected wavelengths, then, the equivalent wavelength λ_{eq} is,

$$\lambda_{eq} = \frac{\lambda_1 \lambda_2}{|\lambda_1 - \lambda_2|} \quad \text{.....(5.3)}$$

Assume $\lambda_1 > \lambda_2$, and λ_1 and λ_2 are carefully selected and spaced closely, the equivalent can be large enough so that phase ambiguity can be avoided. Take the equivalent phase map and apply it in Eq.(5.1) can retrieve other wrapped maps.

For multiple-frequency methodology, sets of fringe patterns with different spacing are projected on the object surface. The coarsest fringe pattern typically only has one fringe across the target surface, in which it means there is no phase wraps. It is used as the reference in the unwrapping process of other wrapped phase maps. The process goes from the coarsest phase map to the finest one by using Eq.(5.1).

In order to adopt these two methodologies mentioned above, the current system configuration needs to be adjusted accordingly. A tunable laser source is needed to be able to generate lasers at close but different wavelengths to obtain a fairly large equivalent wavelength. On the other hand, the current holder of fiber optics can be redesigned to be able to change the distance between the two fibers automatically and accurately. As the spacing of projected fringe patterns is determined by the distance between two fibers (assume other affecting factors, such as laser wavelength, are unchanged), controlling the distances between fibers can achieve the goal of generating fringe patterns with different spacing.

One big advantage of adopting the aforementioned strategies is the wrapped phase map will be unwrapping in the time domain instead of the spatial domain. There is no need to compare neighbor pixels during the phase unwrapping process. Each pixel from the measured data will be unwrapped independently by applying properly selected temporal phase unwrapping algorithms. This can prevent propagation of incorrectly unwrapped pixels into other pixels. Thus, isolated surfaces or surfaces with sharp discontinuities can be measured more accurately. This

approach has the potential to expand the capability of the current developed fringe projection system.

However, there are additional things needs to be considered: 1) the stability of laser source plays a critical role in the multiple-wavelength approach as selected wavelengths are close to each other to enlarge the equivalent wavelength; 2) as a small error in the distance between two fibers can translate into a large error in the spacing of fringe patterns, the holder for fiber optics needs to be carefully designed to meet the high accuracy requirement; 3) multiple-wavelength approach increases the unambiguous measurement range by sacrificing its signal to noise ratio (SNR); 4) both methodologies require multiple sets of measurements of the target object, thus the measurement speed will usually be longer; and 5) temporal phase unwrapping algorithms are good at retrieving true phase information of sharp discontinuous surfaces, however, these algorithms also are usually computational expensive comparing to spatial phase unwrapping algorithms.

For multiple-frequency methodology, sets of fringe patterns with different spacing are projected on the object surface. The coarsest fringe pattern typically only has one fringe across the target surface, in which it means there is no phase wraps. It is used as the reference in the unwrapping process of other wrapped phase maps. The process goes from the coarsest phase map to the finest one by using Eq.(5.1).

For the proposed framework of utilizing high definition surface measurements, there are two areas can be studied in the future:

(1) Develop new metrics for surface shape characterization.

New surface metrics can be developed. As machined surfaces will always interact with their surroundings or mating components, new surface metrics have the potentials to become critical indicators in the evaluation of a workpiece's functionality. Moreover, new applications can be developed with the integration of process information and machine conditions. For example, many machining operations in plants involve multiple machines working in parallel. These machines are set to complete the same operation. In ideal condition, machined workpieces from these machines will be the same. However, variations always exist among workpieces come from different machines. Remaining tooling marks on machined surfaces are reflections of the processes that they have gone through. Variations among different machines would result in different tooling marks. Combining the HDM data and process information regarding operated machines can be helpful to detect machine variations and find out potential root causes.

(2) Overcome the barriers of implementing developed strategy in real plant.

A workpiece in real plant always goes through multiple different operations. A knowledge strategy needs to be built up to categorize and store all related machining process information. An optimal knowledge library should be able to recognize the major process that may result in the most obvious tooling marks on the surface of a workpiece. Thus, data analysis

can be quickly narrowed down to study the differences among surface patterns instead of doing trial and error of all possible processes.

In addition, no matter what new metric is proposed, attention should always be given to the processing speed. In the world of HDM data, data size is overwhelming, efficient algorithm can process large amount of data rapidly and trigger alarm for plant engineers once faulty condition is detected. Then, proper measures could be taken to correct it and avoid further production waste. Therefore, the speed of algorithm is a very critical issue needs to be addressed in order for any strategy to be implemented in real plant successfully.

REFERENCE

ASME B46.1, (2009), Surface Texture (Surface Roughness, Waviness, and Lay).

Aleksoff, C., (2006), *Multi-wavelength digital holographic metrology*, SPIE Proceedings-Optical Information Systems IV, 63111D.

Aguilar, J.J., et al., (1996), *Stereo vision for 3D measurement: accuracy analysis, calibration and industrial applications*, Measurement, Vol. 18, Issue 4, pp. 193-200.

Arines, J., (2003), *Least squares modal estimation of wrapped phases: application to phase unwrapping*. Applied Optics, 42(17): 3373-8.

Aris, N. F. M. and K. Cheng, (2008), *Characterization of the surface functionality on precision machined engineering surfaces*. Int J Adv Manuf Technol, 38: 402-409.

Asundi, A., et al. (1998), *Fast phase-unwrapping algorithm based on a gray scale mask and flood fill.* Applied Optics, 37, pp. 5416-5420.

Baek, D. K., et al., (1997), *A Dynamic Surface Roughness Model for Face Milling*. Precision Engineering, 20(3), pp. 171-178.

Barbosa, E.A., et al. (2007), *Multiwavelength electronic speckle pattern interferometry for surface shape measurement.* Applied Optics, Vol. 46, Issue 14, pp. 2624-2631.

Beraldin, J.A., et al., (2001), *Active 3D sensing*. NRC Publication Number, Technical Report 44159, Ottawa.

Besl, P. J. and R. C. Jain, (1985), *Three dimensional object recognition*, ACM computing surveys, vol, 17, no 75-145.

Besl, P. (1989), *Active optical range imaging sensors.* Advances in Machine Vision, chapter 1, pages 1–63. Springer-Verlag, 1989.

Blais, F. (2004), *A review of 20 years of range sensors development*. J. Electronic Imaging, 13, 231- 240.

Blunt, L., (2003), *Advanced Techniques for Assessment Surface Topography: Development of a Basis for 3D Surface Texture Standards*. Kogan Page Science, ISBN 1903996112.

Bone, D.J., et al., (1986), *Fringe-pattern analysis using a 2-D Fourier transform*. Applied Optics, Vol. 25, Issue 10, pp. 1653-1660.

Bone, D.J., (1991), *Fourier fringe analysis: The two-dimensional phase unwrapping problem*. Applied Optics, Vol. 30, pp.3627–3632.

Brophy, C. P., (1990), *Effect of Intensity Error Correlation on the Computed Phase of Phase-shifting Interferometry*, Journal of Optical Society of America A, 7 (4), pp. 537-541.

Bruning, J. H., et al., (1974), *Digital Wavefront Measuring Interferometer for Testing Optical Surfaces and Lenses*. Applied Optics, Vol. 13, Issue 11, pp. 2693-2703.

Bueno, J. M., (2010), *Wavefront measurements of phase plates combining a point-diffraction interferometer and a Hartmann-Shack sensor*. Applied Optics, Vol. 49, Issue 3, pp. 450-456.

Burke, J., (2010), *Suppression of fundamental-frequency phase errors in phase-shifting interferometry*. Optics Letters, Vol. 35, Issue 12, pp. 2079-2081.

Burke, J., (2012), *How to remove fundamental-frequency phase errors from phase-shifting results*. Proceedings of SPIE, Vol. 8493, Interferometry XVI: Techniques and Analysis, 84930I-1

Caber, P.J., (1993), *Interferometric profiler for rough surfaces*. Applied Optics, Vol. 32, Issue 19, pp. 3438-3441.

Camelio, J., et al., (2004), *Diagnosis of Multiple Fixture Faults in Machining Processes Using Designated Component Analysis*. Journal of Manufacturing Systems, 23(4), pp. 309-315.

Cardenas-Garcia, J.F., et al., (1991), *Projection moiré as a tool for the automated determination of surface topography*. Proceedings of SPIE 1554B, pp. 210–224.

Carré, P., (1966), Installation et Utilisation du Comparateur Photoélectrique et Interférentiel du Bureau International des Poids et Mesures. Metrologia, Vol. 2, No 1, pp. 13-23.

Chen, C.W., et al., (2000), *Network approaches to two dimensional phase unwrapping: intractability and two new algorithms.* Journal of Optical Society of America A. 17(3), pp.401–414.

Chen, F., et al., (2000), Overview of three-dimensional shape measurement using optical methods. Optical Engineering, 39, 10-22.

Chen, H., et al., (2005), *Application of visual servoing to an X-ray based welding inspection robot*. Proceedings ICCA, vol. 2, pp. 977–982.

Cheng, Y-Y. and J.C. Wyant, (1985), *Multiple-wavelength phase shifting interferometry*. Applied Optics. 24, pp.804-806.

Coleman, D.E., et al., (1980), *A System of Subroutines for Iteratively Reweighted Least Squares Computations*. ACM Transactions on Mathematical Software, 6, 327-336.

Creath, K., (1988), *Phase-shifting interferometry techniques*. Progress in Optics, E. Wolf, ed. Vol. 26, pp. 357-373.

Creath, K., (1988), *Phase–measurement interferometry techniques*. Progress in Optics, Vol. 26, pp. 350–393. Elsevier Science Publishers.

Creath, K., (1992), *Error sources in phase-measuring interferometry (Invited Paper)*. Proc. SPIE 1720, Intl Symp on Optical Fabrication, Testing, and Surface Evaluation, 428.

Creath, K., (1993), *Temporal phase measurement methods*: *Interferogram analysis, digital fringe pattern measurement techniques.* Bristol: Institute of Physics Publishing, pp. 94–140.

Deck, L. L., (2009), *Suppressing phase errors from vibration in phase-shifting interferometry*. Applied Optics, Vol. 48, Issue 20, pp. 3948-3960.

Ding, Z.H., et al., (2000), *Fiber-optic based scanning confocal microscopic interferometer for the measurement of surface topography in manufacturing process*. IEEE Industry Applications Conference, 2000, vol.2, pp.1029-1032.

Dirac, P.A.M., (1931), *Quantized singularities in the electromagnetic field*. Proceedings of the Royal Society A, 133, pp. 60–72.

Eshleman, A. E. and H. D. Meriwether, (1966), *Animated Display of Dynamic Characteristics of Complex Structures*. 1966 UAIDE Annual Meeting, San Diego.

Eshleman, A. E. and H. D. Meriwether, (1967), *Graphic Applications to Aerospace Structural Design Problems*. 1967 SHARE 4th Annual Design Automation Workshop, Los Angles.

Ewald, H., (2003), *3-Dimensional magnetic leakage field sensor in nondestructive testing*. Proceedings 20th IEEE I2MTC., vol. 2, pp. 1309–1311.

Fang, S.P., et al., (2011), *Design of laser interferometric system for measurement of gear tooth flank*. Optik, 122 (14), pp. 1301-1304.

Flynn, T.J., (1997), *Two-dimensional phase unwrapping with minimum weighted discontinuity*. Journal of Optical Society of America A. 14(10), pp.2692–2701.

Fu, S., et al, (2003), *Engineering surface analysis with different wavelet bases*, Journal of Manufacturing Science and Engineering. Vol. 125, page 844-852.

Fu, Y., (2010), *Low-frequency vibration measurement by temporal analysis of projected fringe patterns*. Optics and Laser Engineering. Vol. 48(2), pp. 226–234.

Geng, Z.J., (1996), *Rainbow three-dimensional camera: new concept of high-speed three-dimensional vision systems*. Optical Engineering, 0091-3286 35, (2), pp. 376–383.

Goch, G., (2003), *Gear Metrology*. CIRP Annals - Manufacturing Technology, Volume 52, Issue 2, pp. 659-695.

Goldstein, R.M., et al., (1988), *Satellite radar interferometry: two-dimensional phase unwrapping.* Radio Science, 23, pp.713–720.

Goodwin, E. P., et al., (2006), *Field guide to interferometric optical testing*. SPIE PRESS BOOK, ISBN: 9780819465108.

Gorthi, S. S. and P. Rastogi, (2010), *Fringe Projection Techniques: Whither we are?*. Optics and Lasers in Engineering, Vol. 48, No. 2, pp. 133-140.

Groot, P. J., (1995), *Vibration in phase-shifting interferometry*. Journal of Optical Society of America A / Vol. 12, No. 2/February, pp 354-365.

Grove, D.W., (2004), *Multifactor B-spline mixed models in designed experiments for the engine mapping problem*. Journal of Quality Technology, Vol. 36 (4), 380-391.

Greivenkamp, J.E., (1984), *Generalized Data Reduction for Heterodyne Interferometry*. Optical Engineering, Vol. 23, Issue 4, pp. 350-352.

Gu, F. et al., (1997), *A Model for the Prediction of Surface Flatness in Face Milling*. Journal of Manufacturing Science and Engineering, 119(4A), p. 9.

Gu, H.P. and W.W. Duley, (1996), *Resonant acoustic emission during laser welding of metals*. Journal of Physics D: Applied Physics, 29 550-555.

He, L., (2006), *Vibration-compensated interferometry system using phase-modulating interference fringe subdivision technology*. Applied Optics, Vol. 45, Issue 31, pp. 7987-7992.

Hibino, K., et al., (1995), *Phase shifting for nonsinusoidal waveforms with phase-shift errors*. Journal of the Optical Society of America A , Vol. 12, Issue 4, pp. 761-768.

Huang, P.S., et al., (2003), *High speed 3D Shape Measurement Based on Digital Fringe Projection*. Optical Engineering 42(1), pp. 163-168.

Hugel, H., et al., (1999), *Laser beam welding: resent developments on process conduction and quality assurance.* Proceedings of SPIE 3571, 52-60.

Hutber, D., (1987), *Automatic inspection of 3D objects using stereo.* SPIE Optics, Illumination and Image Sensing for Machine Vision II, 850 (1987), pp. 146–151.

Huntley, J.M., (1989), *Noise-immune phase unwrapping*. Applied Optics, 28(15), pp.3268–3270.

Huntley, J.M., et al., (1993), *Temporal phase-unwrapping algorithm for automated interferogram analysis*. Applied Optics, Vol. 32, Issue 17, pp. 3047-3052.

Huntley, J.M., (1997), *Shape measurement by temporal phase unwrapping: comparison of unwrapping algorithms*, Measurement Science and Technology, Volume 8, Number 9.

Indebetouw, G. and R. Czarnek, (1992), *Selected Papers on Optical Moire and Applications.* SPIE Milestone Series. SPIE Optical Engineering Press, Bellingham, Washington.

Ji, Z. and M.C. Leu, (1989), *Design of Optical Triangulation Devices*. Optics and Laser Technology, Vol. 21(5), pp. 335-338.

Jin, R., et al., (2012), *Sequential Measurement Strategy for Wafer Geometric Profile Estimation*. IIE Transactions, Vol. 44 (1), 1-12.

Jenkinson, M., (2003), *Fast, automated, N-dimensional phase unwrapping algorithm*. Magnetic Resonance in Medicine. Vol 49, pp.193–197.

Jiang, X.Q., et al., (2010), *Fast surface measurement using wavelength scanning interferometry with compensation of environmental noise*. Applied Optics, Vol. 49, Issue 15, pp. 2903-2909.

Joenathan, C., et al., (1990), *Contouring by electronic speckle pattern interferometry using dual beam illumination*. Applied Optics. 29, pp.1905–1911.

Kanade, T. and M. Okutomi, (1994), *A stereo matching algorithm with an adaptive window: theory and experiment*. IEEE Transactions on Pattern Analysis and Machine Intelligence, Vol.16, No.9, pp.920-932.
Keferstein, C.P. and M. Marxer, (1998), *Testing Bench for Laser Triangulation Sensors*. Sensor Review, 18(3), pp.183-187.

Kerr, D., et al., (1996), *Unwrapping of interferometric phase-fringe maps by the discrete cosine transform*. Applied Optics, 35(5): 810-6.

Khalifa, O. O. and A. Densibali, (2006), *Image Processing for chatter identification in machining processes*. International Journal of Advanced Manufacturing Technology, 31: 443 – 449.

Kim, S.J., et al., (2007), *Prediction of chatter in NC machining based on a dynamic cutting force model for ball end milling*. International Journal of Machine Tools and Manufacture 47, 1827-1838.

Kline, W.A. and R.E. DeVor, (1983), *The Effect of Runout on Cutting Geometry and Forces in End Milling*. International Journal of Machine Tool Design and Research, 23(1-2), pp. 123-140.

Koliopoulos, C. L., (1991), *Simultaneous phase shift interferometer*. Proceedings of SPIE 1531, 119-127.

Kong, I. and S. Kim, (1994), *General algorithm of phase-shifting interferometry by iterative least squares fitting.* Optical Engineering, Vol. 1; 34(1), pp.183-188.

Kuljanic, E., et al., (2008), *Multisensor approaches for chatter detection in metal cutting*. Journal of Sound and Vibration 312, 672–693.

Kwon, T. and S.W. Kim, (2011), *Fiber-optic interferometer for surface profile measurement with vibration suppression*. Optics Express, Vol. 19, Issue 5, pp. 4223-4230.

Langoju, R., et al., (2006), *Phase-shifting interferometry in the presence of nonlinear phase steps, harmonics, and noise*. Optics Letters, Vol. 31, Issue 8, pp. 1058-1060.

Li, Y. and P. Gu, (2004), *Free-form surface inspection techniques state of the art review*. Computer-Aided Design, 36, pp. 1395-1417.

Li, Y., (2009), *Development of as-manufactured CAD model to support the concept of "Product DNA".* https://deepblue.lib.umich.edu/handle/2027.42/63759

Li, Y., et al., (2010), *Measurement and Defect Detection of the Weld Bead Based on Online Vision Inspection*. IEEE Trans on Instrumentation and Measurement, Vol. 59, No.7.

Liang, Z.P., (1996), *A model-based method for phase unwrapping*. IEEE Trans Medical Imaging, 15, pp.893–897.

Liao, Y., (2010), *Extraction of 3D machined surface features and applications.* https://deepblue.lib.umich.edu/handle/2027.42/78782

Liao, Y., et al., (2009), *Assessment of Tool Wear Based on Surface Texture Parameters.* ASME 2009 International Manufacturing Science and Engineering Conference, 2, pp. 463-470.

Liao, Y. G. and S.J. Hu, (2001), *An Integrated Model of a Fixture-Workpiece System for Surface Quality Prediction.* International Journal of Advanced Manufacturing Technology, 17(11), pp. 810-818.

Liu, W., et al., (2000), *Color-coded projection grating method for shape measurement with a single exposure*, Applied Optics, 0003-6935 39, (20),pp. 3504–3508.

Livnat, A, and O. Kafri, (1983), *Finite fringe shadow moiré slope mapping of diffusive objects*. Applied Optics, Vol. 22, Issue 20, pp. 3232-3235.

Lu, G.W., et al., (1998), *Application of phase-shift optical triangulation to precision gear gauging*. Proceedings of SPIE 3520, pp. 52-63.

Maack, T., et al., (1995), *Three coordinate measurement of an object surface with a combined two-wavelength and two source phase shifting speckle interferometer*. Optics Communications, 115, pp. 576–584.

Malacara, D., et al., (2005), *Interferogram Analysis for Optical Testing*. 2nd edition, CRC Press, Boca Raton.

Matsumoto, T., et al., (1991), *Laser moiré topography for 3D contour measurement*. Proceedings of SPIE, 1332, pp. 530–536.

Medioni, G. and R. Nevatia, (1985) *Segment-based stereo matching, Computer Vision*. Graphics, and Image Processing, Vol. 31, Issue 1, pp. 2-18.

Melozzi, M., et al., (1995), *Vibration-insensitive interferometer for on-line measurement*s. Applied Optics, Vol. 34, Issue 25, pp. 5595-5601.

Moore, D.T. and B.E. Truax, (1979), *Phase-locked Moiré fringe analysis for automated contouring of diffuse surfaces*. Applied Optics. 18, pp. 91-96.

Morgan, C.J., (1982), *Least squares estimation in phase-measurement interferometry*. Optics Letters, Vol. 7, Issue 8, pp. 368-370.

Moring, I. and H. Ailisto, (1989), *Active 3-D vision system for automatic model-based shape inspection*. Optics and Lasers Engineering, 10, 3–4.

Nguyen, H., (2013), *Surface variation characterization and control using high-definition metrology*. https://deepblue.lib.umich.edu/handle/2027.42/97849

Nomura, T., et al., (1998), *Shape measurements of mirror surfaces with a lateral-shearing interferometer during machine running*, Precision Engineering. Volume 22, Issue 4, 185-189.

Novák, J., et al., (2008), *Multi-step phase-shifting algorithms insensitive to linear phase shift errors*. Optics Communications, Volume 281, Issue 21, 1 November 2008, pp. 5302-5309.

Onuma, K., et al., (1993), *Application of real time phase shift interferometer to the measurement of concentration field.* Journal of Crystal Growth, 129 (3-4), pp. 706-718.

Park, H. and S. Rhee, (1999), *Estimation of weld bead size in CO2 laser welding by using multiple regression and neural network.* Journal of Laser Applications, 11, 143-150.

Pan, J., et al., (2006), *Color phase-shifting technique for three-dimensional shape measurement.* Optical Engineering, Vol.45 (1):013602-013602-9.

Passini, A., (2011), *Ultrasonic inspection of AA6013 laser welded joints*. Materials Research, v 14, n 3, p 417-422.

Peters, J., et al., (2000), *Helical Gear Measurement Using Structured Light*. Proceedings of the XVI IMEKO World Congress, Wien, pp. 227–230.

Pommer, A., (2002), *Gear Rollscan for High Speed Gear Measurement - A Revolutionary New Method for a Complete Topographical Inspection of Gears*. International Conference on Gears Vol. 2, VDI-Berichte 1665, p. 785-796.

Prati, C., et al., (1990), *SAR interferometry: A 2- D phase unwrapping technique based on phase and absolute values information*. Proceedings of IGARSS, pp. 2043–2046.

Pritt, M.D., et al., (1994), *Least squares two-dimensional phase unwrapping using FFT's*. IEEE Transactions on Geoscience and Remote Sensing, , Vol.32, No.3, pp.706-708.

Pritt, M.D., (1997), *Congruence in least squares phase unwrapping*. 1997 IEEE International Geoscience and Remote Sensing, Vol.2, No38, pp.875-877.

Puchala, S.S., (2013), *High definition metrology based process control: measurement system analysis and process monitoring*. https://deepblue.lib.umich.edu/handle/2027.42/99874

Raja, J., (2002), *Recent advances in separation of roughness, waviness and form*. Precision Engineering, Volume 26, Number 2, pp. 222-235(14).

Rajshekhar, G. and P. Rastogi, (2012), *Fringe analysis: Premise and perspectives*, Optics and Lasers in Engineering, Volume 50, Issue 8, pp. iii-x.

Reid, G. T., (1986), *Automatic fringe pattern analysis: A review*. Optics and Lasers in Engineering, 7, pp.37–68.

Roddier, C. and F. Roddier, (1987), *Interferogram analysis using Fourier transform techniques*. Applied Optics, Vol. 26, Issue 9, pp. 1668-1673.

Saldner, H. O. and J. M. Huntley, (1997), *Profilometry using temporal phase unwrapping and a spatial light modulator-based fringe projector*. Optical Engineering, 36 (2), pp.610–615.

Salvi. J., et al.,(2004), *Pattern codification strategies in structured light systems*. Pattern Recognition , Vol. 37, Issue 4, pp. 827-849.

Salvi, J., et al., (2010), *A state of the art in structured light patterns for surface profilometry*. Pattern Recognition, Vol. 43, Issue 8, pp. 2666-2680.

Sansoni, G., et al., (2009), *State-of-The-Art and Applications of 3D Imaging Sensors in Industry, Cultural Heritage, Medicine, and Criminal Investigation*. Sensors, 9, pp. 568-601.

Schmit, J. and K. Creath, (1995), *Extended averaging technique for derivation of error-compensating algorithms in phase-shifting interferometry*. Applied Optics, Vol. 34, Issue 19, pp. 3610-3619

Schmit, J. and A. Olszak, (2002), *High-Precision Shape Measurement by White-Light Interferometry with Real-Time Scanner Error Correctio.* Applied Optics, Vol. 41, Issue 28, pp. 5943-5950.

Schwartz, J. T. and M. Sharir, (1987), *Identification of partially obscured objects in two and three dimensions by matching noisy characteristic curves*. Int. J. Robotics Res., Vol. 6, no 2, pp 29-44.
Schmitz, T. L., et al., (2006), *Runout Effects in Milling: Surface Finish, Surface Location Error, and Stability*. International Journal of Machine Tools & Manufacture, 47(5), pp. 841-851.

Schreiber, H., et al., (2007), *Phase shifting interferometry*. Optical Shop Testing, 3rd ed., D. Malacara, ed. (Wiley), pp. 547–666.

Servin, M., et al., (1997), *Demodulation of a single interferogram by use of a two–dimensional regularized phase–tracking technique*. Applied Optics, 36(19), pp.4540–4548.

Sharma, J. N., (2004), *Numerical methods for engineers and scientists*. Alpha Science Intl Ltd, ISBN-13: 978-1842651629.

Sikström, F., et al., (2006), *3D-scanning for weld distortion measuring*. Proceedings, IEEE Int. IMTC., Apr. 24–27 , pp. 2132–2137.

Smythe, R. and R. Moore, (1984), *Instantaneous phase measuring interferometry*. Optical Engineering, 23, pp. 361–365.

Srinivasan, V., et al., (1984), *Automated phase–measuring profiometry of 3–D diffuse objects*. Applied Optics, 23 (18), pp.3105–3108.

Strand, J., et al., (1999), *Two-dimensional phase unwrapping using a block least squares method*. IEEE Transactions on Image Processing, Vol.8, No.3, pp.375-386.

Srinivasan, V., et al., (1985), *Automated phase–measuring profilometry: a phase mapping approach.* Applied Optics, 24(2), pp.185–188.

Stout, K. J., (1994), *Development of Methods for Characterization of Roughness in Three Dimensions*. Commission of the European Communities, ISBN 0704413132

Su, X.Y. and Chen, W.J. (2004), *Reliability-guided phase unwrapping algorithm: a review*, Optics and Lasers in Engineering, Volume 42, Issue 3, Pages 245–261.

Sun, J., et al., (2003), *Stereo matching using belief propagation*. IEEE Transactions on Pattern Analysis and Machine Intelligence, Vol.25, No.7, pp.787-800.

Sun, J., et al., (2006), *Large 3D free surface measurement using a mobile coded light-based stereo vision system*. Sensors and Actuators A: Physical, Vol. 132, Issue 2, pp. 460-471.

Sutherland, J. W. and R.E. DeVor, (1986), *Improved Method for Cutting Force and Surface Error Prediction in Flexible End Milling Systems.* ASME Journal of Engineering for Industry, 108(4), pp. 269-279.

Tajima, J., (1987), *Rainbow range finder principle for ranger data acquisition*. Proceedings of IEEE Workshop on Industrial Applications of Machine Vision and Machine Intelligence, pp. 381–386.

Takeda, M., et al., (1982), *Fourier–transform method of fringe–pattern analysis for computer–based topography and interferometry*. Journal of the Optical Society of America, 72(1), pp.156–160.

Takeda, M., et al., (1994), *Fourier-transform speckle profilometry: three-dimensional shape measurements of diffuse objects with large height steps and/or spatially isolated surfaces*. Applied Optics, 33, pp. 7829-7837.

Takeuchi, Y. and M. Sakamoto, (1964), *Analysis of Machining Error in Face Milling*. Proceedings of the International Machine Tool Design and Research Conference.

Taubin, G., (1988), *Algebraic nonplanar curve and surface estimation in three space with applications to position estimation*. Tech. Rep, LEMS-43, Div. Eng. Brown Univ. Providence, RI.

Taylor, F.W., 1906, *On the art of cutting metals*. Transactions of the ASME, 28: 31-350.

Taylor, B.N., et al., (1994), *Guidelines for evaluating and expressing the uncertainty of NIST measurement results*. NIST Technical Note 1297, U.S. Government Printing Office, Washington, DC.

Tran, T.K.T, et al., (2014), *Speckle reduction in laser projection using a dynamic deformable mirror*, Optics Express Vol. 22, Issue 9, pp. 11152-11166.

Trisnadi, J. I. (2002), *Speckle contrast reduction in laser projection displays*, Proc. SPIE 4657, Projection Displays VIII, 131 (April 30, 2002).

Trolinger, J.D., (1996), *Ultrahigh resolution interferometry*. Proceedings of SPIE, Laser Interferometry VIII: Application, 114.

Tsuruta, T. and Y. Itoh, (1969), *Interferometric generation of counter lines on opaque objects*. Optics Communications, 1(1), pp.34–36.

Vuylsteke, P. and A. Oosterlinck, (1990), *Range Image Acquisition with a Single Binary-Encoded Light Pattern.* IEEE Transactions on Pattern Analysis and Machine Intelligence. 12(2), pp. 148-164.

Wang, L.S. and S. Krishnaswamy, (1996), *Shape measurement using additive-subtractive phase shifting speckle interferometry*. Measurement Science and Technology. 7, pp. 1748–1754.

Wang, L. and M. Liang, (2009), *Chatter detection based on probability distribution of wavelet modulus maxima.* Robotics and Computer-Integrated Manufacturing 25, 989–998.

Wang, Y.J. et al., (2010), *Modified Fourier transform method for 3D profile measurement without phase unwrapping,* Optics Letters Vol. 35, Issue 5, pp. 790-792.

Weng, X. et al., (2014), *Multi-Scale Surface Characterization and Control Based High Density Measurements,* ASME 2014 International Manufacturing Science and Engineering Conference, Detroit, Michigan, USA, June 9–13, 2014, Vol 1.

White, R.A., et al., (1994), *Vision-based gauge for online weld profile metrology*. Proceedings of IEE -Science Measurement Technology, vol. 141, no. 6, pp. 521–526.

Whitehouse, D. J., (1994), *Handbook of Surface Metrology*. 1994 by Taylor & Francis, ISBN 9780750300391.

Whitehouse, D. J., (2004), *Surfaces and their Measurement*, Butterworth-Heinemann, ISBN 9781903996607.

Wilkinson, P., et al., (1997), *Surface Finish Parameters as Diagnostics of Tool Wear in Face Milling*. Wear, 205(1-2), pp. 47-54.

Windecker, R. and H.J. Tiziani, (1995), *Topometry of technicaland biologicalob jects by fringe projection.* Applied Optics, 34(19), pp. 3644–3650.

Wingerden, T. V., et al., (1991), *Linear approximation for measurement errors in phase shifting interferometry.* Applied Optics, 30 (1991) 2718- 2729.

Wizinowich, P. L., (1990), *Phase shifting interferometry in the presence of vibration: a new algorithm and system.* Applied Optics, Vol.29 (22), pp. 3271–3279.

Wyant, J. C., (1975), *Use of an AC Heterodyne Lateral Shear Interferometer With Real-Time Wavefront Correction System.* Applied Optics, Vol. 14, Issue 11, pp. 2622-2626.

Wyant, J. C., (2013), *Computerized interferometric surface measurements*. Applied Optics, Vol. 52, Issue 1, pp. 1-8.

W. F. GmbH., (1985), The new CNC Coordinate Measuring Machine, Schwarzenbek-Germany.

Xia, H., et al., (2008), *Gaussian Process Method for Form Error Assessment*. IIE Transactions, Vol. 40, 931-946.

Xie, X., et al., (1998), *Phase-unwrapping algorithm in the presence of discontinuities using a system with crossed grating.* Optics and Lasers Engineering, Vol. 29, Issue 1, pp.49–59.

Xu, D., et al., (2004), *Seam tracking and visual control for robotic arc welding based on structured light stereovision.* International Journal of Automation and Computing 170-82.

Yamaguchi, I., et al., (2001), *Surface shape measurement by phase shifting digital holography*. Optical Review, 8, 85–89.

Yang, T-H. and J. Jackman, (2000), *Form Error Estimation Using Spatial Statistics*. ASME Journal of Manufacturing Science and Engineering, Vol. 122 (1), 262-273.

Yao, Z., et al., (2010), *On-line chatter detection and identification based on wavelet and support vector machine*. Journal of Materials Processing Technology 210, 713–719.

Younes, M.A., et al., (2005), *Automatic measurement of spur gear dimensions using laser light, part 2: measurement of flank profile*. Optical Engineering 44(10), 103603.

Yurlov, V. et al., (2008), *Speckle suppression in scanning laser display*, Applied Optics Vol. 47, Issue 2, pp. 179-187

Zebker, H.A., et al., (1998), *Phase unwrapping algorithms for radar interferometry: residue-cut, least squares, and synthesis algorithms*. Journal of Optical Society of America A, Vol. 15, No. 3, pp.586-598.

Zhang, M., (2007), *Measurement scheme and classification methods for the development of a "product DNA" concept in manufacturing*.
https://deepblue.lib.umich.edu/handle/2027.42/126604

Zhang, S. et al., (2007), *Multilevel quality-guided phase unwrapping algorithm for real-time three-dimensional shape reconstruction*, Applied Optics, Vol. 46, No. 1, Pages 50-57.

Zhang, S., (2009), *Phase unwrapping error reduction framework for a multiple-wavelength phase-shifting algorithm*, Opt. Eng. 48(10), 105601.

Zhang, Y., et al., (2010), *Analysis of measuring errors for the visible light phase-shifting point diffraction interferometer*. Advances in Optoelectronics and Micro/Nano-Optics, pp.1-4.

Zhang, Z.H., (2012), *Review of single-shot 3D shape measurement by phase calculation-based fringe projection techniques.* Optics and Lasers in Engineering, Vol. 50, pp. 1097–1106.

Zhao, M. et al., (2010), *Quality-guided phase unwrapping technique: comparison of quality maps and guiding strategies*, Applied Optics Vol. 50, Issue 33, pp. 6214-6224.

Zhu, X.Y., et al., (2004), *Form Error Evaluation: An Iterative Reweighted Least Squares Algorithm*. ASME Journal of Manufacturing Science and Engineering, Vol.126 (3), 535-542.

Zuo, C. et al., (2016), *Temporal phase unwrapping algorithms for fringe projection profilometry: A comparative review*, Optics and Lasers in Engineering, Volume 85, Pages 84–103.